Short echo time MR Imaging of the lungs : methods and applications for experimental models of lung diseases in rodents

Magdalena Zurek

Numéro d'ordre : 186 Année 2010

THESE DE L'UNIVERSITE DE LYON

Délivrée par

L'UNIVERSITE CLAUDE BERNARD LYON 1

Ecole Doctorale de Physique et Astrophysique de Lyon

Spécialité : Physique
Option : Imagerie médicale

DIPLOME DE DOCTORAT
(arrêté du 7 août 2006)

par **Mlle ZUREK Magdalena**

IRM des poumons à temps d'écho courts : méthodes et applications à des modèles expérimentaux chez le rongeur

soutenue publiquement le **19 Octobre 2010**

Composition du Jury :

Dr. CREMILLIEUX Yannick - **Directeur de thèse**

Dr. BARBIER Emmanuel - **Rapporteur**

Pr. LAURENT François - **Rapporteur**

Pr. BERTHEZENE Yves - **Examinateur**

Pr. RUIZ-CABELLO Jesus - **Examinateur**

Dr. STILLER Detlef - **Examinateur**

RESUME en français

Dans ce travail de recherche doctorale, l'IRM des poumons à temps d'écho courts dite UTE (Ultra-short Echo Time) a été utilisée pour détecter le signal RMN du tissu pulmonaire afin de caractériser et étudier des modèles expérimentaux de maladies pulmonaires chez les rongeurs (rats et souris). En particulier, la technique radiale UTE a été appliquée pour détecter des biomarqueurs dans des modèles de broncho-pneumopathie chronique obstructive (BPCO) induite expérimentalement chez les rongeurs. La détection du signal RMN en provenance du parenchyme pulmonaire a fourni de précieux indicateurs de la maladie associés à l'élargissement des alvéoles pulmonaires et aux processus inflammatoires. De plus, la simplicité de mise en œuvre de cette technique (absence de synchronisation cardiaque et pulmonaire) permet de réduire les temps d'acquisition et apparait bien adaptée aux études longitudinales. La mesure répétée du centre de l'espace-k à chaque temps de répétition de la séquence a été utilisée pour développer une méthode de post-synchronisation reposant sur la détection des mouvements cardio-respiratoires, et permettant de produire des images sans artefacts de mouvement.

TITRE en anglais

Short echo time MR Imaging of the lungs: methods and applications for experimental models of lung diseases in rodents

RESUME en anglais

In this work, ultra-short echo time (UTE) MR imaging of the lungs is presented as a way of detecting pulmonary MRI signal, thus providing an opportunity to develop new imaging tools for the investigation of experimental models of lung diseases in rodents. The UTE imaging technique (TE=450 μs) was implemented on a 4.7 T scanner and applied to detect indicators of Chronic Obstructive Pulmonary Disease (COPD) induced experimentally in rodents. The improved signal detection from the lung parenchyma provided valuable markers of disease associated with airspace enlargement and inflammation. When used to investigate of inflammation specificity, this technique had advantages when delineating regions of early cellular infiltration into the site of inflammation. In the case of edematous signal quantification, the UTE technique was explored to improve the reliability of the volumetric measurements. This technique was demonstrated to be of use when easy protocol implementation (relatively high throughput and low-cost experiments) and longitudinal studies (limited interference with physiopathology) are of concern. The repetitive probing of the k-space center with a temporal resolution of the sequence's repetition time achieved with this technique was used to develop a self-gating method which relies on the tracking of cardio-respiratory motions, yielding images free from motion artifacts.

DISCIPLINE

Physique

MOTS-CLES

poumons, IRM, imagerie radiale, modèles animaux, BPCO, inflammation, emphysème, élastase, USPIO, LPS, lungs, MRI, radial imaging, rodents, COPD, inflammation, emphysema, self-gating

INTITULE ET ADRESSE DE L'U.F.R. OU DU LABORATOIRE :

Université Lyon1, CREATIS-LRMN, 3 rue Victor Grignard, 69616 Villeurbanne Cedex France.

To my parents

Acknowledgements

This study was carried out in the CREATIS-LRMN lab, located at the University of Lyon (Lyon, France) during the years 2007-2010. I wish to express my deepest gratitude to everyone who contributed to my study and supported my work towards this thesis. Particularly, I wish to mention the following persons:

First of all I would like to express my thanks to the supervisor of this study, Dr. Yannick Crémillieux Ph.D., for his support and inspiration during the PhD project. His dynamic guidance paved the way for numerous collaborations throughout the project, making my work particularly interesting.

I wish to express my sincere thanks to Dr. Katarzyna Cieslar Ph.D., especially for her support and guidance throughout the thesis project. I am very grateful for her patience and tireless answering of all my "questions from logic" and "questions from basics", no matter how simple they were. The support I received from Kasia is priceless.

I owe many thanks to Tangi Roussel M.Sc, for his support and for all the lengthy discussions I learned so much from. I am grateful for our working together, sharing all our small discoveries and our mutual support throughout the thesis.

I would also like to thank my office-roommates and dear friends: Amine Ph.D., Elise Ph.D., Florent, M.Sc., Nirilanto, M. Sc., Emmeline, M.Sc., Anoop, M.Sc., J-C, Ph.D., Benjamin, M.Sc., Andrii, M.Sc., Federico, M.Sc., Aziz, M.Sc., and Maurice for creating an unforgettable atmosphere in the lab. The support I received from all of them was invaluable.

I owe many thanks to my collaborators from the group in Boehringer Pharma, Germany: Dr. Detlef Stiller Ph.D., Dr. Thomas Kaulisch, Ph.D, and Laura

Carrero-Gonzalez M.Sc.; from the INSERM U955 group in Paris, France: Dr Laurent Boyer Ph.D., M.D., Philippe Caramelle, Dr. Jorge Boczkowski Ph.D.; from CRIS, Lyon, France: Dr. Ciril Martin Ph.D., Emeline Aufradet M.Sc.; from CHU Dijon, France Dr. Romaric Loffroy Ph.D., M.D.; from Trinity College, Dublin, Ireland: Dr. Oliviero Gobbo Ph.D., for invaluable co-operation and for the pleasure of working together.

I owe many thanks to Fabienne Larregain and Frederique Foulon who helped me with all the administrative formalities.

I want to thank Dr. Emmanuel Barbier and Pr. François Laurent, the official reviewers, as well as Pr. Jusus Ruiz-Cabello, Dr. Detlef Stiller, and Pr. Yves Berthezene for critical and thorough reading of the manuscript.

I would like to express my thanks to all my [SIKLIK] flatmates: Noémie, Xavier, Andreas, Thierry, Elodie, David and Jun, Claudia Z, Claudia A and Alice, Franziska, Yohan, Réjane, Sam, Matt, Caroline, Clément and Suresh with whom I shared both the high and low points throughout my PhD project and whose encouragement was tireless. I want to thank Noémie, Xavier and Andreas for their invaluable patience and support when I was starting to speak in French. Thanks for creating such a warm atmosphere and for making me always feel at home.

I owe my gratitude to Sam for his thorough revision of the language of this thesis.

Mauro Testa Ph.D and Pr. Andrzej Warczak from the Jagillonian University in Cracow, Poland deserve my gratitude for their support and an enormous influence on the decision about living and studing abroad.

Finally, I wish to thank Suresh for his critiques and careful reading of the manuscript. His support and encouragement have been important factors in helping me to complete this thesis.

I am greatly indebted to my parents, Halina and Ryszard Zurek, for their continuous support during my PhD.

The financial support from the European Network PHELINET (MRTN-CT-2006-36002) is gratefully acknowledged.

Contents

List of Figures

LIST OF FIGURES

LIST OF FIGURES

List of Tables

1

Introduction

1.1 Motivation

Chronic Respiratory Diseases (CRD), which include asthma and Chronic Obstructive Pulmonary Disease (COPD), affect up to one billion people worldwide. According to a report released by the World Health Organization (WHO) in 2001, five respiratory diseases (pulmonary infections, COPD, asthma, tuberculosis and lung cancer) account for 17.4% of all deaths. COPD is the only leading cause of death that still has a rising mortality rate and it has been estimated that by the year 2020, COPD will be the third leading cause of death in the world (50).

Medical imaging plays an ever increasing role in modern medicine, as it allows us to obtain a non-invasive view of internal organs, such as the lungs. These in-vivo images help detect diseases, track disease evolution, prepare and guide surgery, as well as play a role in drug testing and other research purposes.

High resolution computed tomography (HRCT) and nuclear medicine techniques such as gamma-scintigraphy, single photon-emission computer tomography (SPECT), positron-emission tomography (PET) and the traditional chest x-ray are imaging techniques which comprise the standard approaches for lung disease diagnostics (122). However, the exposure to ionizing radiation inherent in these techniques limits their extensive or repeated use for accurate follow-up studies - in order to track the evolution of a disease and its response to treatment or surgery (also known as a longitudinal study). Limiting cumulative radiation is particularly important in children requiring longitudinal studies as prolonged exposure to x-ray radiation is associated with an increased

risk of developing cancer.

Magnetic resonance imaging (MRI) has been recognized as a powerful and versatile tool for the non-invasive characterization of internal organs. This technique is based on physical principles of Nuclear Magnetic Resonance (NMR) and reflects the proton distribution (hydrogen nuclei) in the water or fat in tissues under study. This modality uses the magnetic properties of hydrogen nuclei in the presence of two magnetic fields - a static magnetic field (B_0) and a radio-frequency (RF) field - to produce images of those tissues. The main advantages offered by MR imaging are the lack of harmful ionizing radiation and improved contrast between the different soft tissues of the body, as compared to CT. Additionally, this modality allows one to obtain higher spatial resolution than in nuclear medicine imaging techniques.

To combat any given disease, a treatment must be created which will reduce, neutralize or reverse the effects of that disease. In order to establish the efficacy of the treatment, it is necessary to understand how therapeutic agents impact upon the body by validating their composition and by proving their appropriate and safe dosage. Usually, the validation procedure is performed in pre-clinical trials, as they allow one to avoid large numbers of human subjects being exposed to experimental drugs with no therapeutic potential.

Pre-clinical studies are used in the discovery of new drugs by providing evidence of a drug's efficacy and its potential toxicity. In the process of drug creation, genetically modified small rodents are often used to model specific aspects of human diseases. In pre-clinical, respiratory research studies, invasive and terminal approaches such as: broncho-alveolar lavage fluid analysis, histology and lung weighing, are the currently used methods of choice to validate new drugs (91).

The link between pre-clinical and clinical studies requires non-invasive techniques (like medical imaging) which can translate from animal models to human subjects, by minimizing changes in experimental protocol while the model organism is changed (101).

There are several reasons why MR imaging, amongst available imaging techniques, has the potential of ideal translational modality. First, it provides a high spatial resolution (pixel dimension in the order of 100μm in rodents) exceeding those obtained using nuclear medicine techniques (3-5 mm) by an order of magnitude. Therefore, MRI provides the morphological information which cannot be obtained through the use of the nuclear medicine techniques. Second, it allows longitudinal studies with minimal

interference to the health of animals - something which cannot be avoided with ionizing radiation-dependent techniques. Despite the advantages offered by MRI, the use of this imaging modality for clinical diagnostic and pre-clinical studies of respiratory diseases is still limited

The low proton density of the lungs, combined with susceptibility gradients induced by the air-tissue interfaces and motions within the thoracic cavity, produce an inherently weak MR signal from the lung parenchyma - making the lung the most challenging organ to be imaged by MRI.

This lack of MR signal can be overcome with the use of inhaled contrast agents. For example, large MR signals can be obtained by hyperpolarized (HP) gases, such as 3He or 129Xe. When inhaled, they allow imaging of their distribution in the pulmonary tree and alveolar spaces. Unfortunately, the escalating cost and scarcity of 3He have prohibited its widespread use for medical applications.

Conversely, the lack of signal from the lung parenchyma is also an advantage when imaging lung pathologies. For example, the gradient-echo sequence (with a conventional echo time in the order of 2 ms) was recently shown to be a powerful tool for lung investigation in various models of pulmonary diseases (11). Knowing that a significant contrast between a dark-appearing lung parenchyma and hyper-intense fluids is associated with diverse lung diseases, gradient-echo imaging has been successfully applied to numerous animal models for the detection and quantification of fluid secretion in asthma (119), Chronic Obstructive Pulmonary Diseases (COPD) (14), emphysema (99), lung fibrosis (58) and pneumonia (78).

Extending MRI applications to detect different aspects of lung disorders, apart from inflammatory fluids, is desired. This requires creation of new markers which will serve as potential indicators of physiological processes, pathologic processes and responses to therapeutic interventions.

Another challenge in lung research is posed by cardio-respiratory movements. To address this issue, one can acquire high resolution images using scan-synchronous ventilation, cardiac gating or combined approaches (18), (47). Although synchronizing image acquisition to the breathing cycle and gating to the cardiac cycle allows one to obtain high spatial resolution images of rodents' lungs, it increases the complexity of the MR protocol. Moreover, the scan-synchronous ventilation technique is invasive thus, it can cause injury of the lungs, especially if applied frequently (59).

For drug testing in pre-clinical studies, it is important to keep the acquisition condition as simple as possible so that repetitive, longitudinal measurements can be performed without interfering with the subject's physiology. Also, simple imaging protocols are required to preserve imaging efficiency, a key parameter in pharmacological disease investigation, where a large throughput is desired.

1.2 Aims of this thesis

The primary objective of this work is to develop new MR imaging protocols oriented toward drug and therapy evaluation in animal models of lung diseases. These protocols must have two general characteristics: keep the experiments simple to maximize protocol efficiency and be non-invasive to be suitable for longitudinal studies. The objective of this thesis is composed of two main topics: (i) the development of new MRI methodologies for proton lung imaging in healthy subjects, and (ii) the development of imaging protocols to monitor lung pathologies in animal models.

In proton lung MR imaging, the Cartesian-based imaging sequences are typically used for pulmonary disorder characterization in animal model studies. These characterizations are based on edema fluid detection, which is associated with many pulmonary disorders, such as COPD. A radial sequence with ultra-short echo-time is proposed to improve detection of disease indicators and to achieve better disease characterization. Subsequently, the radial sequence properties were used to develop novel imaging tools for longitudinal investigation of pulmonary diseases.

1.3 Main contributions

The main contributions of this thesis are summarized below:

- Implementation and validation of 'self-gating image reconstruction' using a signal derived from lung parenchyma during free-breathing respiration. The retrospective monitoring of the cardio-respiratory cycle was achieved using radial imaging features that involve the repetitive sampling of the k-space center. This method was proposed to simplify the imaging protocol for lung MRI in rodents. It allows for better control of image contrast and image synchronization at multiple phases of the cardio-respiratory cycle.

- Development of a new protocol allowing for reproducible detection of edema extent. This was achieved by using a specific radial sequence properties adapted to deal with a signal loss due to cardio-respiratory motion and pulmonary blood flow.

- Proposal of a new approach for early detection of inflammation by delineation of cellular infiltration. The detection of cellular infiltration involves susceptibility contrast, which changes in the presence of inflammation. This alteration is estimated quantitatively by determining the T2* parameter.

- Proposal of a novel protocol of quantitative assessment of emphysema using T2* parameters as an indicator of emphysematous lung changes.

1.4 Organization of the text

This thesis is organized as follows:

Chapter 2 includes the functional anatomy of rodents' lungs.

Chapter 3 presents the background of this thesis. In this section, the essentials of MR imaging and concepts concerning work presented in later chapters will be provided. An overview of the MR techniques used in pre-clinical research of the lungs will be given. Particularly, emphasis is placed on describing the principles of the radial UTE technique, as it is a major modality used in this thesis. A variety of radial sequence properties will be introduced and compared against the Cartesian technique. The second part concerns the details of the UTE sequence implementation on a Bruker scanner and specific sequence optimization adopted for lung imaging.

Chapter 4 concerns the development and the validation of the 'self-gating' method for motion synchronization using the radial UTE acquisition method. The principle of cardio-respiratory motion detection from the lung parenchyma is introduced. Next, the principle method of the self-gating technique is explained. The second part of this chapter will show the validation of this technique in both phantom and in-vivo studies.

Chapter 5 introduces new approaches for lung inflammation assessment in the experimental model of COPD induced by endotoxin-LPS. In this chapter, two different approaches characterizing the COPD model will be presented. The first approach concerns reliable, repetitive detection of edema fluids induced by LPS. In the second

approach, the feasibility of cellular infiltrations to the site of inflammation is investigated.

Chapter 6 includes a novel approach for a non-invasive and non-contrast-enhanced detection of emphysema, modeled by elastase administration.

Chapter 7 will gather general conclusions. Next, a discussion of future directions of this work will be presented.

2

Functional anatomy of the rodent's lungs

The purpose of this chapter is to provide the reader with basic terminology regarding the anatomy and physiology of the rodent's lungs.

The morphology of rat and mouse lung is shown in Figure 2.1 (62). The left lung consists of the one lobe and it is smaller than the right lung. The right lung consists of four lobes: three in a row (cranial, median, and caudal); and one (accessory lobe) against the diaphragm to the left of the midline.

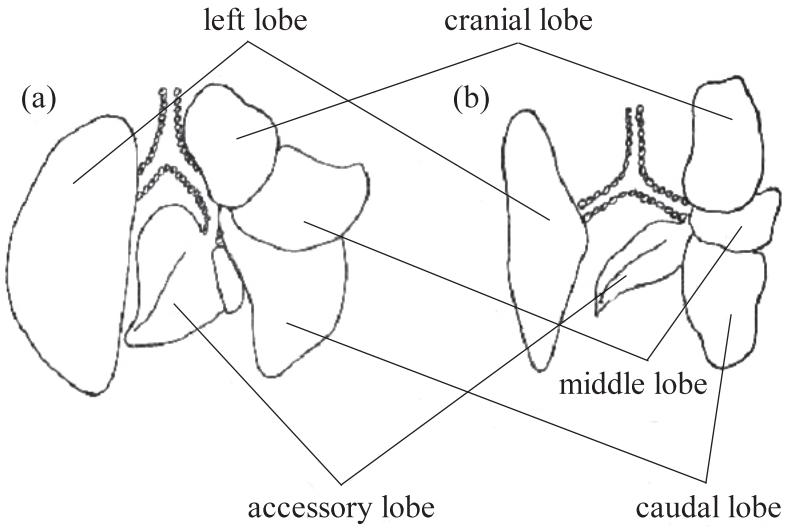

Figure 2.1: Anatomy of rat (a) and mouse (b) lung

2.1 Structure and function of the tracheobronchial tree

The tracheobronchial tree distributes air throughout the lungs. It can be divided into the conduction zone and the respiratory zone. The schematic representation of the of the bronchal tree together with pulmonary lobes of the brown rat lung is shown in Figure 2.2.

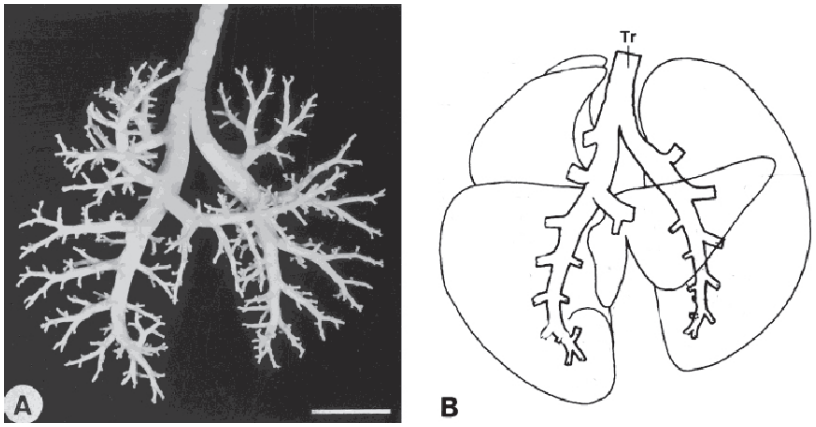

Figure 2.2: Silicon elastomer cast (a), and schematic representation of bronchi and bronchioles levels in the tracheobronchial tree (b) The image was adopted from (123).

The conducting zone consists of the trachea, bronchi and bronchioles. This zone serves as the conductor of air flow in and out of the respiratory zone where the gas exchange occurs. As seen from Figure 2.2, the trachea (Tr) bifurcates into two primary bronchi which enter the left and right lungs lobes and then proceed in a monopodal branching pattern. In rodents, sixteen or seventeen levels of branching occur. The terminal bronchiole is the smallest airway structure leading to the alveolar ducts which comprise the respiratory zone unit. The respiratory zone consists of alveolar ducts, sacs, and alveoli. In this zone, air and blood exchange oxygen and carbon dioxide. The pulmonary arteries accompany the tracheobronchial tree and their branching follows the bronchioles deep into the respiratory zone. As a result, each of alveolar sacs obtains its own individual branch of the pulmonary artery. The example of alveolar sacs surrounded by the network of capillary system are shown in Figure 2.3.

From histological point of view, the tracheobronchial tract is surrounded by a wall composed of four main layers: mucosa, submucosa, muscularis and adventitia (see Figure 2.4). The mucosa is lined with epithelium which consists of three main cell

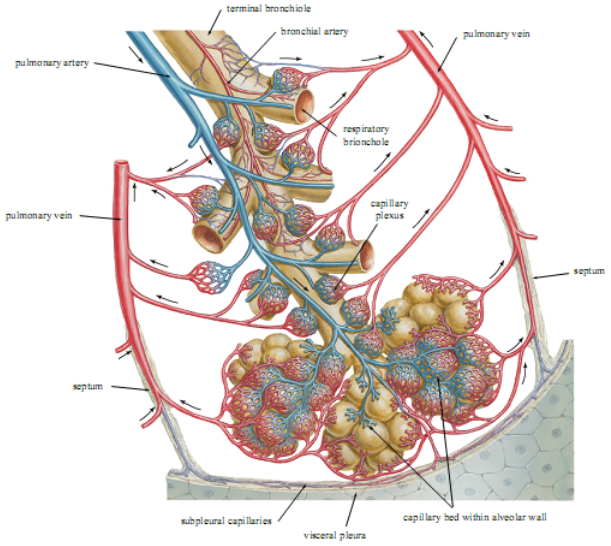

Figure 2.3: Terminal alveoli connected to the network of the capillary system. Adapted from [F. Netter, 2000].

types: noncillated secretory (Clara cells and Goblet cells), cillated and basal cells. The epithelium of the conduction zone secrets a mucous film which serves as a defense agent against airborne particles. Mucus is released throughout the conducting zone by Goblet cells. It is important to note that high numbers of Clara cells which is present in mice and rats epithelium helps in the clearance and at regulation of airways tension. The collagen fibers present in the submucosa prevent the tracheobronchial tree branches from bursting while inflated. The muscularis and adventitia serve as a support of the trachea and bronchi.

2.2 Lung physiology

2.2.1 Physiology of respiration

Respiration mechanics are determined by respiratory muscles such as: the diaphragm, external intercostal muscles, and abdominal muscles. Lung expansion and contraction is accompanied by superior-inferior movement of the diaphragm to change the vertical dimension of the chest cavity and anterior-posterior elevation and deflation of the ribs to increase and decrease the diameter of the chest cavity (see Figure 2.5 and Figure

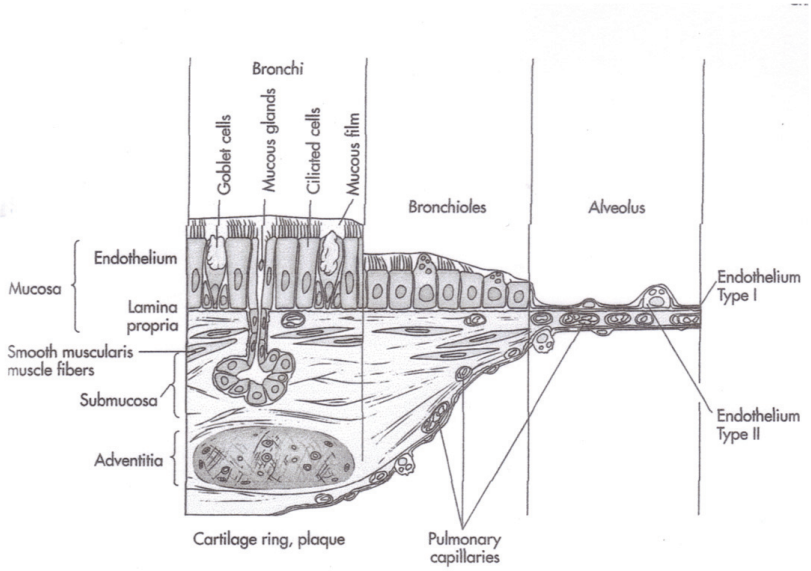

Figure 2.4: Tissue layers of the tracheobronchial tree. Reprinted from [D. Lindsay, 1995]

2.6).

The ventilation cycle is characterized by one inspiration and one expiration phase. In inspiration, the diaphragm contracts, the thoracic volume increases and the internal pressure decreases. Air flows into the lung following its pressure gradient. This results in increased size of the alveoli, thus decreasing the overall parenchyma density. Exhalation is caused by relaxation of respiratory muscle. In exhalation, the elastic fibers contract (decreasing lung volume), the pressure in the alveoli increases and the air flows out of the pulmonary structures increasing the parenchyma density.

During a respiratory cycle, the lung volume and the parenchyma density change with the respiratory phases. The volume curve for the lungs during tidal breathing in a mouse can be derived following Segars (105). A typical curve is shown in Figure 2.7. The shape of the respiratory curve can be approximated with the cosine function as described by Lujan (73):

$$z(t) = z_0 - A \cdot cos^{2n}(\frac{\pi \cdot t}{\tau} - \phi),$$

where z(t) is the position of the diaphragm in a superior-inferior direction, z_0 - a constant value, and ϕ - period and phase of the respiratory cycle, n - the parameter

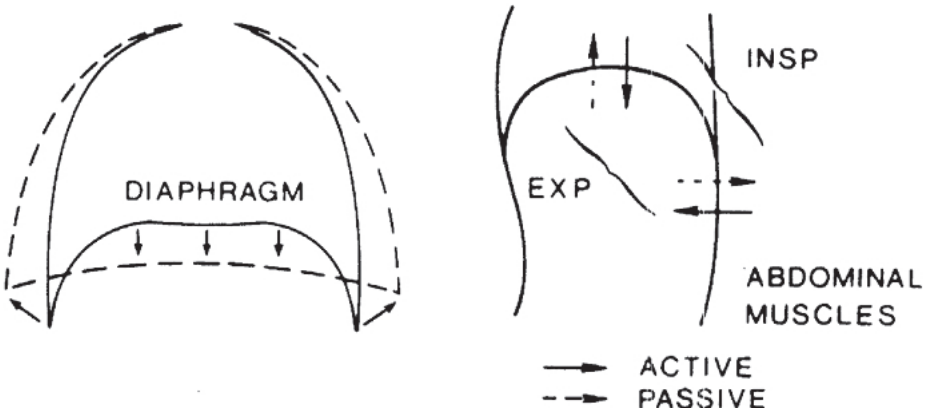

Figure 2.5: Motion of the diaphragm during respiration. During inspiration, the diaphragm contracts increasing the volume of the thoracic cavity. During expiration, the diaphragm relaxes decreasing the volume of the thoracic cavity. Reprinted from [J. West 1995]

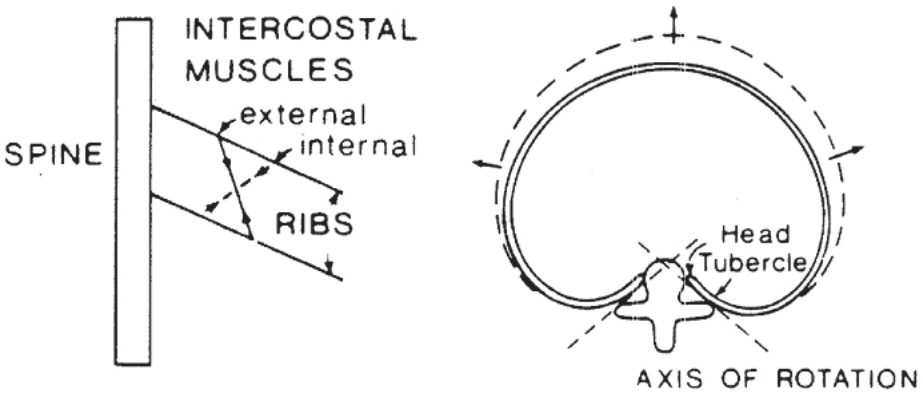

Figure 2.6: Motion of the ribs during respiration. The ribs rotate outward and upward during inspiration increasing the volume of the thorax. Reprinted from [J. West 1995]

influencing flatness and steepness of the curve, and A - amplitude of the respiratory cycle.

2.2.2 Defense mechanisms

The respiratory defense system constitutes the clearance mechanism in the conduction zone of the tracheobronchial three and the alveolar clearance mechanism represented by the mononuclear phagocyte system.

The mononuclear phagocyte system of the lung consists of cells in three categories:

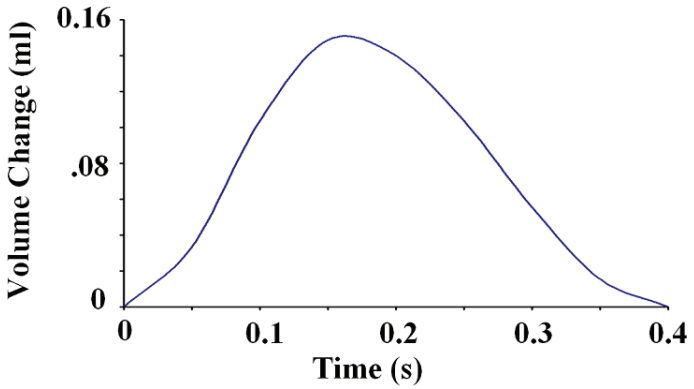

Figure 2.7: Change in lung volume during tidal breathing in a mouse (105). The period of the respiratory cycle for normal tidal breathing in a mouse is approximately 0.4 seconds and the volume change is 0.15 ml [*Biology of the Laboratory Mouse*, E. Green 1996].

airway and alveolar macrophages, interstitial macrophages and in some species, intravascular macrophages (25) (see Figure 2.8). Pulmonary intravascular macrophages promote lung inflammation and are found in ruminants, horses, pigs, cats, and dolphins, (4), (114), (128), (127) but not in primates, rats and mice (17), (40), (114).

In all mammals, the interstitial and avleolar macrophages contribute to phatocytosis of air-borne particles. In those species with intravascular macrophages, all particles circulating in the blood can potentially be phagocytized by intravascular macrophages before entering the interstitium (71). Those species without the presence of intravascular macrophages, can have the ability to recruit them with hepatopulmonary syndrom.

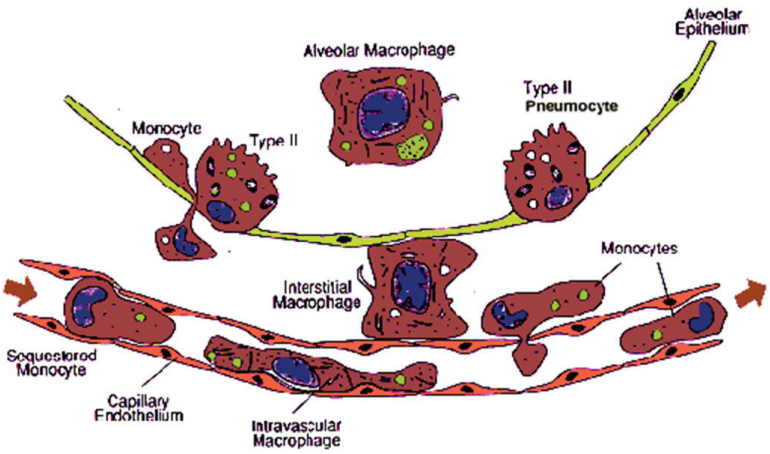

Figure 2.8: The mononuclear phagocyte system of the lung.

3

Application of MRI techniques to a rodent's lung

3.1 MR characteristics of the lungs

The lung is one of the most challenging organs to image by MRI and usually appears black in MR images (See Figure 3.1). The major reason for this is its unique morphology, as the lung consists of air-filled alveoli surrounded by alveolar walls. The alveolar structure is shown in Figure 3.2.

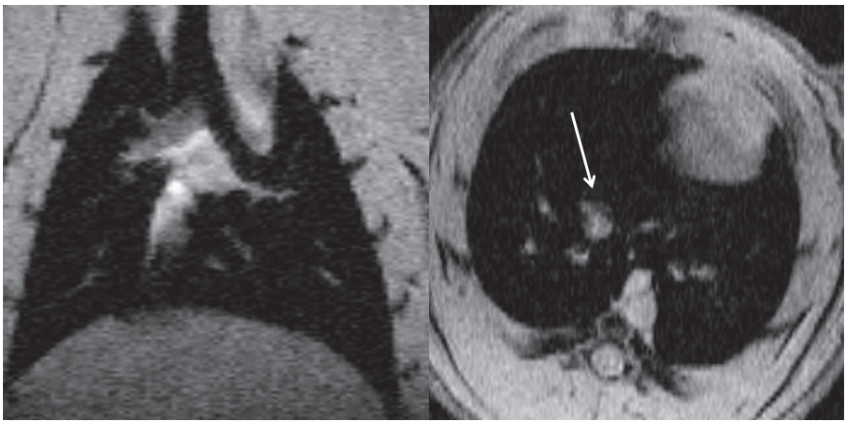

Figure 3.1: Image of a rat's thorax in the coronal (a) and axial (b) plane acquired with a gradient-echo sequence. TE was equal to 2.1 ms. Note, the visibility of the pulmonary structure is limited to vessels - indicated by the arrow.

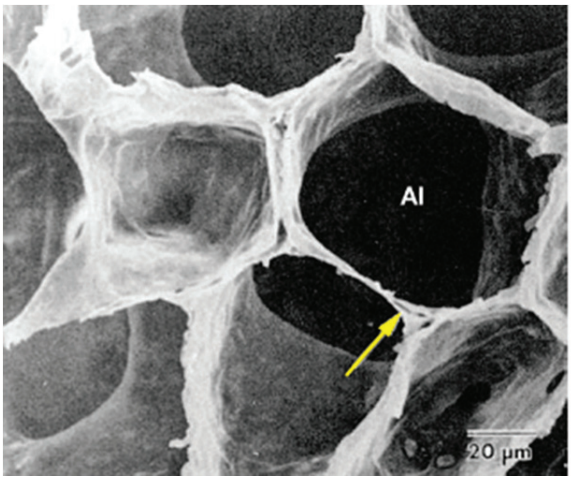

Figure 3.2: Alveolar structure of the lungs. The arrow indicates the alveolar wall surrounding the air-filled alveoli (Al). Air constitutes 80% of the lung parenchyma. Adapted from Albertine 1996.

- **Density**

The air-filled alveoli constitute the greatest part of the lung's volume. Therefore, the density of protons, which are the source of MR signal, in the lung parenchyma is very low. Consequently, the MR signal emitted from the lung is weak.

The proton density depends on the degree of lung inflation. In humans, at the end of expiration, proton density is about two times higher (0.3 g/ml) than at the end of inhalation (0.15 g/ml) (45). This change is a source of the amplitude modulation of the NMR signal during respiration.

The NMR signal from the lung is mainly emitted from nonparenchymal structures such as blood vessels, airways, lymph nodes, and connective tissue. In humans, the blood fraction in the lungs comprises 400 ml which consists of about half of the total pulmonary tissue volume (900 ml) (2). The remaining tissue volume is represented by structural elements for lung support and for the alveolar walls. Notably, the vascular and structural elements comprise a small lung's volume fraction, compared to gas volume consisting of about 2.5 L.

- **Tissue heterogeneities**

Multiple air/soft tissue interfaces inside the lungs produce local magnetic field inhomogeneities (termed "field gradients") that result in the dephasing of the already

weak MR signal due to T2* decay. The T2* relaxation time is inversely proportional to the applied magnetic field. For instance, at 4.7 T, a magnetic field commonly used in small animal scanners, T2* in the lung parenchyma is about 500 μs (9). Thus, lung parenchyma usually appears dark in MR images acquired with a conventional echo time (m̃illiseconds) imaging sequences.

T2* relaxation time can be determined from a gradient echo experiment in which the MR signal is acquired at different echo times:

$$S(TE) \approx S(t=0) \cdot exp\left(\frac{-TE}{T2*}\right).$$

Where: 1/T2* = 1/T2 + 1/T2'. Here, 1/T2' is a contribution to the relaxation time due to local field inhomogeneities. It results from the external B_0 field's defects and the internal gradients of the lungs. By locally mapping the T2* within the lungs, one can measure the lung contribution which might reflect variability in alveolar size. For instance, Cutillo at al. (30) showed the changes of T2* between inflated and compressed lungs. The shorter magnetization decay in the case of inflated lungs, was consistent with a theoretical simulation based on a spherical-shell model (34). These results suggest that T2* of the lungs may reflect morphometric features of the micro-architecture of the lung at the alveolar level (30), thus they can be used to diagnose some chronic obstruction pulmonary diseases like emphysema.

- **Cardio-respiratory motion**

Breathing and cardiac motions are two major sources of signal change in lung MR imaging. It has been shown that changes in lung volume cause proportional changes in MR signal intensity (6). Thus, the NMR signal of the lung, proportional to the proton density, changes due to breathing and scales linearly with lung volume.

Additionally, taking into consideration the periodic signal changes caused by blood perfusion during the cardiac cycle, the total signal intensity changes in the thoracic cavity can be described as (7):

$$i(t) = i_0 - A_r \cdot cos^{2n}(\frac{\pi \cdot t}{\tau_r} - \phi_r) + A_c \cdot sin^{2n}(\frac{\pi \cdot t}{\tau_c} - \phi_c),$$

where i_0 - constant value, τ_r and ϕ_r - period and phase of the respiratory cycle, τ_c and ϕ_c - period and phase of the cardiac cycle, n, m - parameters influencing the shape of the curve, and A_r and A_c - amplitude of both cycles.

Concerning the image display, the motion effect of the structures within the thoracic cavity during the breathing cycle and the cardiac motion is twofold. First, it causes blurring of pulmonary and vascular structures. Second, it generates ghosting of external structures such as subcutaneous fat. Both effects degrade the image spatial resolution and are associated with image artifacts (see Figure 3.3).

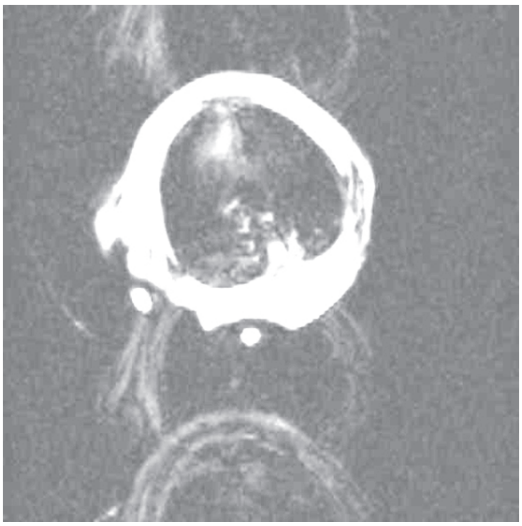

Figure 3.3: Gradient-echo image (TE/TR=2.1/7.8, 50 signal averages, 256x256 matrix) of mouse thorax showing blurring and ghosting artifacts.

3.2 Motion considerations

Cardio-respiratory motion artifacts are more evident in small animals, as their cardio-respiratory rates are up to an order of magnitude higher than in human subjects. Table 3.1 gathers several biological parameters characteristic for humans, rats and mice. For example, the rat heart rate of 300 bpm requires a five-fold increase in acquisition speed over the human heart rate of 60 bpm to capture the same relative phases of the cardiac cycle (18).

Regarding respiratory motion, usually in human studies the breath can be voluntarily held back and a fast pulse sequence acquisition can be performed whilst the breath is held in the acquisition window of approximately 20-30 seconds (46). This condition cannot be achieved in animal studies.

	Human	Rat	Mouse
Heart rate (bpm)	60	300	700
R-R interval (ms)	1000	200	80
Blood volume (mL)	5200	13.5	2
Respiratory rate (breaths/minute)	12	60	160

Table 3.1: Comparison of physiological parameters in humans, rats and mice.

In general, there are two acquisition approaches which allow one to deal with respiratory (and cardio-respiratory) movement in studies of small animals. In the first, the animals are allowed to breathe spontaneously and the potential movements are suppressed by means of signal averaging or navigator techniques. The second is based on the synchronization of movement with acquisition (e.g scan-synchronous ventilation) with the use of a mechanical ventilator. Below a short description of the two mentioned techniques will be provided.

Free-breathing methods:

Signal averaging: The averaging method uses the inconsistency of motion artifact amplitude to reduce overall image ghosting.

Navigator or self-gating techniques: The navigator technique consists of repeatedly measuring a partial set of k-space data that is processed to track the motion. Two types of navigators can be distinguished: the explicit (e.g gradient moment nulling), and implicit (e.g. using radial projection, PROPELLER method (95), multi-coil navigator). The navigator techniques acquires a partial set of k-space data (usually collected when passing through the origin of k-space) which is processed to track the motion. The navigator techniques were applied in numerous studies for breathing and cardiac motion synchronization in patient and animal studies.

Forced-breathing method

Scan-synchronous ventilation: A key feature of this technique is the use of a mechanical ventilator. A breathing valve that is attached directly to the endotracheal tube allows for independent control of inspiratory and expiratory phases of ventilation(47) (See Figure 3.4). With the use of a ventilator, the imaging sequence is triggered at a well defined moment of the respiratory cycle. One of the major disadvantages of using a ventilator is its possible interference with patho-physiology of the disease and its caus-

ing lung injury when applied repeatedly. For example, it has been reported that the use of the ventilator caused pulmonary edema and hypoxemia (59). Additionally, the use of all synchronization method introduces magnetization instabilities due to variable TR of the imaging sequence, which may alter the image contrast and influence image quantification.

Figure 3.4: Scan-synchronous ventilation set-up. Courtesy of Angelos Kyriazis, Instituto de Estudios Biofuncionales, Universidad Complutense de Madrid, Spain.

The cardiac motion can be reduced by means of ECG synchronization. An electrocardiogram (ECG) is a plot of voltage versus time which indicates the electrical activity of the heart. The example of an ECG plot is shown in Figure 3.5. The waves indicated in Figure 3.5 have physiological interpretations. For example, the RQS complex indicates the activation of the ventricles and this complex is used for the ECG synchronization of MR images.

The cardiac cycle can be divided into systole and diastole. Systole corresponds to the heart contraction. In the ECG plot, it covers the period from RQS complex to the end of the T wave. Diastole corresponds to the heart dilatation.

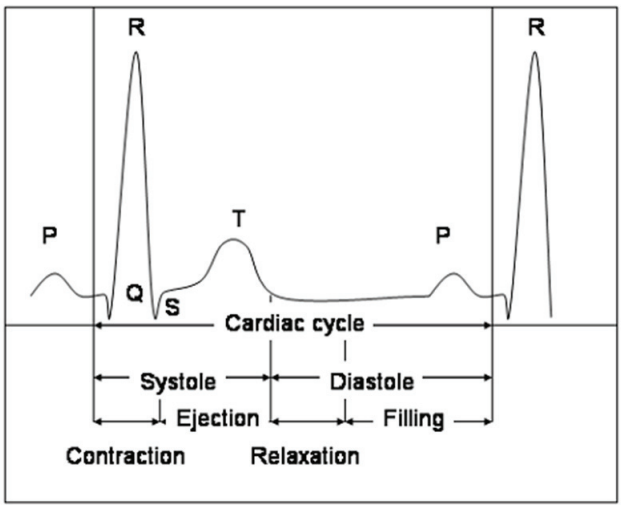

Figure 3.5: Electrocardiogram.

3.3 MR imaging methods for lung parenchyma

3.3.1 The concept of k-space

MRI techniques are usually described using k-space formalism. K-space is defined as the spatial frequency domain and represents the signal before an inverse Fourier transform is applied to form the image. More specifically, spatial frequency vector k describes the time integral of the magnetic field gradient vector experienced by the transverse magnetization during an MR experiment (during and before acquisition).

$$k(t) = \frac{\gamma}{2\pi} \int_0^t G(t')dt'$$

where G=∇B_0, B_0 is a static magnetic field and γ is a gyromagnetic ratio of the considered nucleus ($\gamma/2\pi$ for protons is equal to 42.576 MHz/T). The time origin (t=0) corresponds to the time at which transverse magnetization is created (which is achieved by means of a RF pulse).

3.3.2 K-space trajectory

The k-space trajectory (ordering scheme) can have an arbitrary form. Each scheme has its advantages and disadvantages and the appropriate choice will depend on the type of desired applications (for example temporal resolution versus spatial resolution). For an

extensive description of different k-space sampling trajectories, the reader is referred to the MRI handbooks (for example Handbook of MRI pulse sequences, Bernstein 2004). Depending on the shape of the k-space trajectory, the sequences can be divided into Cartesian and non-Cartesian. In the Cartesian encoding scheme, the sampling points are uniformly distributed on the rectangular grid and the Fast Fourier Transform is applied to reconstruct the image. In the non-Cartesian schemes, such as radial k-space sampling, the points lie on radial spikes emerging from the k-space center and additional steps are required (before FFT is applied) for image reconstruction (see section 3.3.4). The example of the Cartesian and radial encoding scheme is shown in Figure 3.6.

Depending on the sampling scheme, the MR signal can be detected either in the form of a free induction decay (FID) or in the form of an echo. The free induction decay is the signal acquired right after the RF excitation. The echo signal is obtained after the precessing spins are refocused by means of a second RF pulse or a gradient pulse. The moment when rephrasing is completed is called the echo time (TE).

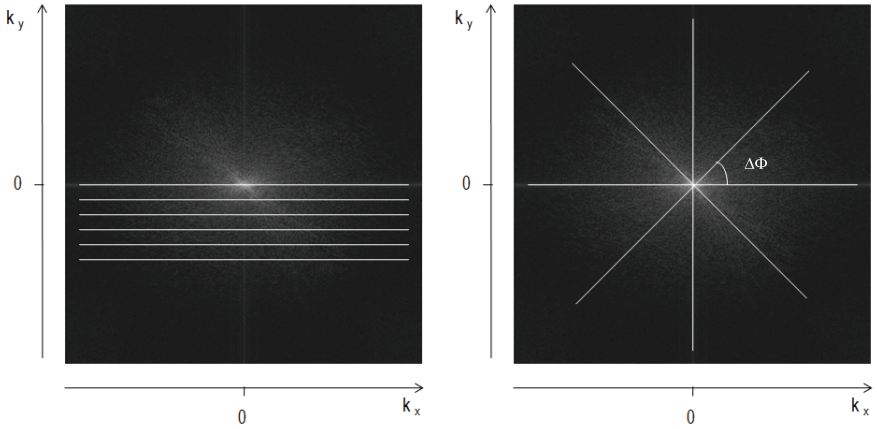

Figure 3.6: Cartesian (a) and radial (b) k-space scheme

- Cartesian k-space sampling

Conventional MR experiments applied to the lungs use Cartesian k-space sampling. In Cartesian k-space sampling, each k-space line is acquired after each RF excitation which is repeated with repetition time TR (see Figure 3.7).

The desired field of view (FOV) of the image and its spatial resolution, δr, determine the set of points used to sample the k-space. The sampling step size (sampling frequency), δk, is calculated to be small enough to avoid aliasing artifacts, using the

Nyquist criterion. The k-space range, ΔK_{max} must be large enough to achieve high spatial resolution δr. This leads to the following conditions:

$$\delta k \leq 1/FOV$$
$$\Delta K_{max} \geq \frac{1}{\delta r}$$

Among these traditional MRI techniques, the FLASH (Fast Low Angle SHot) sampling scheme proved to be particularly useful in proton lung imaging.

The schematic of the FLASH acquisition sequence is shown in Figure 3.7. FLASH is a multi-shot gradient-echo sequence. Following each excitation, the echo signal is acquired at the echo time TE. Usually, TE obtained with gradient-echo is of an order of milliseconds. The train of RF pulses applied with gradient selective slice G_z is repeated for each encoding gradient G_y with repetition time TR.

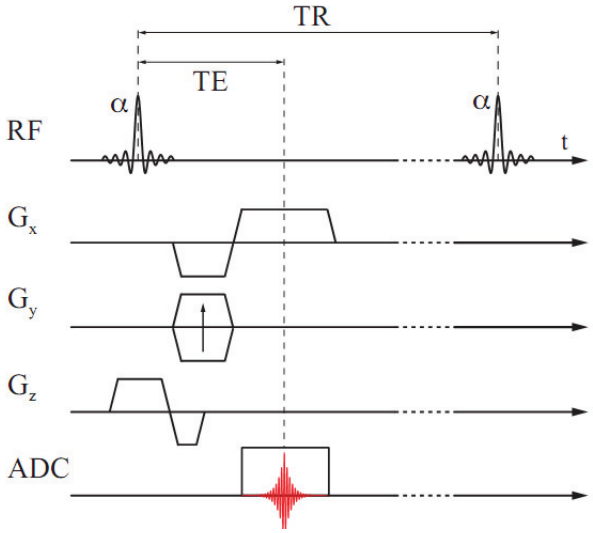

Figure 3.7: Chronogram of FLASH (gradient-echo) imaging sequence.

- UTE radial k-space sampling

Radial acquisition was the first MRI k-space trajectory, developed in 1973 by Lauterbur (68). Lauterbur called it zeugmatography (from the Greek word "zeugma", meaning "that which joins together", because of the joint use of static magnetic and RF electro-magnetic fields in the imaging process). Several names were introduced for this

technique, such as: projection and radial acquisition. The radial acquisition was first used for lung parenchyma imaging in human extracted lungs in 1991 by Bergin (15). Soon after, Gewalt et al. (39) showed its application in rodent lung imaging. Despite these pioneering studies, proton imaging using radial acquisition has not been widely applied to clinical or pre-clinical investigation of lung diseases. Recently, due to a renewed appreciation of the positive contrast allowed by a very short echo time (TE) achievable with the radial acquisition, a revival of interest in this technique - especially in the Ultra Short Echo-Time (UTE) imaging sequence, has been observed.

In radial acquisition it is assumed that projections are equally distributed over the k-space center with angular step, $\Delta\Phi$ (see Figure 3.6). The maximum k-space radius k_{max} is determined by the desired spatial resolution, δr. The sampling step size $\Delta\Phi$, is limited by the Nyquist criterion, described as follows:

$$k_{max} \cdot \Delta\Phi \leq \frac{1}{L}$$

where L is the FOV and k_{max} − the maximum k-space radius.

To cover π rad, the number of spokes, Ns required to satisfy the Nyquist criterion is:

$$N_s = \frac{\pi}{\Delta\Phi} = \pi \cdot k_{max} \cdot L$$

Interpreting the Nyquist criterion in terms of evenly spaced projections in k-space, it can be stated that the distance or the azimuthal gap between samples in an azimuthal direction, $\Delta\Phi$, must not exceed the sample distance in radial direction. For example, when 128 samples in radial direction are acquired to satisfy the Nyquist criterion, 400 azimuthally spaced directions over 2π rad are required.

The radial pulse sequence diagram is shown in Figure 3.8. After a conventional slice excitation, the two gradients G_x and G_y are turned on simultaneously. This results in filling in k-space data with radial spokes starting at k=0 with angular range of $0 - 2\pi$. Each radial projection is acquired after each RF excitation with the repetition time, TR. The signal induced by transverse magnetization M_{xy} is sampled by the digitizer (ADC) at constant time intervals, resulting in a set of data points along each projection. The amplitudes of the G_x and G_y gradients are incremented in equal steps, resulting in the gradient waveforms defined as follows:

$$G_x = G_0 \cdot cos\Phi$$
$$G_y = G_0 \cdot sin\Phi$$

where G_0 is the maximum readout waveform amplitude (see Figure 3.8). It is assumed that the sampling is performed in the physical XY plane.

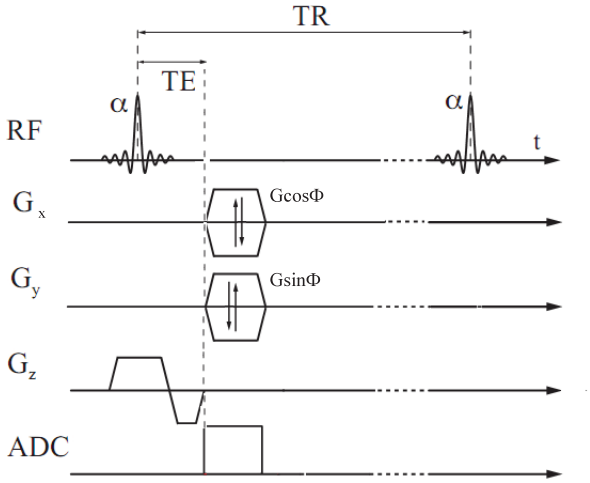

Figure 3.8: Radial sequence chronogram.

Concerning the k-space filling, full or partial (with the range of 0-π) echo data collection using the radial technique is possible. The use of the partial echo (with each spoke starting at k-space center) approaches results in the acquisition of the free induction decay (FID) which is recorded immediately on completion of the slice selective excitation. Contrary to the full echo acquisition, since the FID us encoded directly, there is no echo in this case. The echo time is defined then as an interval between the end of the slice selective excitation and the first point of the recorded FID. It is this interval that must be minimized in order to improve signal detection from lung parenchyma.

3.3.3 RF excitation scheme

In an MR experiment, an RF pulse excitation and a magnetic field gradient is applied to choose a slice from an imaged object volume. The typical excitation scheme is shown in

Figure 3.9. It consists of a slice-selective RF excitation followed by a gradient-refocusing interval. The purpose of the slice refocusing gradient pulse is to refocus slice dispersion. This slice refocusing interval requirement translates into long echo times.

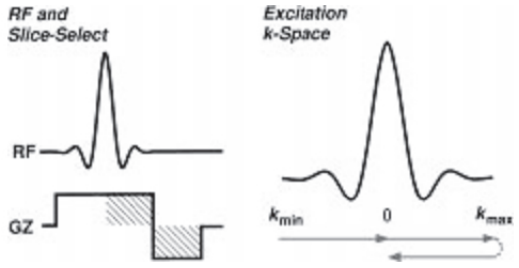

Figure 3.9: Conventional excitation scheme.

There are many approaches which permit us to minimize the echo time intervals. One can begin the data acquisition during gradient ramping and apply a non-selective, asymmetric (83) or half-pulse RF excitation (82). With the use of half-pulses, one can achieve a minimum TE in the order of 8μs (32) restricted only by hardware limitations. An example of a half-pulse excitation scheme using the half-sinc pulse is shown in Figure 3.10 (reproduced from (82)).

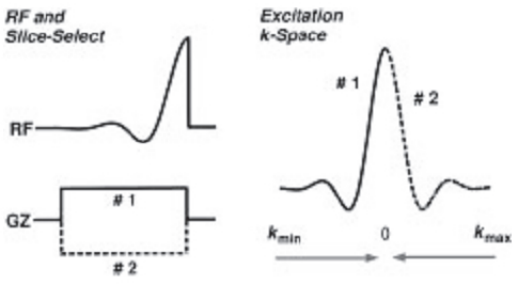

Figure 3.10: Half-pulse excitation scheme.

Figure 3.11 shows the UTE pulse sequence combined with a half pulse RF excitation. In such excitation schemes two RF excitations are used. The first excitation is performed in the presence of the positive slice selection gradient. Then the polarity of the slice selection gradient is inversed and the second RF pulse is executed. Data acquisition is performed after each half-excitation. The same readout gradients are applied for each pair of half-excitations and the signals of the two individual measurements are

added. The drawback of the presented scheme is the extended acquisition time. Since the slice selection requires double excitation for each projection, the acquisition time is doubled. Therefore, the total measurement time associated with the above scheme is given by $2 \cdot TR \cdot N_s$,where TR is a repetition time of the imaging sequence and N_s, number of spokes.

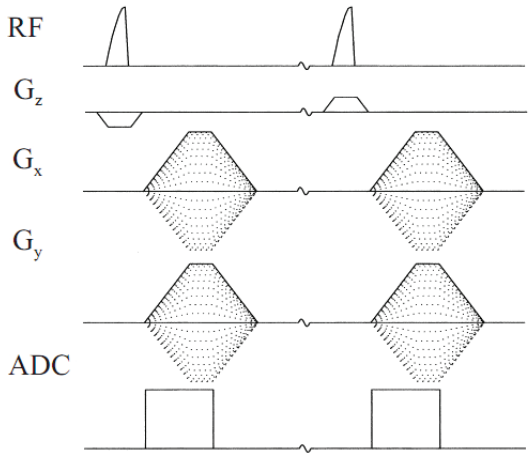

Figure 3.11: Radial sequence chronogram with the half-pulse excitation. Adapted from (121)

Note that the studies presented in chapters 4, 5 and 6 were performed using a conventional excitation scheme in which acquisition was started right after a short refocusing gradient.

3.3.4 Image reconstruction using gridding algorithm

In the case of radial sampling, MRI data is acquired along a non-uniform grid. Thus, directly applying the Fast Fourier Transform (FFT) algorithm to reconstruct the image is not possible. For image reconstruction, a non-uniform discrete Fourier transform (DFT) could be used, however it requires a considerably longer computation time (75). Instead, it is much more efficient to resample the data on a uniform grid, by means of an interpolation, and then perform the FFT. The entire reconstruction process, including the FFT step, is called gridding. The gridding algorithm can be divided into three main steps, of which brief descriptions are given below:

1. Density compensation of non-uniformly sampled data

In order to compensate for the non-even spacing of the data points in k-space, the radial MR data needs to be multiplied by a density compensation function (DCF). This function can either be calculated analytically (80) or obtained by geometrical consideration of a particular k-space trajectory using the Voronoi diagrams (100). The analytical method relies on the transformation of the coordinates from a non-uniform to a uniform grid. This approach leads to a density compensation function that is equivalent to the Jacobian of the transformation. In the case of radial encoding, the numerical representation of the density compensation function (w) is given by the following formulae:

$$w(k_r[j], \Phi[j]) = \frac{2 \cdot \pi \cdot k_{max} \cdot j}{(N_s - 1)^2 (N_r - 1)} \quad for \quad 1 \leq j \leq N_s - 1$$
$$w(k_r[j], \Phi[j]) = \frac{\pi \cdot k_{max}^2}{(Ns - 1)^2}$$

where N_s denotes the number of sampling points on each radial projection, N_r is the number of projections, and j is the sample index. $0 \leq k_r \leq k_{max}$ and $0 \leq \Phi \leq 2\pi$.

2. Convolution with a gridding kernel

After weighting the sampled data, each data point is convolved with a gridding kernel and the results are sampled and accumulated on a Cartesian grid. The kernel shape is usually chosen to be a Kaiser-Bessel function as it gives the optimal results with respect to computation time and reconstruction errors (52). The Kaiser-Bessel function is defined as:

$$C(k) = \begin{cases} I_0 \left[\frac{\pi \cdot L \cdot a}{2} \sqrt{1 - \left(\frac{2k}{L} \right)^2} \right] / L & for \quad -L/2 < k_{max} < L/2 \\ 0 & elsewhere, \end{cases}$$

where I_0 is the zero−order modified Bessel function, and L and a are kernel window parameters. The convolved data are resampled on a Cartesian grid optimized for a fast Fourier transform.

3. Deapodization

Once the k-space data is resampled on the Cartesian grid, the FFT can be applied to reconstruct the image. However, the consequence of convolution in the Fourier domain has to be taken into consideration; the transformed data must be divided by

the Fourier transform of the convolution kernel. As the result of this operation, the aliasing artifacts at the edge of the FOV are amplified. It was proved beneficial to use an oversampled Cartesian grid to reduce the errors from the aliasing lobes that appear near the edges of the image ((89), (52)). As a result of oversampling, the FOV is increased. To preserve the original FOV size, the image should be scaled ignoring the outer portion of the enlarged FOV.

Gridding represents one of methods for data reconstruction from non-Cartesian k-space trajectories. Radial MR data can be also reconstructed using a filtered back-projection (65).

3.3.5 Properties of radial acquisition

The radial acquisition was shown to have the advantages over a Cartesian encoding when imaging of moving object is of concern (42). The effect of motion is particularly important in abdominal imaging where breathing, cardiac or peristaltic movement can occur.

In Cartesian imaging, the motion artifacts are manifested as blurring and ghosting appearing in the encoding gradient direction, G_y. The typical ghosting artifacts in the image of the thorax acquired under spontaneous breathing conditions using a gradient-echo sequence (FLASH) are shown in Figure 3.12.

It was shown by Glover and Pauly (42) that an improved image quality with radial encoding with respect to motion artifacts can be obtained. This improvement results from three factors characteristic of radial encoding: (i) the motion artifacts manifest themselves as radial streaks with low amplitude near the moving object, (ii) streaks emanate perpendicularly to the surface of the moving object (often appearing in the image periphery) and (iii) oversampling of the k-space center results in signal averaging of low spatial frequencies.

Another robust method for motion artifact reduction is signal averaging (see section 3.2). Specifically, it was shown by Beckmann et al. (8) that 40-60 signal averages are sufficient to eliminate motion artifacts from images of freely-breathing animals acquired using a Cartesian (gradient-echo) imaging method.

The properties of a radial acquisition versus that proposed by Beckmann et al., based on the Cartesian scheme, with regards to motion artifacts, were investigated

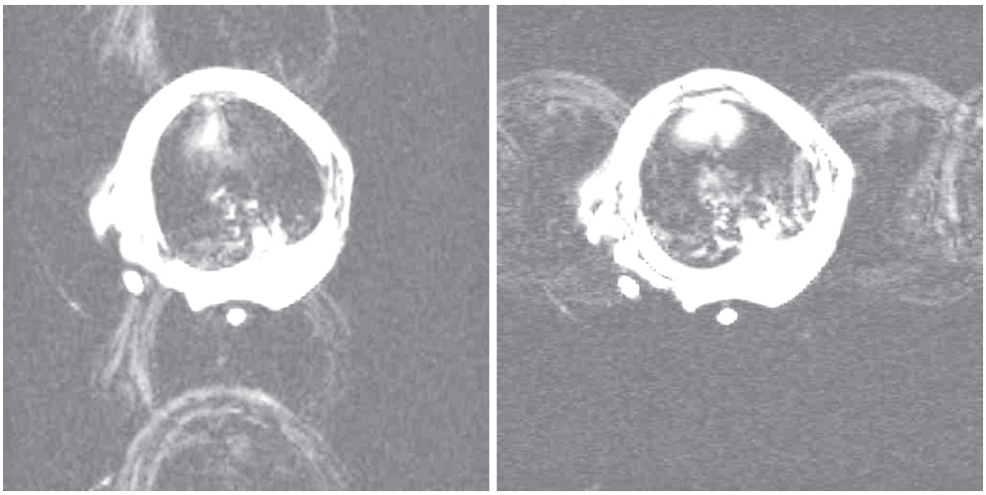

Figure 3.12: Gradient-echo thorax images of a free-breathing mouse. The contrast and luminosity were changed in order to emphasize the motion artifacts. The frequency encoding gradient was set up in the direction parallel (left) and perpendicular to the diaphragm motion (right). Despite 40 signal averages, severe artifacts in thoracic cavity are prominent. Other sequence parameters were: TR/TE=2.1/7.8 ms, flip angle=15 deg, slice thickness=1 mm.

experimentally. For this purpose, we designed a protocol in which we compared the effeciency of motion artifacts reduction using these two techniques.

In the study, an oscillating phantom consisting of the water filled syringe attached to an oscillating piston was designed. In order to verify the efficiency of the averaging method, averaged acquisitions performed using the Cartesian and radial schemes were optimized. The Cartesian technique was optimized following Beckmann et al. (8). The elements of radial sequences optimization with regards to motions can be found in section 4.9.1. The detailed sequence parameters are given below (Table 3.2):

Figure 3.13 presents images of the oscillating phantom, with an amplitude of 3 mm and a rate of 30 cycles/min, acquired using the gradient-echo and radial technique. Application of 50 signal averages in the case of gradient-echo sequence and 20 signal averages in the case of radial technique did not completely eliminate image artifacts due to the motion; this can be observed in the severe blurring of the image. It can be noticed however, that in the case of the gradient encoding scheme, these image artifacts significantly obscure the image making its correct interpretation impossible.

Auto navigation

	Gradient-echo	UTE
Matrix size	128x256	400 projection/128 samples
TR/TE ms	7.8/2.1	80/4.5
Slice thickness mm	1	1
Bandwidth kHz	100	64
Flip angle deg	15	30
Number of signal averages	50	20

Table 3.2: Gradient-echo and UTE sequences parameters used for the assessment of image quality in the moving phantom study. Number of signal averages was chosen to obtain the best image quality with regards to the motion artifacts.

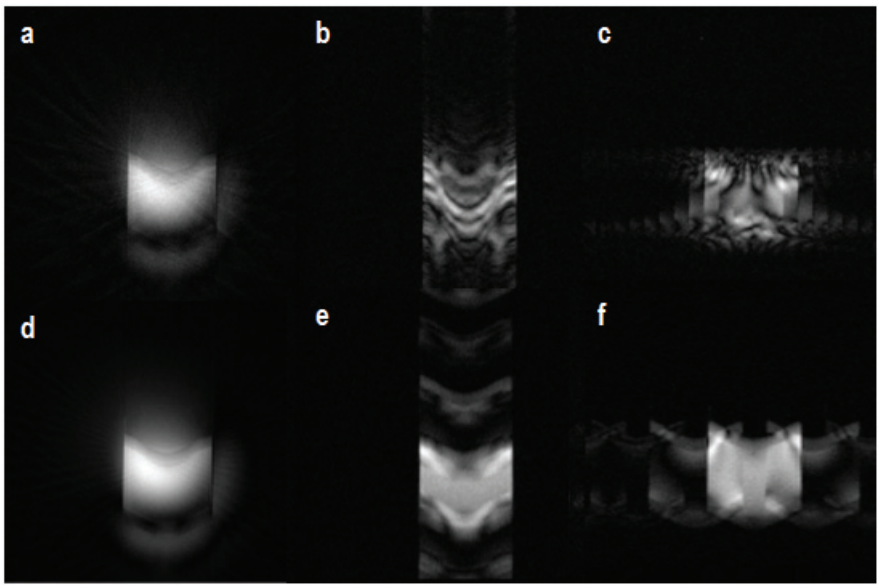

Figure 3.13: Averaging efficiency of the radial (a,d) and Cartesian acquisition (b,c,e,f) estimated in case of oscillating phantom. No averaging (a, b, c) and 50 averages (d, e, f) was applied. The gradient-echo acquisition was performed with two different phase-encoding directions (along the motion axis, middle, and perpendicular to the motion direction, right images).

While discussing the properties of radial acquisition, it is not possible to omit its self-navigation properties. The navigator consists of each projection crossing the k-space center at each RF excitation which can be used to monitor, or correct for, motion. For a more detailed description of the self-gating technique, the reader is referred to chapter

4.

Sensitivity to the off-resonance effect

Radial encoding is sensitive to off-resonance effects such as susceptibility differences or chemical shift. The nature of artifacts caused by the off-resonance effect is shown in Figure 3.14. The off-resonance displacement in the radial technique occurs in all directions, resulting in blurring. This blurring appears as a ring surrounding the imaged object, as shown in Figure 3.14. The frequency shift corresponds to the chemical shift between water and lipids produced in 3T and 4.7 T magnetic fields, respectively. One can minimize this sensitivity by using a wider acquisition bandwidth; however the reduced SNR at higher bandwidth is evident. For most of our experiments the bandwidth of 64 kHz was used as a reasonable operating point to optimize the image SNR.

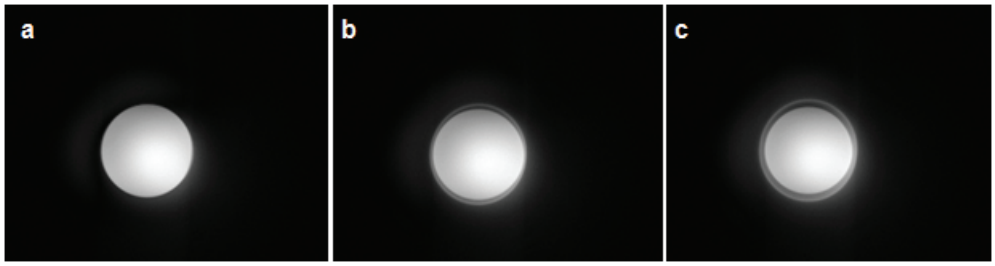

Figure 3.14: Axial images of water-filled syringe acquired in resonance a), and off-resonance conditions corresponding to the frequency shift of fat with respect to water at 3T (440 Hz)(b) and 4.7 T (700 Hz) (c). Acquisition was performed with a bandwith of 64 kHz

3.4 Methods development

3.4.1 Sequence implementation

The radial UTE sequence was implemented on two 4.7 T MR scanners: one in the CREATIS-LRMN laboratory (Lyon, France) and another at Boehringer Pharma (Biberach, Germany), both interfaced with a Bruker platform (Paravision environment). A brief overview of both systems is presented in Table 3.3.

The chronograms of the radial sequence implemented on the Bruker platform are shown in Figure 3.15.

Table 3.3: Description of the imaging platform.

Parameter	Lyon	Biberach
Field strength	4.7 T	4.7 T
Magnet manufacturer	Oxford (UK)	Bruker (Ettlingen, Germany)
Gradient manufacturer	Oxford,	Magnex Bruker (Ettlingen, Germany)
gradients slew rate GSR (max strength/rise time)	1086 mT/m/ms	800 mT/m/ms
gradients maximal amplitude	250 mT/m	200 mT/m
minimum TE achieved with a Gaussian pulse	450μs	670μs
operating system	Paravision 4.0/5.0	Paravision 4.0/5.0

The UTE sequence was programmed using methods developed for FLASH. The arrays of G_x and G_y gradients were programmed to obtain the radial encoding scheme. The interface of the UTE sequence is shown in Figure 3.16.

Each of the implemented sequences has the possibility of performing:

- Multi-slice acquisition
- Multiple repetitions allowing repeated sweeps of the sequence
- Signal averaging allowing signal accumulation after each excitation
- Segmented inversion recovery module implemented for T1- weighting
- Arbitrary slice geometry
- Time varying spoiler

Moreover, two different order schemes with evenly spaced projections were implemented. In the first scheme, the projections were spaced sequentially with an increment of $\Phi = 2\pi/N_s$. In the second scheme, consecutive projections were obtained by altering the sign of the imaging gradients before each angle increment. In this projection order,

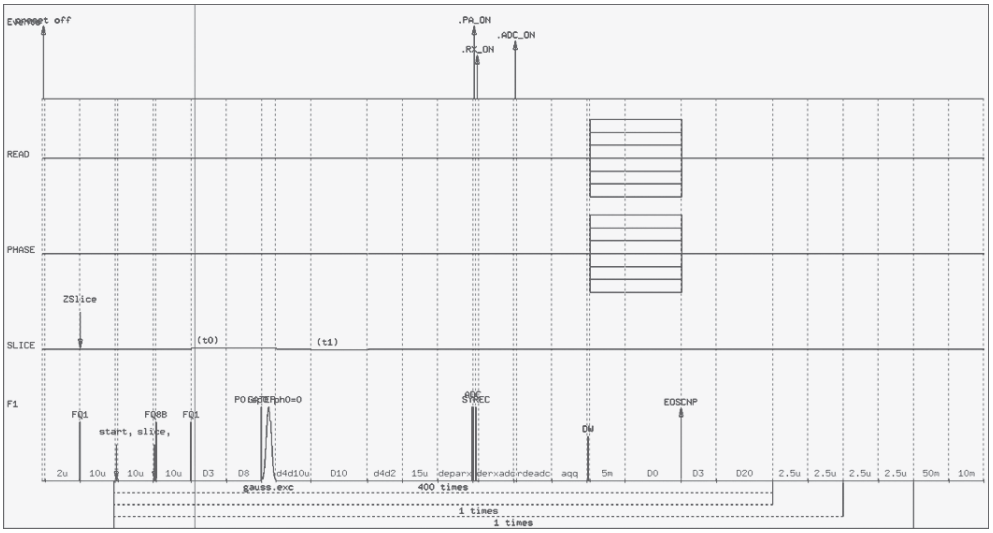

Figure 3.15: Chronogram of the radial sequence implemented on the Bruker platform using Paravision environment.

the k-space is first filled with even projections followed by all odd projections. The schematics of both above-mentioned profile orders are shown in Figure 3.17.

The total angle variation during k-space filling allows us to describe a circle during the acquisition of time T_{acq} and it can be represented as a function of time t:

$$\Phi = \frac{2\pi \cdot t}{T_{acq}}$$

Then, the gradient wave form shape in time can be described as follows:

$$G_x(t)\ sin(\frac{2\pi \cdot t}{T_{acq}})$$
$$G_y(t)\ sin(\frac{2\pi \cdot t}{T_{acq}}).$$

The gradient waveforms required to fill in one k-space are presented in Figure 3.18. The gradient waveforms are shown for the two different projection order as described previously (Figure 3.17).

3.4.2 Sequence optimization

Experiments were performed to validate the radial sequence as our technique of choice in proton lung MRI. The advantages and disadvantages of using the radial technique

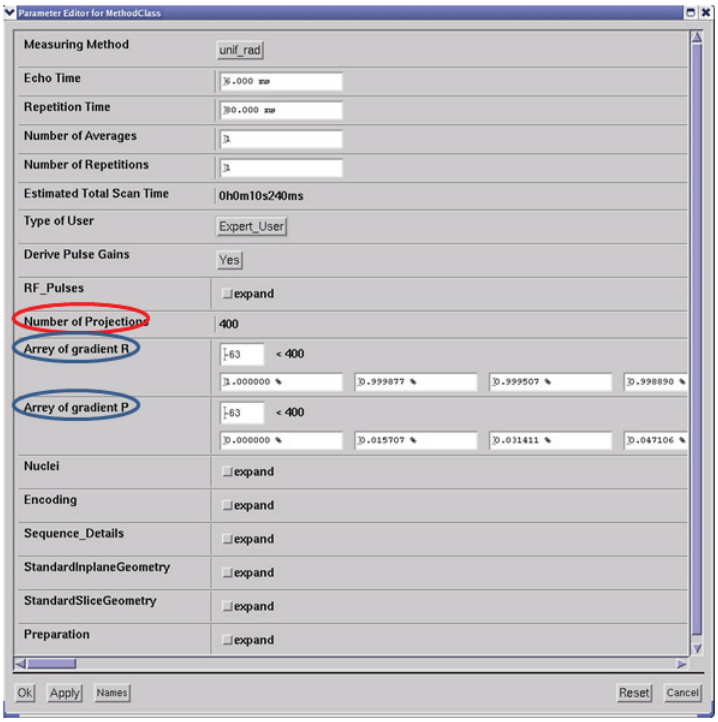

Figure 3.16: Interface of the UTE sequence. Radial specific sequence parameters: number of projections and gradients array in read and phase direction are indicated in the Figure.

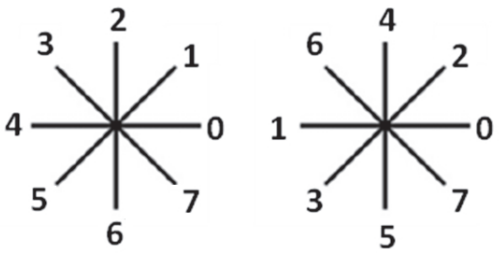

Figure 3.17: Profile order in case of uniform azimuthal projections distribution with an increment angle of a) $\Phi = 2\pi/N_s$ and b) increment preceded the projection reflection by π.

are illustrated below. All data presented here were obtained with a radial technique developed using ParaVision 4.0 in Lyon, France.

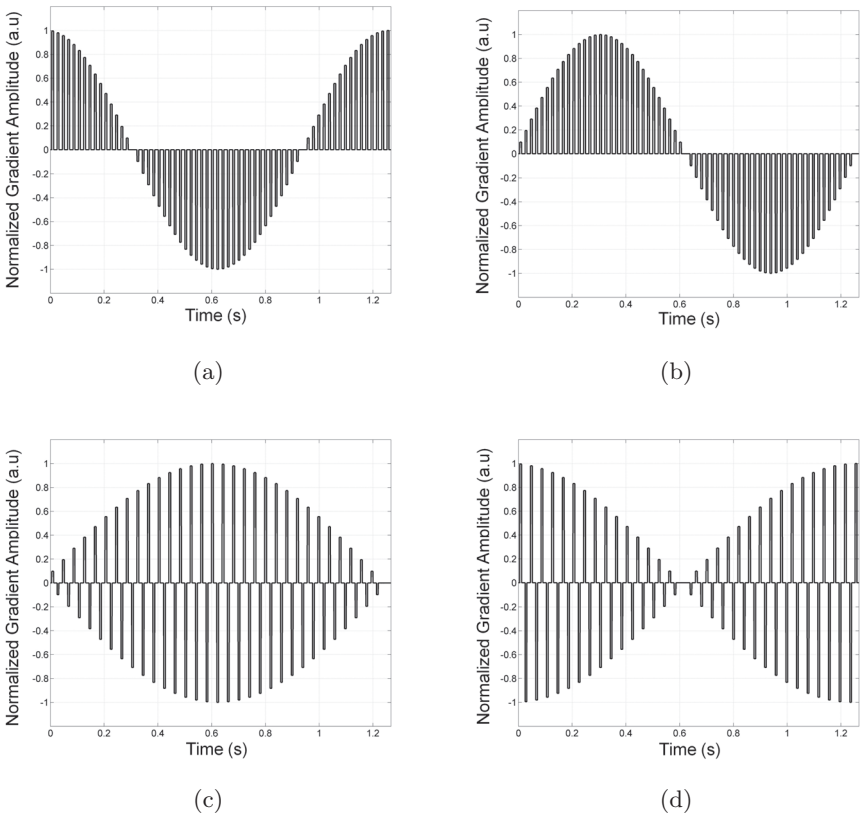

Figure 3.18: Gradient waveforms (G_x, G_y) in the case of two different profile orders. The curves represent gradient amplitudes in the case of the sequentially projection order (a,b) and the $\pi-$reflected projection order (c,d). For clarity, only 64 projections were used to fill in the k-space, TR of sequence was eqaul to 20 ms.

3.4.2.1 Gradients

The key parameters which must be considered during a sequence implementation are the two characteristic gradients' constants: the maximal gradient strength G_{max} [mT/m] and the maximal gradient slew rate (GSR) [mT/m/msec]. The maximal gradient slew rate defines the speed of gradients (rise time) employed to achieve their maximum gradient amplitude, which imposes a limit on the minimum achievable echo time, TE. The rise time depends on the pre-emphasis and for imaging scanners in Lyon and Biberach, it is equal to 230μs and 250μs, respectively. The longer the rise time, the longer the minimum TE. In order to achieve the shortest possible TE, the acquisition was performed during gradient ramping. The effect of non-uniform point sampling

during the ramp was corrected by gridding reconstruction (See section 3.3.4)

3.4.2.2 RF Selection pulse

To achieve a short echo time with conventional pulse selection, there must be a trade-off between the pulse duration and minimum slice thickness, due to the limited gradient amplitudes.

One can avoid the need for the time consuming selective excitation and large gradients required for thin-slice selection by omitting a refocusing gradient and using a half-pulse excitation, instead (see section 3.4.1).

The second approach which permits us to achieve the relatively short TE without the need to use the large gradient strength for a given slice thickness, is to apply a pulse with a high bandwidth.

To compare the effectiveness of slice-selection, acquisitions were performed using a standard selective Gaussian-shape pulse and also a non-selective, hard pulse. The phantom (containing NiSO4 (H2O6) (1.25g/L) and NaCl (5g/L) dissolved in 1000g of H2O) was placed in the magnet in an oblique position, with respect to the slice selection gradient as shown in Figure 3.19, and coronal slices were acquired.

As seen from Figure 3.19, the hard pulse gives crisper images as compared to the Gaussian pulse. However, due to the external lobes of the Fourier Transform of this pulse, it cannot be utilized for quantitative studies.

For further studies the conventional Gaussian-shape RF pulse was used, as it provides a reliable mean when image quantification is required.

3.4.2.3 Contrast

There are many natural sources of MR image contrast, including spin density (the local concentration of protons nuclei) or spin relaxation times (T1, T2, T2*). The typical lung MR images are proton density-weighted. However, it is also possible to obtain strong T2* or T1 contrast by enhancement or reduction of one of the relaxation pathways. This can be achieved by applying appropriate sequence parameters; for example by increasing the TE value, one can obtain T2* weighted images. The significant reduction of TR results in the T1 image's enhancement. Here, we will focus on T1-enhanced radial imaging.

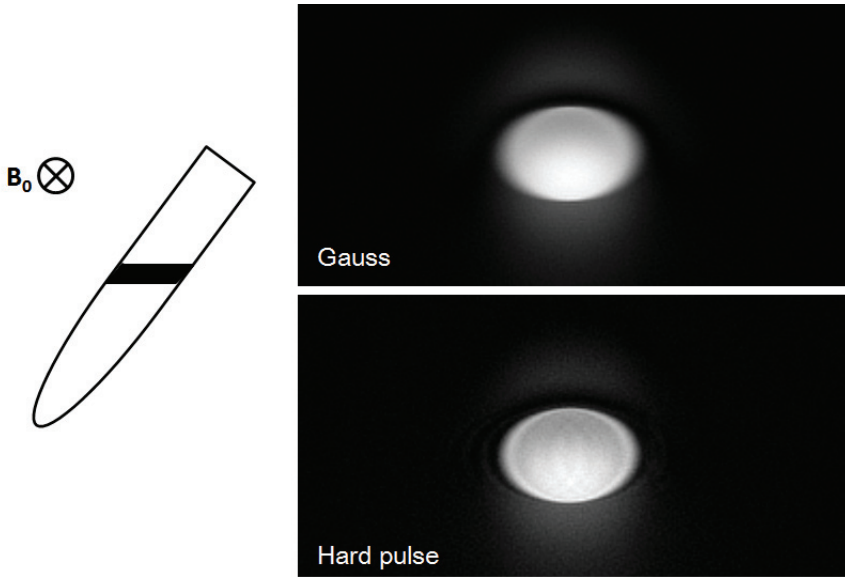

Figure 3.19: Coronal images of syringe obtained with Gaussian and hard pulse. The images were acquired using the radial sequence using the same imaging parameters. Slice thickness was set up to 2 mm. In case of conventional excitations 4 signal averages were applied.

In a radial acquisition after a given number of consecutive RF excitations, a steady-state of the longitudinal magnetization is reached. Under this condition, the signal for the transverse magnetization can be described similarly to that achieved with a spoiled gradient-echo acquisition given by:

$$S(\alpha) = \frac{S_0 \cdot sin\alpha(1 - exp - (TR/T_1))}{1 - cos\alpha(exp(-TR/T_1))}$$

where S_0 is an equilibrium signal. The flip angle which allows us to maximize the signal is called the Ernst angle. The value of the Ernst angle can be calculated by derivating previous equation, yielding:

$$\alpha_{Ernst} = arccos\left(exp\left(\frac{-TR}{T_1}\right)\right)$$

Furthermore, by changing the flip angle, α or TR of a sequence one can determine the T1 value of the lung parenchyma. The T1 value of the lung depends on the concentration of alveolar and dissolved molecular oxygen in lung tissue and blood. The knowledge of the precise value of T1 parameter is crucial in the oxygen-enhanced

MRI technique in order to assess ventilation defects in patients with many pulmonary diseases like embolism, fibrosis or pneumonia.

Figure 3.20 illustrates a series of axial images from a mouse thorax acquired with different value of TR ranging between 20 ms and 500 ms. By measuring the signal intensity changes with increasing TR value, one can determine the T1 for the lung parenchyma.

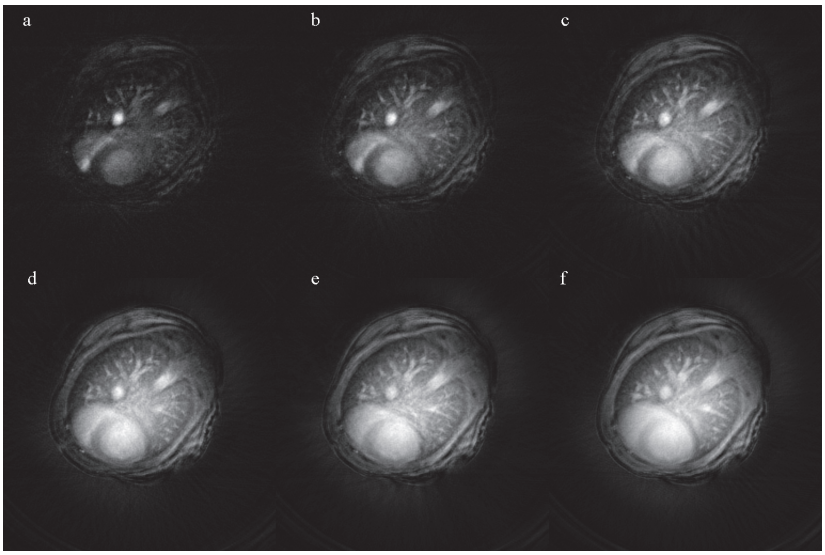

Figure 3.20: Images of a mouse thorax acquired with TR of 20 ms a), 50 ms b), 100 ms c), and 200 ms d). Signal from 20 excitations was averaged.

Figure 3.21 shows the signal from the regions of interest (ROI) from the lungs as a function of TR ranging between 20 ms and 500 ms. The ROIs were chosen to avoid large vessels. The data points were fitted to the aforementioned equation describing S(α) using a nonlinear algorithm with adjustable parameters S_0, α and T1. The T1 value obtained from this exemplary fit was $698 \pm 5 \cdot 10^{-6}$ ms (where fitting error was $(CHISQ/(N * M))^{1/2}$, where N is the number of TR points, and M is the number of fitting coefficients). The knowledge of T1 value allows calculation of the Ernst angle for any TR. For example, the Ernst angle is approximately 25° for TR of 80 ms at T1 equal to 700 ms.

Notably, the T1 value obtained from our experiment is shorter than the value reported in the literature for rodents, ranging between 780 at 2T (107) and 1300 at

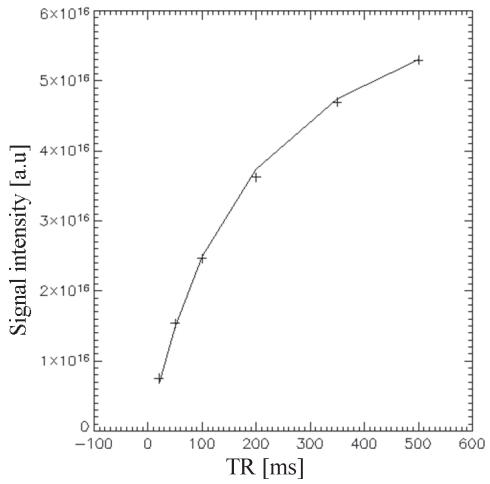

Figure 3.21: Signal intensity from the lung parenchyma versus repetition time.

7T (125). The reason for this discrepancy may result from inaccurate flip angle estimation, hovewer further investigations are needed in order to explain this observation.

3.4.2.4 Spoiling

As described is section 3.4.2.3, one of a possible way to obtain the T1-enhanced image of the lung tissue is to apply a short TE and short TR simultaneously. When a very short TR is used various unwanted spin coherences can appear leading to complex signal intensity weighting (combination of T1 and T2 weighting) (27). In order to eliminate the transverse magnetization prior to the next excitation, the MR sequence employs signal spoiling. Spoiling can be accomplished in a variety of ways. The simplest is to choose a sequence TR that is at least four or five times the T2 relaxation time, so that the transverse magnetization decays to zero by the end of the pulse sequence. The use of such spoiling approach results in extended acquisition time, which is undesirable for many imaging applications.

Spoiling can also be achieved using magnetic field gradients, or by phase rotations of RF pulses, such that the unwanted contributions to the MR signal cancel out. In such approaches, usually the extended minimum TR values are achieved.

Recently, it was demonstrated that a radial gradient-echo acquisition can generate images with ideally spoiled signal intensity at a very short TR < 5 ms when a spoiling scheme with random RF phase and gradients moments is applied (70).

For our application, an intrinsic feature of a radial sampling approach is used in which every projection is applied with different gradient direction, thus limiting a signals summation probability for consecutive TRs. Furthermore, sequence spoiling is accomplished by a phase rotation of RF pulses.

4

Robust protocols for free-breathing MRI of the lungs: Validation of the self-gating method

4.1 Introduction

In this chapter, the self-gating technique as a method for artifact-free image synchronization will be presented. First, a detailed description of the method's theory and the self-gating reconstruction algorithm will be given. The method will be compared with two other approaches, namely standard cardio-respiratory gating (CRG) acquisition and signal averaging (SA) acquisition. The results obtained from phantom and in vivo studies will be presented. Finally, the potential and the limitations of the self-gating technique will be discussed.

4.1.1 Motivation

One fundamental limitation of spatial resolution for in vivo MR lung imaging is related to motion in the thoracic cavity. This problem is more evident in imaging of small animals as their respiratory and cardiac rates are up to an order of magnitude faster than in human subjects (see chapter 1). Constant motion can degrade image quality, typically with blurring, ghosting or radial-striking artifacts that make it difficult to

distinguish neighboring voxels.

Several methods have been proposed to overcome this limitation in small animal studies. One can use an MR-compatible ventilator (47) that controls the breathing cycle and triggers the MR scanner to acquire data only during a specified phase of the cycle, such as at end-expiration or at full inspired volume. Images are acquired over multiple breaths to attain sufficient SNR. For example 150 breaths were used to obtain 900 radial samples of Fourier space for one image (22).

Heart motion artifacts can be eliminated using an electro-cardiogram (ECG) which synchronizes image acquisition with the cardiac cycle (18). In the ECG technique, the R-wave (see section 3.2) is detected by the triggering system and a trigger delay is used to set the time point (after which the pulse sequence is performed). Any desired phase of the cardiac cycle can be imaged by selecting an appropriate delay. Consequently, images free of motion artifacts, corresponding to different phases of the cardiac cycle, can be acquired.

Although a method with synchronous ventilation and cardiac gating allows one to obtain high resolution images (39), (54), the acquisition time is long and imaging protocol is complex. Additionally, since the acquisition is triggered by the R-wave, which can vary in time due to irregularities of the cardiac cycle, the use of a predetermined and constant sequence repetition time with those techniques is not possible. As a result, the image contrast is variable in time. This can lead to difficulties in the interpretation of image readouts when quantification of changes in signal amplitude or in tissue relaxation time is required.

Alternatively, motion artifacts in the lungs can be efficiently reduced using signal averaging (9). In this approach, the animals are allowed to breathe spontaneously and images are acquired without the use of either cardiac or respiratory triggering. Typically, 40 signal averages are sufficient to suppress most of the potential motion artifacts (9).

Another technique for motion artifact suppression is the use of a radial encoding method (42). The radial sequence was shown to have several advantages over Cartesian sampling techniques. The use of radial sampling leads to: (i) oversampling of low spatial frequencies, leading to intrinsic averaging of the subject contour, and (ii) the generation of artifacts as streaks which emanate from the object instead of being arrayed along a phase-encoding direction in Cartesian encoding (42). Another interesting feature of

radial imaging is the repetitive sampling of the k-space center giving access to total NMR signal amplitude after each RF excitation. This can serve as a motion navigator, which consists in repeatedly measuring a partial set of k-space data that is processed to track the motion.

This motion navigating property of radial sequence can be used to retrospectively monitor physiological functions such as cardiac or respiratory cycles. It has been applied recently in order to acquire time-resolved 3He ventilation images in spontaneously breathing animals (115). Similarly, in proton MRI this approach has been used to reconstruct time-resolved cardiac images synchronized with the cardiac cycle in humans (66), (67) and mice (48),(49). In both cases, the technique relies on the retrospective use of the MR signal intensity variations induced by cardiac and respiratory events. Regarding proton MRI, the synchronization of the cardiac cycle was possible due to large variations in blood volume, occurring in slices crossing myocardium cavities between systolic and diastolic phases. These large variations in blood volume resulted in large variations of signal intensity allowing for its synchronization (48).

4.2 Proposed solution

We used the specific navigating property of radial acquisition to retrospectively monitor the signal changes in the lung parenchyma. The signal intensity changes were possible to detect due to a very short echo time of imaging sequence. These signal changes were caused by lung volume and density changes due to respiratory cycles and the pulsation of pulmonary blood. Based on these observations we reconstructed artifact-free images using the self-gating reconstruction method.

The self-gating method allows one to:

- Obtain sharp images of the thorax that are synchronized to different phases of the cardio-respiratory cycle within one acquisition.
- Avoid delays associated with the setup of electrocardiographic (ECG) equipment, thus reducing overall imaging time and cost of studies.
- Ensure constant repetition times of the imaging sequence. This is necessary when quantitative image analysis is required.

4.3 Aims of this study

The main aims of this study include:

- Deriving NMR signals from the lung parenchyma and using then as a motion navigator;
- Implementing the self-gating reconstruction method to synchronize images with a specific phase of the cardio-respiratory cycle;
- Validating the navigator properties in the phantom stimulating motion;
- Applying and evaluating the self-gating method as a protocol for in vivo high resolution lung imaging in mice.

4.4 Method principle

4.4.1 Detection of double cardiac and respiratory motion by MRI

Cardio-respiratory gating relies on real-time monitoring of the cardio-respiratory cycle. The NMR signal intensity changes due to breathing and cardiac motion are monitored using a repeatedly acquired MR signal at the origin of k-space. For this purpose, repeated sweeps of a radial sequence are applied and a k-space center after each radial projection is sampled (see Figure 4.1). An MR signal amplitude measured at the center of k-space corresponds to the total transverse magnetization from the whole imaged volume. If the image volume contains moving or changing structures, a series of consecutively acquired echoes exhibits peak changes corresponding to proportional changes in the overall transverse magnetization due to motion (67). Using a radial acquisition, these signal changes can be detected at each radial view that samples the k-space origin with sampling frequency limited by the minimum sequence repetition time.

Figure 4.2 shows the signal amplitude changes versus time at the center of k-space for a set of consecutive radial views acquired in a spontaneously breathing mouse. In this example the sampling rate was 12.5 Hz and the display covers 16 seconds of acquisition.

Signal variation with two signal modulations can be observed: high frequency variations (4 Hz) due to the cardiac motion and low frequency variations (0.5 Hz) due to the

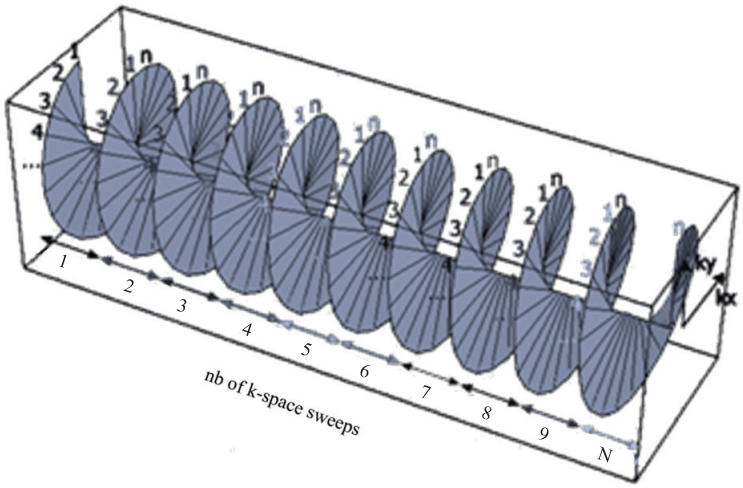

Figure 4.1: Scheme of data set acquisition. Signal at the center of k-space is sampled from repeated sweeps of the sequence.

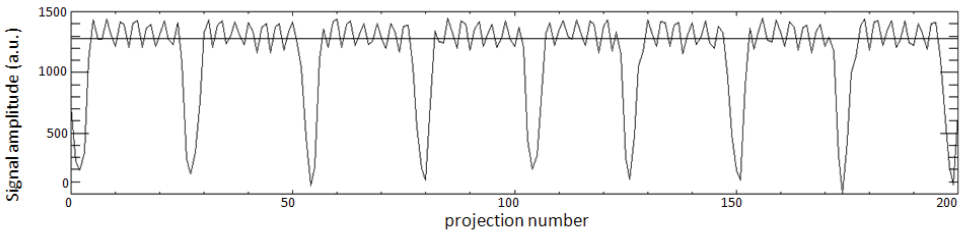

Figure 4.2: NMR signal amplitude from the center of k-space from a spontaneously breathing mouse acquired in coronal plane. Low frequency (0.5 Hz) and high frequency (4 Hz) signal modulations correspond to the respiratory and cardiac cycles, respectively. The line indicates the threshold (See section 4.4.2). The temporal resolution was 80 ms.

respiratory cycle. Using a Fourier filter, it is possible to separate these two signals. An example of the Fourier spectrum is shown in Figure 4.3. The spectrum shows several lines: two main lines correspond to the signal from breathing and pulsation of pulmonary blood in the lung parenchyma, while the remaining lines represent harmonics with different Fourier coefficients due to the non-sinusoidal shape of the signal.

Regarding the low frequency modulations due to the respiratory cycle (see Figure 4.2), the maxima and minima correspond to the end of expiration and inspiration, re-

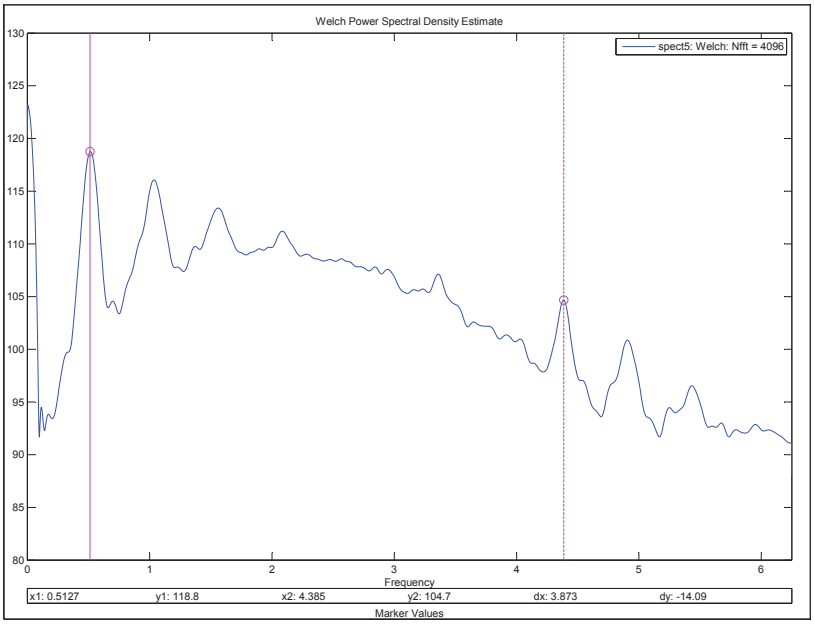

Figure 4.3: Fourier spectrum of the signal from Figure 4.2. The Hann filter was applied to the signal. Pointers indicate frequency corresponding to the respiratory (0.5 Hz) and cardiac cycle (4 Hz).

spectively. The inspiration phase is characterized by a reduced parenchyma density, hence the global decrease of MR signal. On the contrary, in the expiration phase the parenchyma density increases; this in turn increases the MR signal. Signals from other organs, such as the liver, during animal respiration may also contribute to the total signal amplitude. This results in greater changes in signal amplitude than expected from density changes only. Regarding the low frequency modulations due to the respiratory cycle (see Figure 4.2), the maxima and minima correspond to the end of expiration and inspiration, respectively. The inspiration phase is characterized by a reduced parenchyma density, hence the global decrease of MR signal. On the contrary, in the expiration phase the parenchyma density increases, increasing the MR signal. The signals from other organs such as liver during animal respiration may also contribute to the total signal amplitude. This results in larger changes in signal amplitude then expected from density changes only.

Depending on the slice orientation, different signal amplitude variations can be observed. Modulations caused by the animal's respiratory cycle are more pronounced

in coronal then in axial images. This is the result of larger lung volume changes in the superior-inferior direction as compared to the left-right and anterior-posterior orientation. Notably, the detection of signal variations due to the cardiac cycle is not restricted to slices encompassing parts of the cardiac muscle. Indeed, signal changes due to pulsing blood flow within pulmonary vasculature can be detected in all imaged slices. However, the maximum amplitude fluctuations due to pulmonary blood pulsation were observed in the slice containing a significant fraction of the heart muscle. An example of signal intensity changes in the axial plane is shown in Figure 4.4.

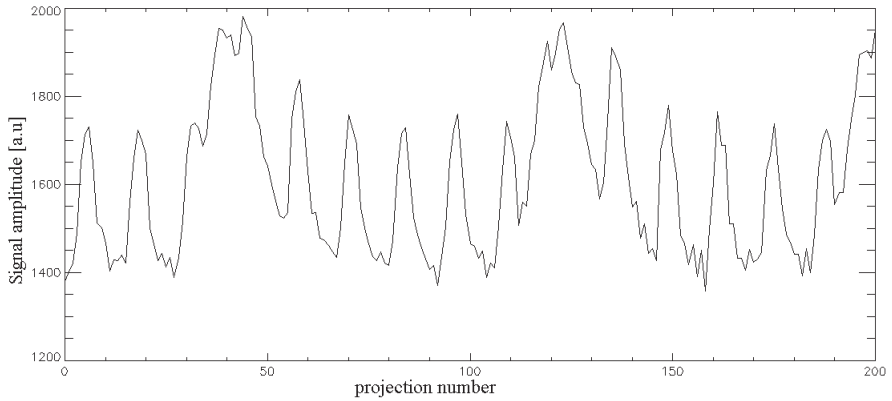

Figure 4.4: Signal intensity changes in the spontaneously breathing animal measured in the axial plane. Similarly, as compared to the signal from the coronal plane, two frequencies of signal modulation can be distinguished. The high fluctuation frequency (3.5 Hz) corresponds to cardiac activity. The temporal resolution was 20 ms.

4.4.2 Self-gating procedure

Retrospective self-gating reconstruction was based on the use of a signal extracted from the center of k-space as a trigger and its use for image reconstruction in spontaneously breathing mice.

The self-gated reconstruction was performed using in-house software written in IDL (RSI, Boulder, CO, USA), as follows:

- Self-gating signal extraction: As previously explained, the first sampled data points of each radial view recorded during the whole acquisition were extracted from the MR signal and plotted as a function of time. The plotted curve represents the respiration and cardiac pattern given by the view-to-view MR signal

amplitude variations. Typically, signals from 20 k-space sweeps were extracted and inspected.

- SG trigger detection: the view-to-view signal evolution was visually inspected, and depending on the required phase of the cardio-respiratory cycle, the user-defined threshold was chosen. Typically, a trigger level was set up at $\tilde{2}0\%$ of the tidal volume (coronal slices) or cardiac peak (axial slices).

- Self-gated reconstruction: The radial views selected in this way were used to fill in a k-space matrix. Figure 4.5 illustrates the principle of this procedure. A gridding algorithm (52) was used for the image reconstruction. Reconstructed images were interpolated into a 512×512 grid with a Kaiser-Bessel interpolation kernel (52).

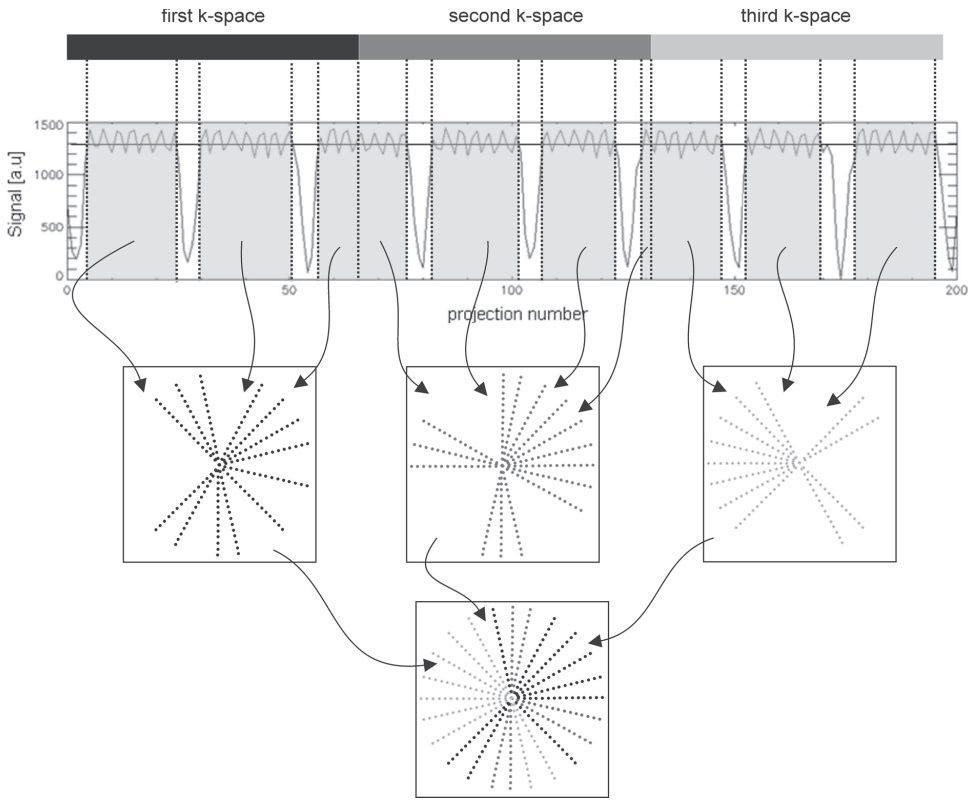

Figure 4.5: Schematic diagram of the retrospective self-getting reconstruction technique. The threshold selecting the radial projections for image triggering is indicated by a horizontal line.

4.5 Materials and Methods

4.6 Animal preparation

Female C57BL/6 mice (with an average weight of 25 g) were anesthetized with isofluorane (concentration 1.5%, flow rate 0.4 l/min) administered via a face mask. For cardiac monitoring, ECG electrodes were placed on the paws of the mice. The breathing cycle was controlled by a pressure sensor placed in the abdominal area. The animals were positioned supine in a custom-built Alderman-Grant coil and body temperature was maintained by a regulated water-flow. The experimental protocol was approved by the local ethics committee.

4.7 MR acquisition

Experiments were performed on a 4.7 Tesla Oxford magnet (10-cm wide bore) interfaced to a Bruker MR console. A radial sequence was used for image acquisition. Four hundred radial views per image with 128 points per view were collected with an angular sampling range of (0,2π) and increment angle of (number of view)/2π in order to fulfill the Nyquist criterion (400$\approx$128π) and minimize aliasing image artifacts. The radial projections were evenly spaced in k-space with a successive azimuthal increment of 180 degrees. Free induction decay (FID) acquisition was triggered during read gradient ramping, starting immediately after slice excitation and slice refocusing gradient. For each radial view, the k-space origin was acquired with an effective echo time TE of 450 μs (the effective TE is defined as the interval between the middle of the RF pulse and the first point of the acquisition). An RF excitation pulse of 0.2 ms was applied to excite a slice of 1.2 mm thickness.

Data acquisition was carried out using two different approaches: 1) "constant repetition time" imaging, and 2) cardio-respiratory-gated (CRG) acquisition. The "constant repetition time" protocol was based either on retrospective self-gating (RSG) or on a signal averaging (SA) approach.

For the RSG and SA acquisition schemes, the repetition time, TR, and flip angle were set to 80 ms and 30 deg, respectively. In the case of RSG acquisition, twenty k-space sweeps were performed resulting in a total acquisition time of 10 minutes. The

SA acquisition consisted in averaging data from 20 consecutive scans before image reconstruction (total acquisition time of 10 minutes).

The typical repetition time for CRG acquisition was equal to 400 ms resulting in a total acquisition time of 3 minutes. The flip angle was set to 20° .

For reproducibility tests, in vitro studies were performed. This includes the comparison of the signal averaged (SA), synchronized and respectively self-gated (RSG) images acquired in different experimental conditions determined by different rates and amplitudes of the phantom oscillation.

In order to validate the self-gating in vivo, specifically, signal averaging (SA) and standard cardio-respiratory gating (CRG) acquisition were used for comparison.

4.8 Quantitative analysis

To show the relative impact of the self-gating method on motion artifacts, the image quality was assessed using two image parameters, namely sharpness and noise level. The image sharpness was used to assess the image resolution while the noise level was measured to evaluate the impact of motion on image quality. Additionally, SNR per unit time was used as an image quality estimator.

1. Sharpness estimation

Motion in the thoracic cavity can degrade image quality, obscuring important anatomic structures. If not corrected, the motion can produce image blurring, ghosting, intensity loss and mis-registration. A simple method for estimating the image quality corrected for motion artifacts is by investigating its sharpness at the boundary between different imaged structures. The image sharpness can be represented by the profile-line steepness crossing the object of interest. Figure 4.6 presents three objects edges that are progressively less sharp. The line crossing the object corresponds to the profile through the object. One can notice a dependence: the less sharp the image border the more inclined the profile-line measured at this border.

The sharpness value can be assessed as follows: the local maximum and minimum intensity values are determined along an intensity profile and the distance d between the points having 80% and 20% of profile intensity is measured. The sharpness value

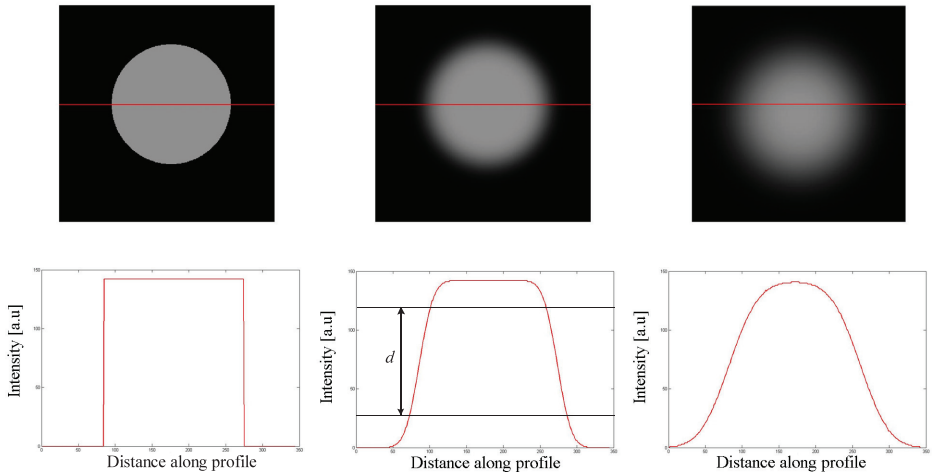

Figure 4.6: Concept of image sharpness. d represents a distance between 20% and 80% of the profile line.

is defined as $1/d$, see Figure 4.6. A similar approach was applied to vessel sharpness scoring of coronary arteries and the septum from clinical MR images (108), (66).

In practice, to avoid misevaluation of sharpness due to noise appearance in the image, an averaging profiles algorithm was implemented.

In order to calculate an average profile along any curved structure border such as: the diaphragm or vessels, we assumed that any fragment of its shape can be approximated by a quadratic function:

$$y = a \cdot x^2 + b \cdot x + c$$

To calculate the profile at any point on this curve, the tangent line was calculated:

$$\frac{dy}{dx} = 2 \cdot a \cdot x + b.$$

The profile line is given by a line perpendicular to the tangent:

$$y_p = \frac{1}{a} \cdot x + b.$$

The lengths of the profiles were determined by defining the coordinates of the boundary points (x_a, y_a) and (x_b, y_b) of each profile, crossing the diaphragm at the point (x_1, y_1) as follows:

$$x_a = x_1 - dx$$
$$x_b = x_1 + dx$$

$$y_a = y_1 + dy$$
$$y_b = y_1 - dy.$$

This procedure is illustrated in Figure 4.7.

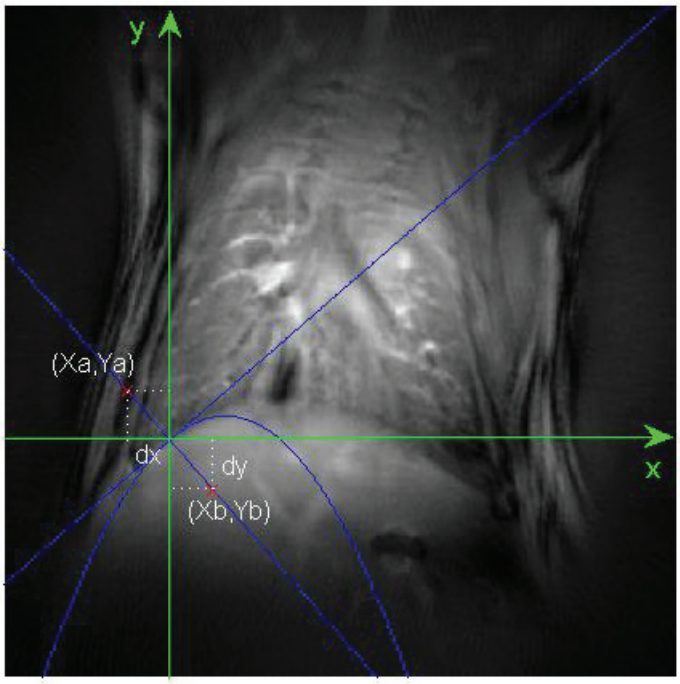

Figure 4.7: Graph showing the algorithm for calculating the line profiles. A position of the intensity profile generated and used for the calculation of the image sharpness at the diaphragm position, is shown. (x_a,y_a) and (x_b,y_b), are the coordinates of the profile's end-points. The length of the profile was 100 pixels.

The sharpness calculation algorithm was implemented under Matlab and the profiles were calculated with the following steps:

(i) a set of points lying on the boundary of lung structure (vessels, diaphragm,...) was selected; (ii) the selected points were fitted with a polynomial function (n=2);

(iii) the tangents to the polynomial curve and intensity profiles perpendicular to the tangents were plotted, as explained before. The procedure was repeated iteratively for each point of the curve and profiles obtained in this way were averaged. We found that typically, 30 to 40 profiles averaged along the considered structure were sufficient to correctly assess the border sharpness. Figure 4.8 shows an example of a profile crossing the diaphragm boundary obtained in the case of no averaging (Figure 4.8a) and with averaging (Figure 4.8b). The length of the profiles was modified depending on the considered structures and typically ranged from 18 to 35 pixels.

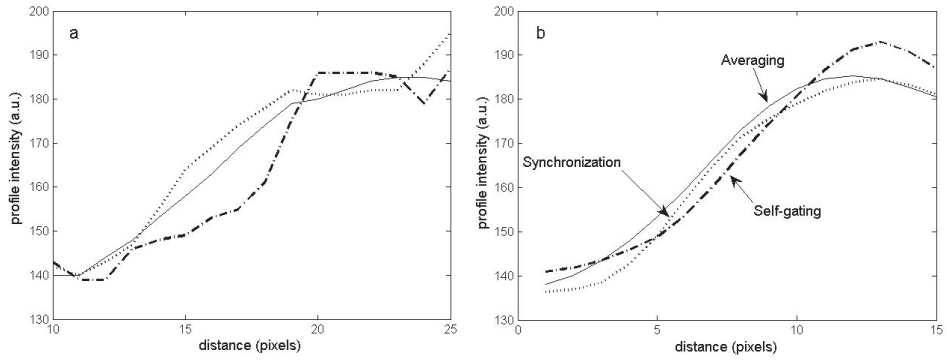

Figure 4.8: Typical profiles crossing the diaphragm boarder obtained in the case of no averaging (a) and with 15 averages (b).

In order to determine the sharpness value of averaged profiles several algorithms were tested:

- The extreme coordinates (Min, Max) of profiles were found manually and the aforementioned d value was determined according to:

$$d = a - b, where$$
$$a = Min + (Max - Min) \cdot 0.8$$
$$b = Min + (Max + Min) \cdot 0.2$$

- The modeled profile with variable steepness was generated and fitted to a measured profile curve using a minimization algorithm.

- Additionally, the profile was differentiated and its extrema were inspected (as shown below).

2. Noise level

Additionally, quantitative image quality assessments were performed using the noise level and signal to noise ratio (SNR) per unit of acquisition time. The noise level was defined as the standard deviation of mean signal intensity measured in a region of interest (ROI) located in the image background. To make the comparison of this parameter with different imaging techniques possible, the noise level was normalized according to the square root of acquisition time of the imaging sequence. The SNR per unit time was defined as an index of imaging method efficiency.

4.9 Results: Phantom study

In order to validate the proposed self-gating technique, phantom experiments were performed, simulating respiratory motion. The phantom consisted of a 2-cm plastic syringe filled with a water solution doped with Gd-DTPA to reduce the T1 relaxation times. The setup was designed to perform symmetric oscillations along the longitudinal axis of the syringe with different periods and amplitudes.

Figure 4.9 shows the signal changes over time measured at the k-space center from an oscillating phantom. In order to demonstrate the navigating properties of the self-gating technique, images synchronized to extreme positions of the oscillating phantom were reconstructed. Figure 4.10 compares non-synchronized (left), and synchronized phantom images synchronized to the maximum (middle) and mimimum (right) amplitude of oscillation. It can be seen that the synchronization permits to avoid the blurring artifacts due to motion (see Figure 4.10).

Figure 4.11 shows images of the oscillating phantom reconstructed from the averaged and gated-acquisitions (Figure 4.11a-f). The image triggering was performed at the maximal phantom displacement. The motion was followed using a pressure transducer sensor. For self-gating synchronization, the signal from the k-space center was used and specific amplitudes of phantom oscillation were chosen in the reconstruction process (see section 4).

Figure 4.12 compares the profiles measured at the boundary of the oscillating phantom for images acquired with oscillation rates of 30 cycles/min and 60 cycles/min and amplitudes of 1.5 mm and 3 mm, respectively. For both cases, the averaging results in a gentler slope of the profile while the slopes of the two gating methods are comparable.

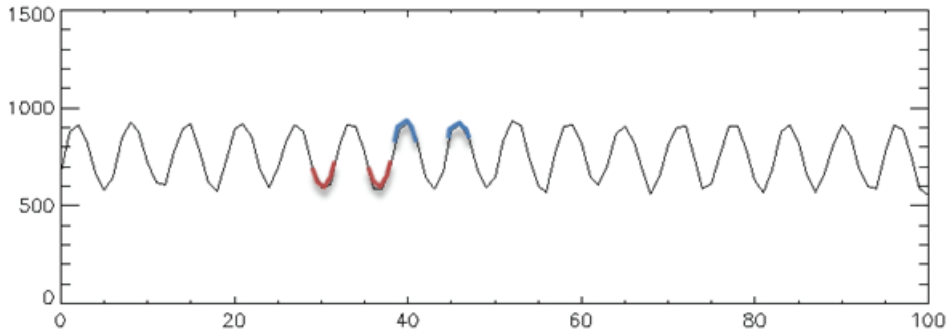

Figure 4.9: Signal intensity changes measured in the case of an oscillating phantom. The part of signal marked in blue corresponds to the maximum amplitude of oscillation while the part marked in red corresponds to the minimum amplitude of the oscillating phantom.

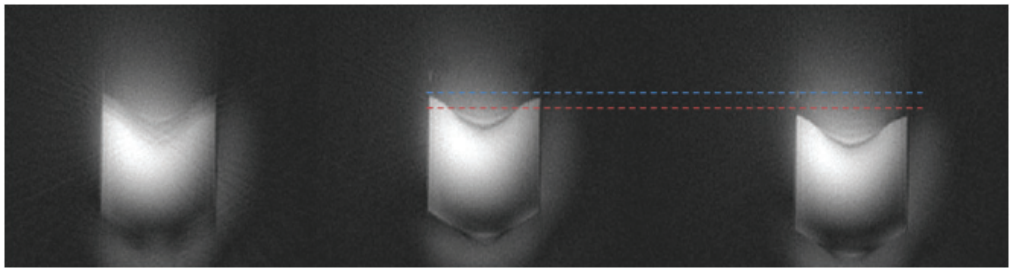

Figure 4.10: From left to right: a non-gated (left), synchronized to the maximum (middle) and minimum amplitude (right) image of oscillating phantom. Lines indicates different position of phantom reconstructed from corresponding parts of the signal marked in blue and red in Figure 4.9. Note the presence of blurring and streaks artifacts in non-gated image.

The quantitative measurements of sharpness are presented in Table 4.1. Comparable sharpness values were obtained for standard synchronization and the self-gating technique. In contrast, the sharpness for the averaging approach was approximately two times lower with oscillations of 1.5 mm amplitude and four times lower with oscillations of 3 mm amplitude.

Figure 4.13 shows the derivative of the profiles from Figure 4.12. In the case of the synchronization and the self-gating method, the directional derivative exhibits one minimum, corresponding to the observed abrupt signal change at the tissue border. It can be noticed however, that the derivative of the SA profile shows two smaller peaks, corresponding to a gentler and more blurred profile slope. Particularly, these two peaks

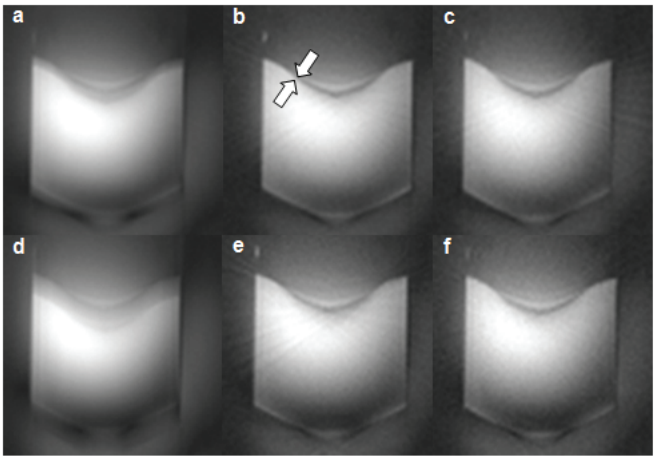

Figure 4.11: From left to right: averaged, synchronized and self-gating image of phantom oscillating with the rate of 30 cycles/min and the amplitude of 1.5 mm (a-c) and the rate of 60 cycles/min and the amplitude of 3 mm (d-f). Oscillations were performed along the longitudinal axis of the phantom. Arrays indicate the phantom's boundary in a position where sharpness was measured.

correspond to two different positions of the oscillating phantom.

Table 4.2 shows the noise level assessed for each of the acquisition methods.

It can be noted that the equivalent noise level was measured in the synchronized and self-gating images. Contrarily, the noise level observed in the signal averaging acquisition was twice as big as that of the gated acquisitions.

4.9.1 Results: In vivo

For all three protocols, the images were acquired consecutively in the axial and the coronal planes. Examples of coronal lung images obtained with RSG, SA and CRG approaches are shown in Figure 4.14.

From visual inspection, one can note similar features, comparable image quality and the absence of major motion artifacts related to respiratory or cardiac motion regardless of the imaging approach.

In order to estimate the degree of blurring suppression for each method, intensity profiles crossing either the diaphragm-liver boundary or going through a right pulmonary vein were generated for the quantification and scoring of image sharpness. Typical averaged intensity profiles from coronal images are depicted in Figure 4.15.

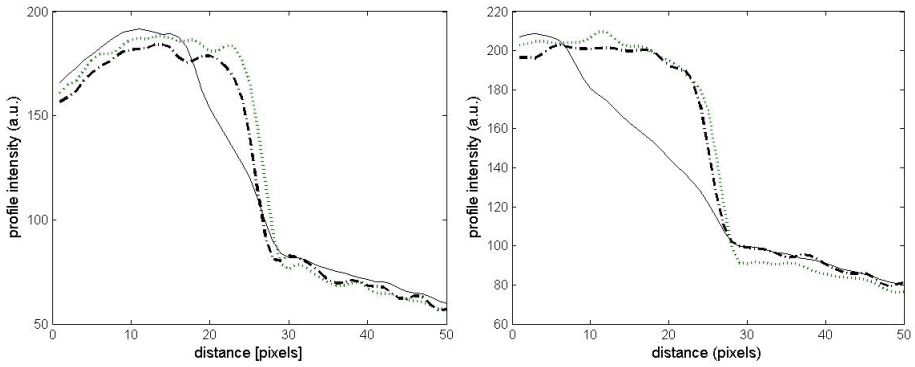

Figure 4.12: Averaged line profiles obtained in phantom oscillating with the rate of 30 cycles/min and amplitude of 1.5 mm (left) and the rate of 60 cycles/min and the amplitude of 3 mm (right).

Sharpness	Averaged image	Synchronized image	SG image
phantom case 1 [pixels-1]	0.111± 0.003	0.23± 0.02	0.23± 0.03
phantom case 2 [pixels-1]	0.061± 0.004	0.25± 0.04	0.24± 0.02

Table 4.1: Sharpness scores from averaged, synchronized and self-gated images. Values were obtained for two different rates and amplitudes of oscillation: 30 cycles/min and 1.5 mm (case 1) and 60 cycles/min and 3 mm (case 2), respectively. Each sharpness value was measured 10 times and averaged. The measurement error represents the standard deviation of averaged values.

Comparable slopes of the intensity profiles were measured both at the diaphragm-liver interface and through a pulmonary vein. Table 4.3 summarizes the sharpness value measured for each acquisition approach in the region of the diaphragm. Comparable values were obtained for all approaches confirming the qualitative similarity of the images and the intensity profiles.

Table 4.4 summarizes the noise level assessed for each of the acquisition methods. In the case of the signal averaging approach, the noise level was scaled with the square root of the number of averages.

Equivalent noise levels were measured in self- and CR-gated images while the noise level observed in the signal averaging acquisition was twice as big as that of the gated acquisitions.

The impact of averaging on the suppression of motion artifacts and image quality

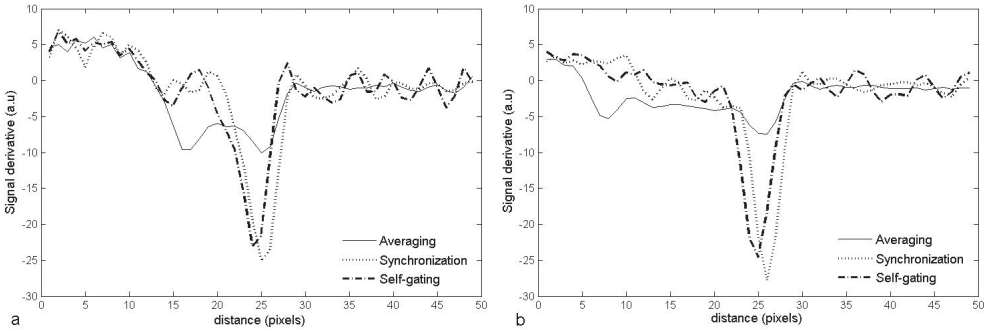

Figure 4.13: Derivative of the profiles from Figure 4.12

Normalized noise level in image background	Averaged image	Synchronized image	SG image
phantom (case 1)	3.33± 0.22	1.53± 0.05	1.59± 0.06
phantom (case 2)	3.54± 0.24	1.55± 0.08	1.71± 0.13

Table 4.2: Mean noise level values measured in the averaged, the synchronized and self-gated images of the oscillating phantom. Case 1 corresponds to the oscillation rate and amplitude of 30cycles/min and 1.5 mm, respectively while in case 2 the oscillation rate was 60cycles/min and the amplitude was equal to 3 mm.

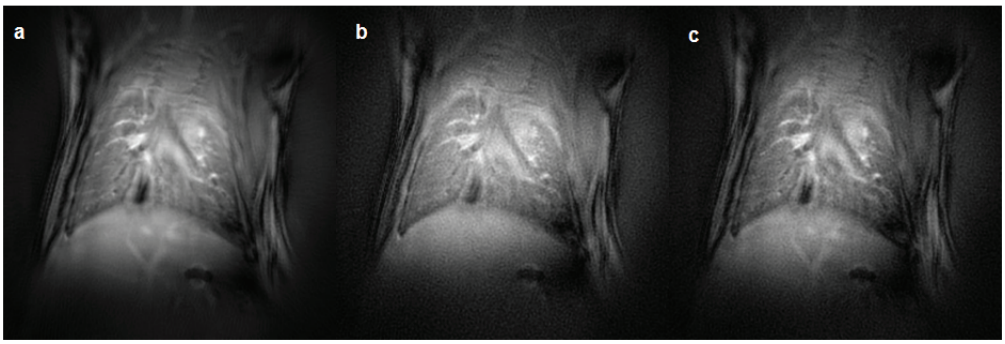

Figure 4.14: Typical images of mice thorax acquired using signal averaging approach (20 averages) (a), CRG approach (b) and retrospective self-gated procedure (c).

was investigated. Images acquired consecutively with the increasing number of averages were compared. Figure 4.16 shows coronal images acquired with 1, 5 and 20 averages. Typically, 20 averages were sufficient to suppress most of the streaking motion artifacts and the blurring located in the region of diaphragm and lung vasculature. The sharp-

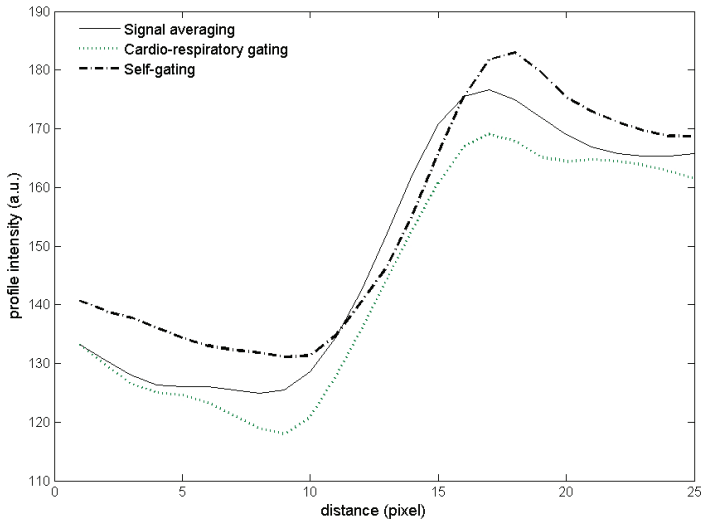

(a)

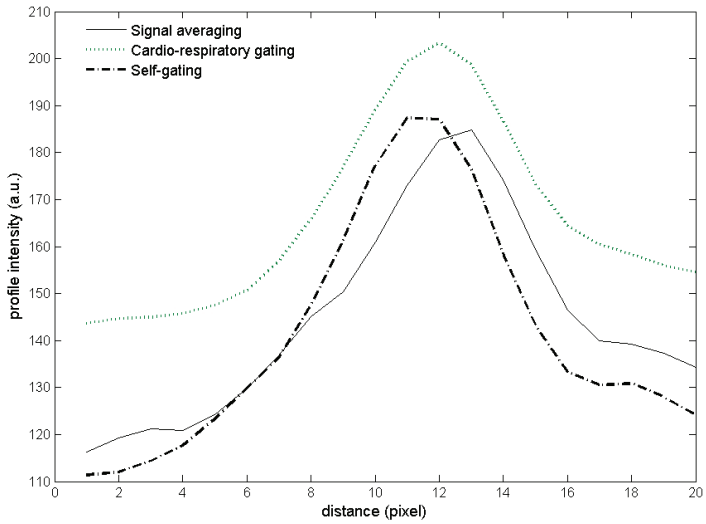

(b)

Figure 4.15: Averaged line profiles obtained at the diaphram/liver interface (a) and at the edge fo the right pulmonary vessels (b).

ness was assessed, as described earlier, for images acquired with 1, 5, and 20 averages. In order to evaluate the sharpness measurement accuracy, the standard deviations of measured mean distance d were estimated and compared. Calculated standard deviations, 12% in the case of 1 and 5 averages, and 4% for 20 averages, show that 20

	Averaged image	CR image	SG image
Sharpness in vivo [pixels-1]	0.15± 0.01	0.18± 0.04	0.16± 0.02

Table 4.3: Sharpness scores from averaged, cardio-respiratory-gated and self-gated images. Values were measured in coronal images from averaged intensity profiles crossing the diaphragm/liver boundary. The standard deviation values were obtained from repeated measurements.

	Averaged image	CR image	SG image
Normalized noise level in image background	8.64± 1.73	4.81± 0.26	3.851± 0.23

Table 4.4: Mean noise level values measured in averaged, synchronized and self-gated images in vivo. The standard deviation values were obtained from repeated measurements.

averages sufficiently improved the image quality

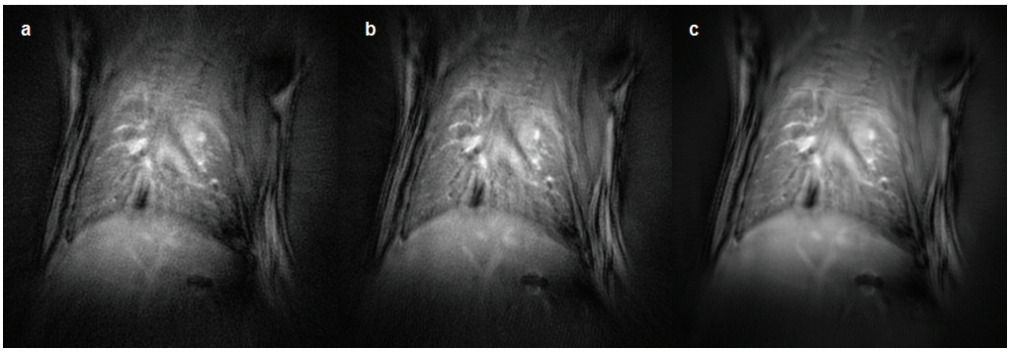

Figure 4.16: Reduction of motion artifacts by averaging. NA was 1 (a), 5 (b) and 20 (c). Arrows indicate some blurring artifacts due to respiratory motion.

We saw that the self-gating method can be efficiently used to minimize motion artifacts arising from respiratory and cardiac movement. However, the major advantage of the self-gating approach is its feasibility of forming lung images at various cardiac phases. The example of image synchronization using the self-gating technique to different phases of the cardiac cycle is shown in Figure 4.17. In this case, the radial projections corresponding to a specific phase of the cardiac cycle were chosen and image reconstructions corresponding to that specific phase were performed. As seen from Figure 4.17, the sufficiently high SNR of images enables one to detect the signal changes

between two phases of the cardiac cycle observed in the lung parenchyma. These signal changes correspond to the pulmonary blood perfusion variation during the cardiac cycle and they can be detected due to a large volume of blood in the lung parenchyma.

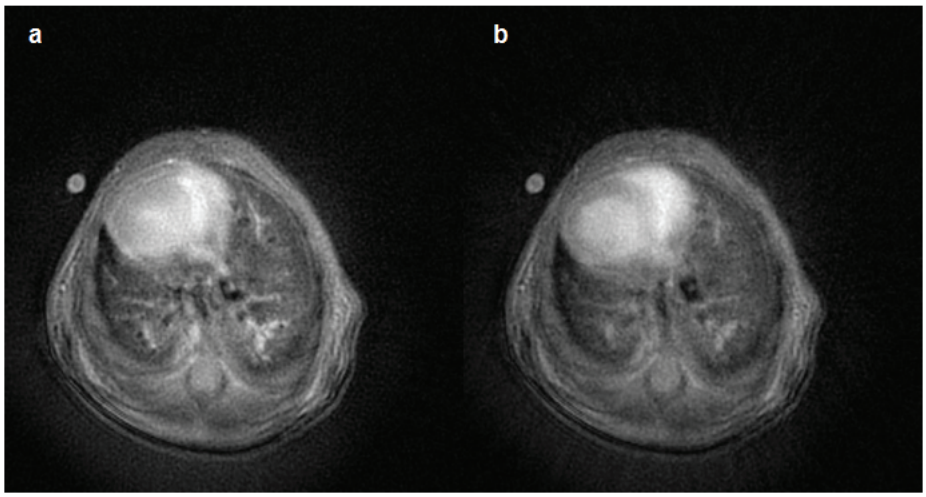

Figure 4.17: Comparison of self-gated transverse pulmonary images triggered in the systolic (a) and diastolic (b) phases of the cardiac cycle.

4.9.2 Discussion

The effectiveness of the signal averaging approach for motion artifact suppression in lung proton MRI images was previously demonstrated by Beckmann et al. in rats and mice using Cartesian k-space scanning (9). Since then, the signal averaging technique has been successfully applied to numerous animal models of lung disease for the detection and quantification of inflammation, mucous plugging or lung fibrosis (8), (56), (57). For all the above-mentioned applications, this approach has been recognized as robust, easy to implement and well-adapted to scanning large cohorts of animals.

The short-echo time radial k-space sampling is the acquisition technique of choice when increased SNR from lung parenchyma and improved image resolution are sought. Combined with cardio-respiratory triggering and a ventilation-synchronous scan, the approach has been shown to be very efficient for depicting the fine anatomical details of a rodent's lungs (54), (39), (63). The main objective of this study was to determine whether short-echo time non-triggered approaches can provide similar results, and thus two parameters were measured: the sharpness and the noise level of the image. The

image sharpness was used to assess the image resolution, while the noise level was measured for evaluating the impact of motion artifacts on the image quality.

The retrospectively cardio-respiratory gated approaches using Cartesian and radial sampled signals have been previously reported in proton imaging for time-resolved imaging in humans (67), (86) and small animals (48). The findings of the present study indicate that the self-gating approach is also applicable for lung imaging in small animals. Modulations of MR signal intensity induced by breathing and cardiac pulsations were noticeable in both coronal and axial imaging slices. Modulations caused by the animal's respiratory cycle were more pronounced in coronal then in axial images. This results from larger lung volume changes in the cranio-caudal direction as compared to the left-right and anterio-posterior orientation. Notably, the detection of signal variations due to the cardiac cycle was not restricted to slices encompassing parts of the cardiac muscle. Indeed, signal changes due to pulsing blood flow within pulmonary vasculature were detected in all imaged slices. These signal changes were used for reconstructing images synchronized with the cardiac cycle.

The results from sharpness measurements indicate that spatial resolutions equivalent to those of CRG acquisitions can be obtained using self-gated or averaging approaches. In the case of averaging acquisition, this counterintuitive observation can be attributed to the peculiar behavior of radial acquisition in the presence of a moving structure. In radial images, motion artifacts are usually distributed as radial streaks in the periphery of the image. Furthermore, the acquisition of FID signals at a very short echo time prevents the phase accumulation of moving spins in the presence of the imaging gradients.

Similar diaphragm positions for all three imaging techniques were observed in coronal images (Figure 4.14). Cardio-respiratory and self-gated lung images were acquired at the expiratory phase with the animal breathing spontaneously at tidal volume. As seen from the MR signal intensity time curve in Figure 4.2, the fraction of time spent in the expiration phase represents about two thirds of the total breathing cycle of the animal. As a result, in the signal averaging image, the diaphragm is seen in a position corresponding to the expiratory phase.

The noise level was measured in the image periphery where the motion artifacts are presumably mainly located. A two-fold higher noise level was observed in the signal

averaging acquisition. This higher noise level is an indication of increased fluctuating signal intensity related to motion as can be suspected from non-gated acquisition. However, this increase in noise level did not affect the sharpness measurement within the lung nor did it degrade the overall image quality.

If image SNR is of concern, the SNR per unit time provided by the different approaches has to be considered. When using appropriate RF excitation at the Ernst angle, it can be demonstrated that signal averaging and CR-gated techniques can yield very similar SNR per unit time. On the contrary, the self-gated technique has a reduced SNR per unit time due to the discarding of the radial views during the image reconstruction.

Despite its degraded SNR per unit time, self-gated acquisition offers the possibility of reconstructing lung images at different cardiac or respiratory cycles. Figure 4.17 shows a typical axial image of a mouse thorax obtained using the retrospective-gated technique at two different cardiac cycle phases. In this case, the projections corresponding to systolic and diastolic phases of the cardiac cycle were chosen and the images corresponding to each phase were reconstructed. Depending on the cardiac phase, one can observe signal intensity variations in the parenchyma that are attributed to changes in lung perfusion. Furthermore, if needed, the acquired k-spaces can be averaged later to generate higher SNR images.

The results obtained in the phantom study validate the accuracy of the self-gating method for motion artifact suppression, the sharpness and noise level were found to be similar to those obtained with the standard gating technique. However, in contrast to in vivo experiments, degradation of the sharpness value was observed for signal averaging acquisition. Although the frequencies and amplitudes of phantom displacement correspond to the breathing rate and diaphragm displacement in mice and rats, the pattern of the phantom's motion was different to that observed in vivo (as mentioned above, the fraction of time spent in the expiration phase represents about two thirds of the total breathing cycle of the animal).

4.9.3 Limitations of the method

The limitations of our protocol are primarily related to the imaging sequence, one of which is related to the off-center displacement of the radial trajectory caused by the imperfections of the gradient system. As a result, the real radial trajectory misses

the k-space center which results in image artifacts. Consequently, the position of the first point of the radial views changes as a function of the projection angle. This signal misalignment can cause unwanted signal modulation with a period equal to the duration of a complete k-space scan (TR $\times$ nb radial projection) (48). Although in our experimental setup we did not observe the signal modulation which differs from that defined as the intensity of a cardio-respiratory signal changes. One has to ensure the correctness of the measured signal variation. Therefore, in the future, a specific method for the measurement and possible correction of this off-centering effect (93) should be applied to standardize the self-gating method.

The second limitation of this study is related to the temporal resolution due to a limited TR value. The TR chosen in this study was equal to 80 ms; this value allows high SNR images of the lung parenchyma to be obtained. The sampling frequency of the k-space center (determined by the TR value) allows us to obtain synchronized images for only two different phases of the cardiac cycle. Figure 4.18 shows images corresponding to the systolic and diastolic phases of the cardiac cycle acquired with different TR values. The decrease of the signal with decreasing TR value can be observed. To obtain sufficient temporal resolution, allowing better cardiac and respiratory synchronization to be achieved, one can reduce the TR value with simultaneous averaging of the gated-signal from several k-space to attain sufficient SNR.

Additionally, as mentioned previously, the signal amplitude varies according to the orientation of the chosen slice. Therefore for each image to be synchronized correctly, requires inspection by an individual.

4.9.4 Conclusions

In this chapter, based on the self-gating property of the radial UTE technique, we have shown that signals from the lung parenchyma can be derived and used for the free-artefacts image synchronization. To validate the self-gating method, different short echo-time radial imaging protocols were applied for proton lung imaging in small animals during spontaneous breathing. “Constant repetition time” methods and the cardio-respiratory gated approach were compared. Within the limit of the nominal image resolution of this study (pixel size of 54μm $\times$ 54μm), parenchyma and vascular structures in mouse lungs were visualized with equivalent spatial resolution for all the applied techniques. The use of non-cardio-respiratory-gated techniques offers several

advantages. First of all, it simplifies the imaging protocol for lung MRI of rodents. Second, the images are acquired with an operator-defined repetition time, allowing the control of the image contrast. Finally, the retrospectively-gated approach offers the possibility of lung imaging at multiple phases of the cardiac or respiratory cycles.

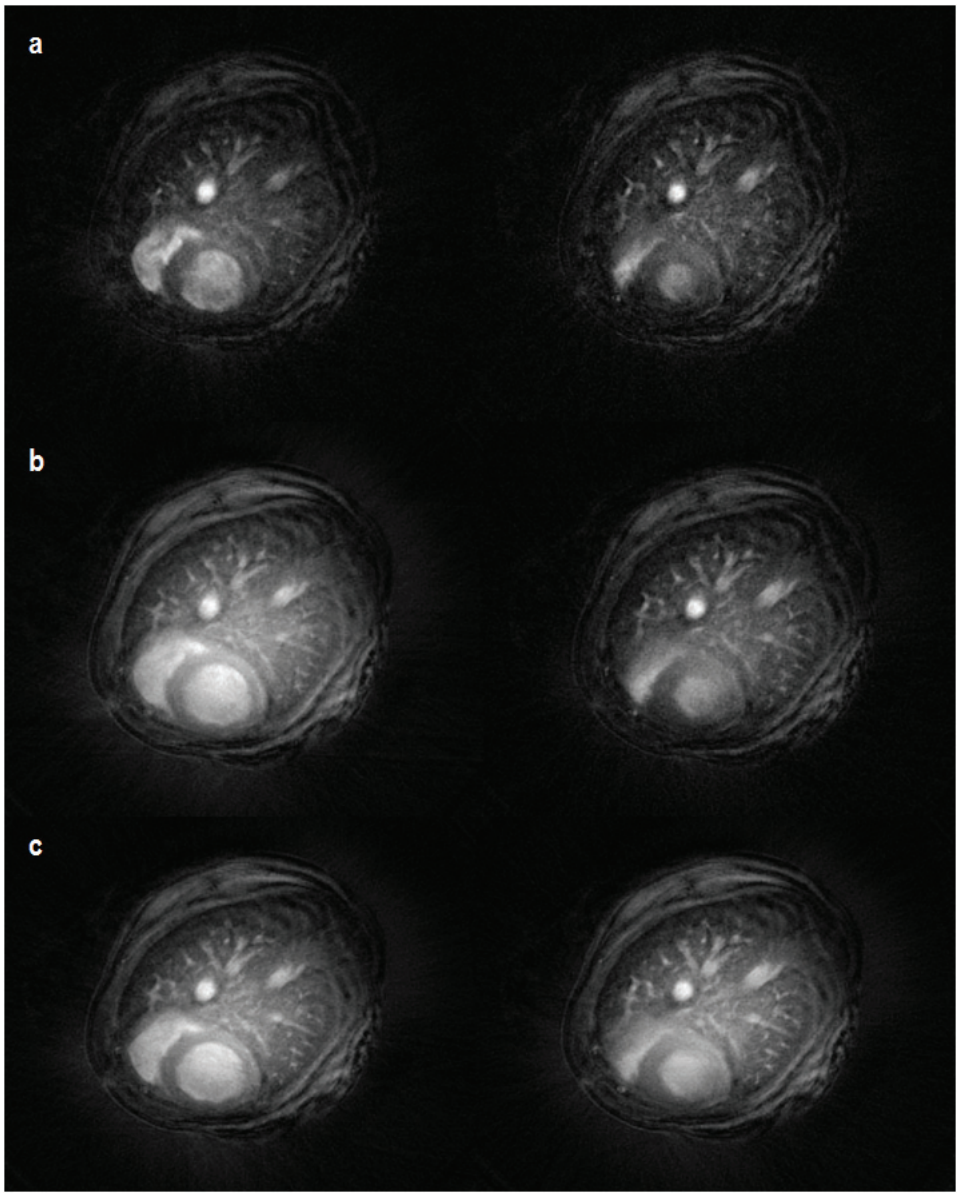

Figure 4.18: Images in the systolic and diastolic phase of cardiac cycle acquired with TR equal to 30 ms (top), 50 ms (middle) and 100 ms (bottom). Decrease of the signal intensity with decreasing TR value can be noticed

5

Detection of LPS-induced inflammation in rat lungs

5.1 Introduction

In this chapter, the focus will be on different MR approaches of detecting inflammation induced experimentally by Lypopolysaccharide (LPS) exposure in rat lungs, modeling Chronic Obstructive Pulmonary Disease (COPD). First, characteristic features of COPD will be presented. Next, the experimental design, the main results and conclusions will be provided. This study raises several interesting issues, including the validity of the UTE technique for quantifying the extent of inflammation, as well as exploration of the early stage inflammation investigation approach in animal models by means of macrophage imaging using MR.

5.2 Aims of the present study

The detection of the extent of inflammation plays an important role in establishing therapeutic responses and in the development of new treatment agents. Also, the earlier a disease can be detected and characterized, the greater the chance of being able to successfully combat the disease with an appropriate treatment. An early estimation of the extent of inflammation is therefore of crucial importance. To reach these two goals, two independent studies were designed based on the UTE imaging technique.

The main objectives of the first study (**study I**) were:

- To create a tool allowing for reproducible edema detection.
- To develop an MR protocol for lung inflammation assessment with respect to pharmacological research strategies.
- To verify if utilization of the UTE technique improves in vivo volumetric evaluation of lesion extent.
- To quantify the edema volume.
- To evaluate the validity of the UTE technique for the quantitative diagnosis of lung inflammation.

The main objectives of the second study (**study II**) were:

- To investigate the feasibility of the early detection of inflammation assessed by cellular infiltration of macrophages at the site of inflammation.
- To establish a method for estimation of the inflammation
- To correlate MRI findings with histology

5.3 Experimental animal model

Animal models play an important role in the understanding of the pathogenesis of chronic obstructive pulmonary disease (COPD). Different experimental COPD models have been developed in guinea pigs, rats and mice using cigarette smoke and endotoxin (81), (129), (69), (76) . For details concerning the experimental COPD models, the reader is referred to (106), (77), (21). Many of these models mimic emphysema - an advanced stage of COPD. Emphysema will be described in chapter 6. Here, the focus will be on early stages of COPD, with a particular consideration to the inflammation process.

The main feature of the inflammation characteristic for COPD is an increased production and secretion of respiratory mucus and influx of inflammatory cells. The inflammatory cells contain along neutrophiles and macrophages.

Airway infections similar, to those observed in human COPD patients can be induced by endotoxin-laden bacteria (124), (117). More specifically, the endotoxins are

lipopolysaccharide-protein molecules released from the walls of some gram-negative bacteria. Briefly, the bacterial cell surface consists of an inner cytoplasic membrane and a tri-layer outer cell wall structure; the outer-most layer consists of lypopolysaccharide, (LPS). The endotoxin refers to the impure extract of LPS combined with different proteins.

The LPS introduced to the living organism provokes a septic shock initialized by ligand-receptor interaction with a number of immune cells. This includes the mononuclear phagocytes (MPs) which comprise circulating monocytes and fixed tissue macrophages.

The macrophages are believed to play a pivotal role in the recognition and the transduction of LPS. They produce chemotactic mediators such as interleukin $1-\alpha$ and β (IL-1 α, β), tumor necrosis factor (TNF-α). TNF-α may account for neutrophil recruitments and activation(124), (131). More precisely, they increase the adherence of neutrophils on endothelial cells and migration of neutrophils into the pulmonary spaces (1). The cellular infiltration into the site of inflammation is considered to be a very early sign of inflammation.

In this study, two rat species, the Brown Norway (BN) and Wistar were exposed to LPS to induce the inflammation with features characteristic for COPD. The exposure to LPS provokes infiltration of the alveolar and bronchiolar air spaces (117) by neutrophils, as well as induction of mucous cell metaplasia (44). This process is presented schematically in Figure 5.1.

5.4 Lung inflammation detection: State-of-the-art

An accurate and sensitive method for inflammation detection and quantification is indispensable for the development of new therapeutic drugs and for the analysis of the pathogenesis of diseases.

Traditionally, bronchoalveolar lavage (BAL) is used to estimate lung inflammation in pharmacological research in small animals (91), (11). The BAL procedure involves washing the cells and secretions from the alveolar and bronchial airspaces by instilling saline solution via a fiberoptic bronchoscope and withdrawing the fluid immediately after. The fluid is analyzed and withdrawn cells counted. A major limitation of this

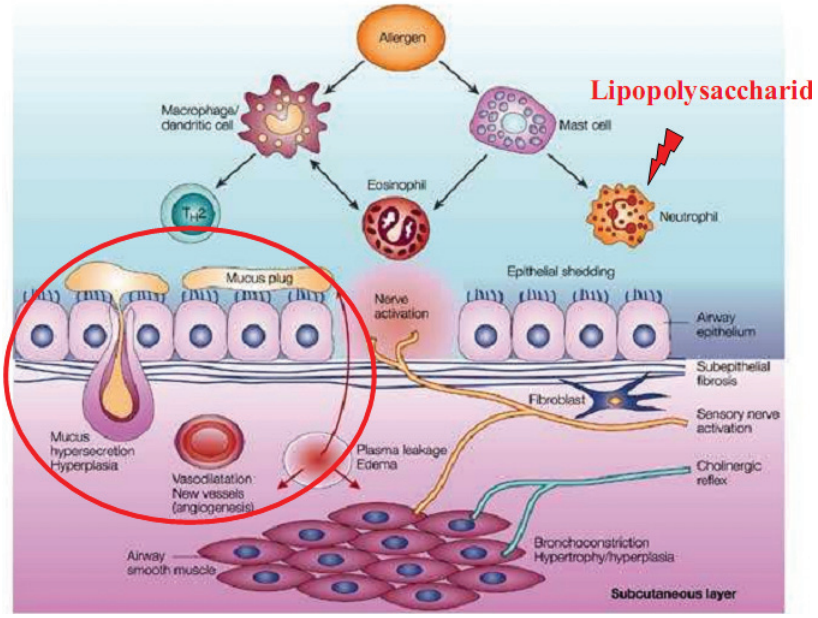

Figure 5.1: Schematic of LPS induced inflammation Reprinted from N. Beckmann, [Beckmann2001].

technique is the large variability in normal anatomy, which makes it difficult to differentiate among different diseases based on BAL only. Furthermore, the cell findings in BAL fluid are non-specific in terms of the precise location of the inflammation.

Recently, it was reported that detection of lung inflammation in the COPD was feasible using 18−fluoro-deoxyglucose and positron emission tomography (PET). The PET scan is a well-validated method for in vivo monitoring of the metabolic activity of cells in the brain and to detect tumors. Since inflammatory cells utilize glucose as a source of energy during their activation, it was suggested that 18FDG uptake by inflammatory cells in the lung could be used as an in vivo measurement of both total and regional lung inflammation (64).

It has also been demonstrated that magnetic resonance imaging constitutes a relevant tool in the research of lung diseases in animal model studies due to the high resolution obtained in MR images and easy protocol implementation.

The induced inflammation modifies the characteristics of pulmonary tissue resulting in an increase of SNR and T2* (29), (110) as compared to the healthy tissue, which can be detected by MRI.

For instance, Beckmann et al. have shown that standard proton MR imaging can be used as a diagnostic tool for detecting inflammation during the evaluation of various pulmonary diseases in animal models (11). The low SNR of lung parenchyma, coupled with the high SNR of edema (9), (12), allows a precise detection of the edema extent. Additionally, motion artifacts were suppressed by multiple averaging with a short acquisition of approximately 70 s for one slice.

Beckmann et al., used a standard gradient-echo technique to investigate MR signal development in the lungs of rats after intratracheal instillation of LPS (14). Following the LPS challenge, images exhibited two different types of overlapping features: a diffuse and bright component associated with edema formation and the second component with irregular appearance and weaker intensity. Histological analysis was correlated with MRI findings, suggesting that the second component of the detected signal was due to secreted mucus. Also, mucus concentration was the only parameter that significantly correlated in the BAL measurement. Furthermore, Quintana et al. investigated the inflammatory effects at early time points (3 and 6 hours) after endotoxin challenge (98). At these time points, irregular fluid from inflammatory regions was detectable and it was associated to edema. BAL fluid analysis showed an increase of inflammatory parameters including macrophages and neutrophiles (98).

More recently, Flogel et al., investigated the LPS-induced inflammation process by means of emulsified perfluorocarbons (PFC) (35). Intravenous application of PFC particles resulted in its accumulation in the inflammatory regions of the lungs and was detectable with 19F MRI. Furthermore, the regions where PFC infiltration was detected showed the presence of edema on proton MR images, at the later time points.

5.5 Proposed approaches

Study I

Conventional gradient-echo MR imaging has been recognized as an efficient tool in assessing the edema volume (11) . Furthermore, in this approach, motion artifacts can be reduced by averaging (9). Despite multiple averaging, Cartesian-based MRI in the lung remains sensitive to ghosting and motion blurring. This can lead to misevaluation of the inflammation extent. We proposed using the UTE technique to study the repro-

ducibility of edema detection, as this technique is robust against motion and provides improved image resolution compared to the standard gradient echo technique.

Study II

It has been reported that iron oxide nanoparticles (IONPs) can be used to detect the infiltration of macrophages to the sites of inflammation. For review refer to (10), (26), (104). These particles, injected intravenously, are not immediately removed from the blood circulation by the mononuclear phagocytic system but may be taken up by macrophages by means of endocytosis. The iron-loaded macrophages can later be tracked by MRI due to the signal modulation they produce in the inflammatory regions infiltrated by these cells. Therefore, the inflammation extent, defined as the area of cellular inflammatory infiltrates can be delineated.

Although this approach was used in pre-clinical animal models of various diseases, (13), (55), (94), (126) it was never applied to lung imaging. This is due to two particular challenges. The first is concerned with the fact that the iron particles largely affect T2* relaxation of protons - usually leading to attenuation of the MR signal (26). Since lung images (under traditional gradient echo imaging) appear black, applying the negative contrast agent will not provide additional information. The second, biological, challenge is related to the existence of different populations of macrophages (see - section 2.). The first difficulty is addressed by employing the UTE imaging sequence which allows the visualization of lung parenchyma, thus allowing detection of contrast changes due to the presence of iron particles. To address the second challenge, the specific conditions of contrast agent administration must be preserved to optimize opportunities available for macrophages labeling. Here we examined the feasibility of detecting the macrophage infiltration into the lungs following the LPS instillation.

5.6 Materials and methods

5.6.1 General study design

In this chapter, two independent study protocols (I, II) are presented. The global structure of this study is presented in Figure 5.2.

Study I focuses on the evaluation of the UTE technique for accurate measurement of the extent of edema in LPS exposed Wistar rats.

This study was performed in collaboration with Boehringer Pharma in Biberach, Germany. The experimental protocol of this study is shown in Figure 5.3.

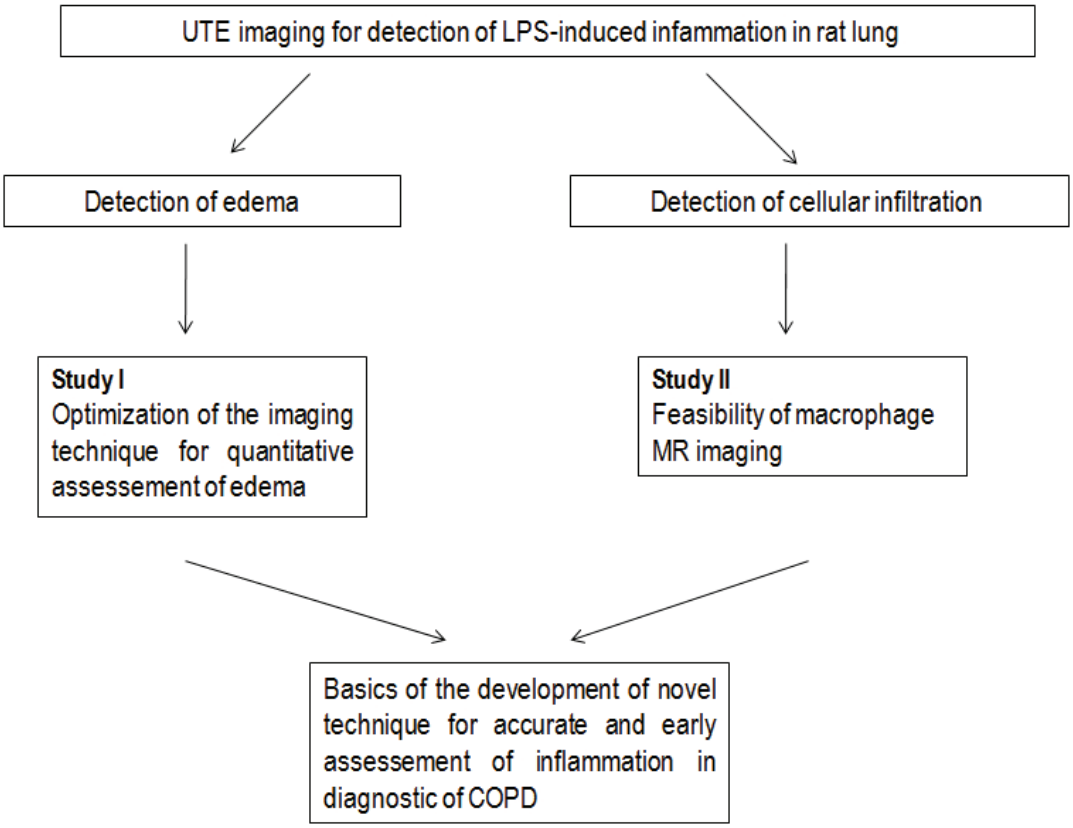

Figure 5.2: Study design.

Study II focuses on the detection of the early stages of inflammation (i.e. by detection of inflammatory cells infiltration) in Brown Norway rats), by means of macrophage MR imaging. This study was performed at the Creatis-LRMN lab in Lyon, France.

The schematic of the experimental protocol of this study is shown in Figure 5.4.

5.6.2 Animal preparation

Both studies were performed in accordance with Ethics Committee regulations. Study II was performed with the approval of the local Ethics Committee of the Rhone-Alpes region (license No. 302).

The experimental protocol was different for **studies I** and **II** with regards to species used throughout the study and administration of LPS. The experimental protocol of

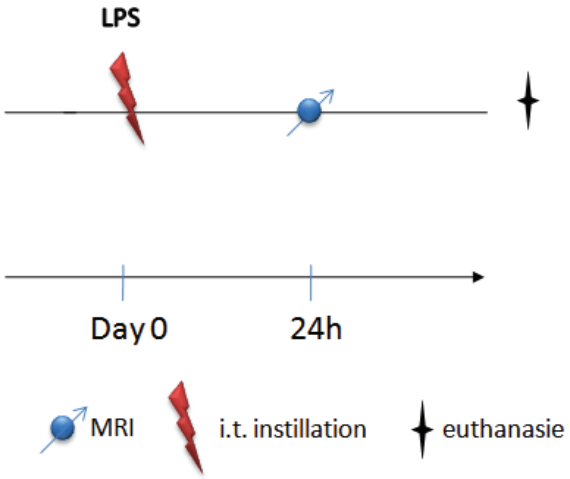

Figure 5.3: Protocol design for study I.

both studies is detailed in Table 5.1.

Briefly, in both studies, 1 mg/kg of LPS was dissolved in 0.2 mL of saline. The rats were anesthetized by intramuscular injection of a mixture of ketamine and xylazine. After the animals lost their toe pinch reflex, they were positioned supine on a board with their heads tilted up (see Figure 5.5).

In **study I**, LPS was selectively instilled into the left lung using a fiberoptic bronchoscope while the right lung serving as a control.

In **study II**, the intubation was performed with a 26-gauge flexible polyethylene catheter attached to the 1mL syringe and 0.2 mL of the solution was instilled into the trachea. In this way, it could later reach both, the left and right lung.

In order to have a homogeneous distribution of the product in the lungs, the animals were ventilated by means of a mechanical ventilator at a frequency of 60 breaths per minute for approximately 1 minute. After instillation the animals were allowed to recover maitaining their body temperature on a heating pad.

5.6.3 Contrast agents

There were no contrast agents used in **study I**. The imaging sequences parameters were chosen to ensure the T1 enhancement of detected fluids.

In study II, the ultrasmall superparamagnetic particles of iron oxide (USPIO),

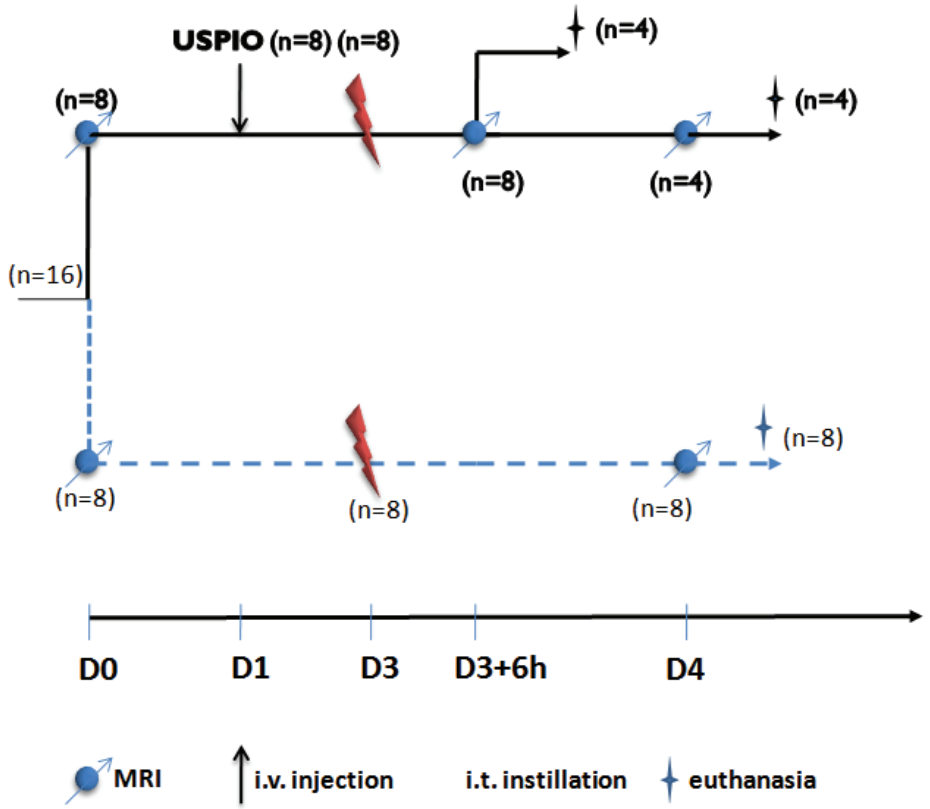

Figure 5.4: Protocol design for study II

specifically, Ferumoxtran-10 (Sinerem; Laboratory Guerbet, Roissy, France) were utilized as a contrast agent.

The nanoparticles consist of iron oxide nuclei (Fe_2O_3 and Fe_3O_4) crystals coated with dextran. The mean diameter of the particles is 35 nm and its half-life in rat blood is between 2 and 3 hours at a dose of 40 μ mol/kg (26).

Due to the action of the phagocytic system - which is responsible for removing all intrusive particles from the blood stream - these intravenously injected particles are removed from the circulatory system. The blood resistance of iron oxide nanoparticles differs between species. The particle's intake is dependent on their physical properties such as a particle size and their surface type and is proportional to the particle's concentration.

The biodistribution studies performed with Ferumoxtran-10 showed that with a dose of 3.4 mg of Fe per kg, 38% of these particles were found in the spleen, 26% in

Table 5.1: The summary of the materials and methods.

Study	Animals species	LPS exposure	Contrast enhancement	Imaging time
I	Wistar (n=7)	Selective into left lung LPS dose: 1 mg in 0.2 mL of saline	No contrast used T1-weighening of imaging sequence	24 h after LPS administration
II	Brown Norway (n=12):	Homogenous distribution	USPIO: administration i.v., (dose 600 μM of Fe/kg)	With respect to LPS administration: 6h and 24 h post instillation
	USPIO injected, LPS instilled (n=8) Control: only LPS instilled, (n=4)	LPS dose: 1 mg in 0.2 mL of saline	T1/T2* enhancement of USPIO	With respect to USPIO injection: 48h and 72h post administration

the liver and 10% in the lymph node with the peak appearing between 6 and 24 h after contrast injection (5). Insignificant changes in iron level during the first 24 h after i.v. administration was demonstrated in other tissues like the lungs, kindey, brain and heart.

A progressive saturation of macrophage uptake by the liver and other macrophage-rich organs, result in a long half-time of these particles which renders them suitable for its labeling outside of these organs.

The USPIO particles have strong magnetic properties that affect both the T1 and

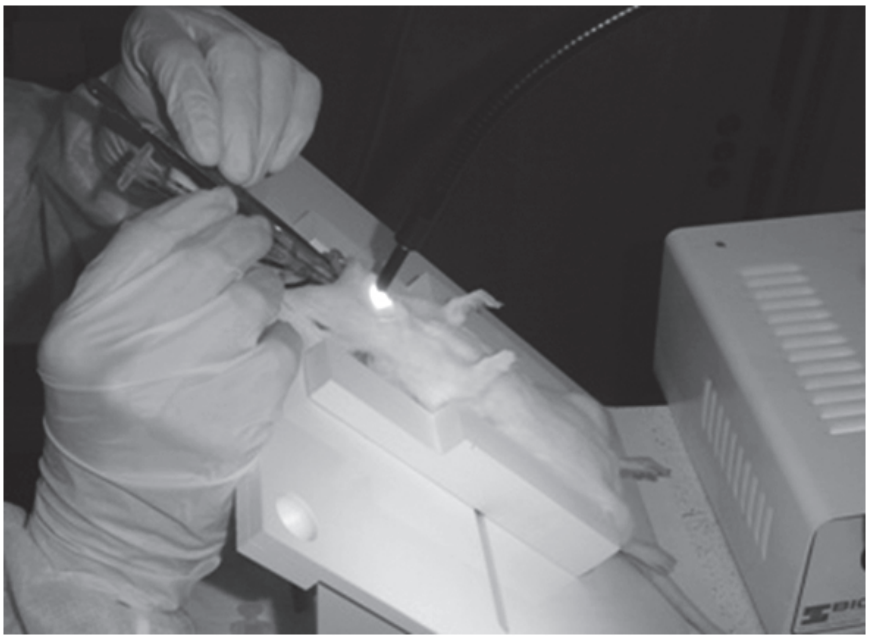

Figure 5.5: An example of the LPS-instillation setup. For instillation of agents, a rat is positioned supine with the head tilted up. It is intubated perorally with a 26-gauge flexible polyethylene catheter into the trachea. 0.2 mL of solution is injected.

T2 proton relaxation times, as well as result in magnetic field perturbation leading to T2* effects (26). The relaxivities, r1 and r2, of freely dispersed Ferumoxtran-10 at 4.7 T are 2.8 and 118 mM-1s-1, respectively (19), and they decrease while particles are compartmentalized in macrophages down to r1 = 0.1 and r2 = 79 $\mathrm{mM}^{-1}s^{-1}$ (19). The opposite effect is noted in the case of r2* relaxation, which is equal to $66mM^{-1}s^{-1}$ in freely dispersed particles and increases up to 540 $\mathrm{m}M^{-1}s^{-1}$ when macrophages are labeled (19).

The magnetic properties result in contrast modulation attributed to the particles distribution in the subject. Typically, negative (T2*) contrast is obtained with the use of these particles, however positive contrast can also be obtained with the USPIO (41)- for example using the UTE imaging sequence.

Furthermore, it must be noted that the magnitude of the relaxivities also depends on many other factors such as compartmentalization of the contrast agent, type of imaging sequence and aggregation of the contrast agent as well as a strength of the magnetic field.

The contrast agent used in this study was delivered as a powder and reconstituted

prior to the experiment with 15 ml of 0.9% NaCl giving solution containing 21.6 mg Fe/ml. It was administrated intravenously by means of the rat tail vein at a dose of 600μmol of iron/kg (33 mg Fe/kg). The administration was performed 24 h before LPS challenge (See Figure 5.3) and 48 h and 72 h before MR imaging.

5.6.4 Imaging Parameters

Study I

Measurements were carried out with a Biospec 47/40 scanner (Bruker, Germany) operating at 4.7 T. The details concerning the MR scanners parameters are presented in chapter 3.

Two different approaches were compared: the first approach used a conventional gradient-echo imaging sequence which permits one to obtain a high contrast between dark-appearing lung parenchyma and the expected fluids due to inflammation. Furthermore, using this imaging sequence, motion artifacts can be reduced by signal averaging.

The second approach, based on a radial ultra-short echo time sequence, is less sensitive to motion and blurring artifacts occurring in the thoracic cavity during respiration. It can, thus, provide a more reliable visualization of fluids due to the inflammation. To evaluate the accuracy of edema detection using these two approaches, a set of axial images covering the entire lung volume was obtained using a multi-slice acquisition. The sequence parameters were chosen to ensure vizualization of edema via T1 enhancement. The following sequence parameters were used:

- Gradient echo imaging

TR=150 ms, TE=3 ms; bandwidth=100 kHz, flip angle=30° , FOV=$6 \times 6cm^2$, matrix size=256×256, slice thickness=1.5 mm and interslice interval=2 cm. 20 averages were applied to limit motion artifacts in the free-breathing animals resulting in an acquisition time of 13 minutes. To cover the entire lung volume, 12 consecutive axial slices were used.

- Radial ultra-short echo time imaging

TR=80 ms, TE=670μs; band width=64 kHz, flip angle=20° , FOV=$6 \times 6cm^2$, 800radial views/image, 128 points/view and slice thickness=1.9 mm. A multi-slice acquisition with 4 averages was applied. Neither cardiac nor respiratory gating was used. The total acquisition time was equal to 8 minutes with an acquisition covering 12 contiguous axial slices.

During MR acquisitions rats were anesthetized with isoflurane (1.7%) in a mixture of O2:N2O (1:2) administrated via a face mask. Circulating water was used to maintain the body temperature of the rats during image acquisition.

Study II

MR measurements were performed with a 4.7 T Oxford magnet (10-cm wide bore) interfaced to a Bruker MR console (Bruker, Ettlingen, Germany). In order to delineate the inflammation extent, the radial UTE T2*-weighted multi-echo sequence and T2*-weighted gradient-echo sequence were used throughout the study. The following sequence parameters were applied:

- Radial ultra-short echo time imaging

TR=200 ms, TE= (0.67, 0.97, 1.17, 1.67, 2.1) ms; band width=64 kHz, flip angle=30°, gaussian-shaped pulse length=0.2 ms, FOV= $6 \times 6cm^2$, 400 radial views/image, 128 points/view and slice thickness=2.5 mm. A multi-slice acquisition with 2 averages was applied. To cover the entire volume of the lungs, 13 contiguous axial slices were acquired. Neither cardiac nor respiratory gating was used.

- Gradient echo imaging

TR=5.6 ms, TE=2.7 ms; bandwidth=100 kHz, flip angle=15° , FOV= $6 \times 6cm^2$, matrix size=256×128 and slice thickness=2.5 mm. A single slice with 60 averages was acquired. 13 slices in total were acquired with slice positions corresponding to the ones acquired with the radial sequence.

During the MR examination, the animals were kept under dissociative anesthetics (mixture of ketamine and xylazine) for approximately 1 hour.

For both protocols, image reconstruction from radial acquisition was performed using a gridding algorithm (see Chapter 3) with IDL. The reconstruction oversampling factor was equal to 2, sampling density compensation was performed using the Jacobian of the transformation, Kaiser-Bessel kernel parameters were the following: shape factor $a = 2.8$, window width $L = 3.0$, final reconstruction matrix was equal to 512×512. The regional T2* values were calculated from linear fit as described in Chapter 6.

5.6.5 Optimal imaging times

According to literature, the optimal imaging time to observe edema is between 24-48 h after LPS exposure (14), (88) with a peak appearing at 48 hours after instillation. However, according to some studies (14), (98) the inflammation can be detected in the

pleura during earlier stages of inflammation (6h after the challenge). Furthermore, it was reported that in endotoxin-induced lung inflammation model, the cellular infiltration occurs several hours following the challenge.

The imaging protocol of **study I** was performed 24 h after LPS instillation. At this time point, all animals developed a severe edema (visible as hyperintense signal regions on the T1-weighted images). For early stage inflammation detection (**study II**) the imaging protocol was performed at 6 h and repeated at 24 h after LPS instillation.

5.6.6 Quantitative analysis

Study I

For quantitative analysis, the volumetric measurements of lesion extent were performed. Twelve slices covering the lungs of each individual animal were inspected and regions comprising the lesions were manually delineated. From the defined region, the logical mask was created and enclosed pixels counted. An exemplary logical mask covering an inflammatory region is shown in Figure 5.6

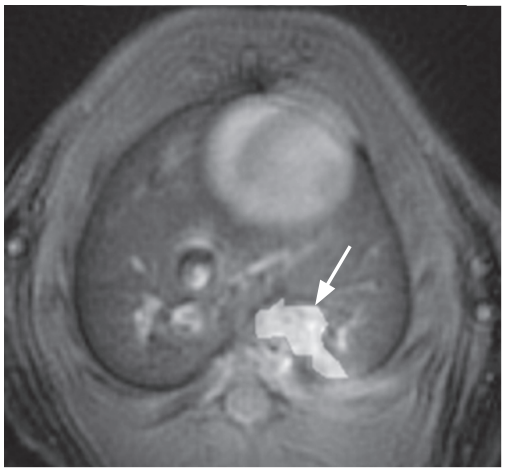

Figure 5.6: The example of image from rat thorax instilled with LPS. The arrow indicates a mask covering an inflammatory region.

For repeated measurements, the mean, standard deviation and the coefficient of variation of the segmented regions were calculated. Coefficient of variations was defined as normalized measure of dispersion (CV=σ/mean), where σ is a standard deviation .

Study II

For quantitative analysis, the signal intensities on multi-echo UTE images and T2* values on T2* maps were measured within the regions of interest (ROI) on the images acquired 6 h and 24 h following LPS administration. TE values for T2* measurement ranged between 0.67 ms and 2.1 ms (see section 5.6.4)

The ROIs were placed in the inflammatory region, within the healthy region of the lung parenchyma, and in the muscle. The mean signal intensity of the ROIs were calculated from the images acquired with two different echo times (TE) equal to 0.6 ms and 2.1 ms. The T2* values and signal intensities measured in inflammatory regions were statistically analyzed with the Student t-test.

The statistical analysis involved the data from the rats exposed to LPS and USPIO versus control (only LPS instilled). Two different groups were established, as the USPIO administration was performed 48 h and 72 h prior to imaging, namely (LPS+/USPIO 48 h) for the group USPIO treated 48 h before imaging, and (LPS+/USPIO 72 h) for the group USPIO treated 72 h before imaging.

Additionally, statistical analysis of the kinetics of T2* and signal intensity values was performed. Statistical significance was determined at the level of $P<0.05$.

5.6.7 Histology

Study I

The protocol for study I, did not involve histological analysis.

Study II

Immediately after the acquisition was finished, the rats were euthanized with an overdose of pentobarbital (250 ml/kg). For the tissue fixation, the lungs were removed from the thorax and perfused via a trachea with buffered neutral formalin, then sectioned and embedded with paraffin. Lungs were trimmed and sliced for histological analysis. The staining was performed with (i) hematoxylin and eosin to assess the general morphology, (ii) Perl's Prussian blue to demonstrate iron presence, (iii) monoclonal antibody ED1 to show macrophages and (iv) ED1/Perls to detect whether iron was phagocyted by macrophages. The histological analysis was performed at the Novotec lab (Lyon, France).

5.7 Results

Study I

Figure 5.7 shows some representative axial slices acquired with Cartesian (gradient-echo) and radial UTE sequences after exposure to LPS. The corresponding gradient-echo and UTE images were acquired in the same session with the same animal.

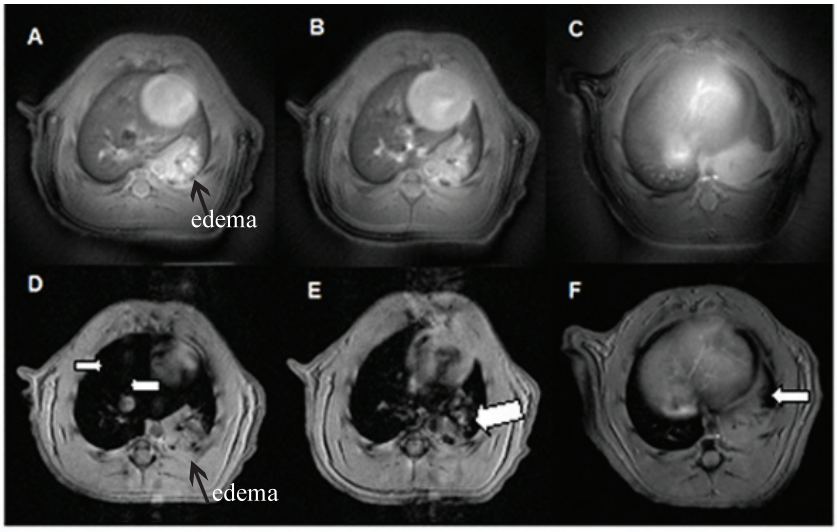

Figure 5.7: UTE radial images (A-C) and corresponding Cartesian images (D-F) acquired in the same animal. A diffuse edematous signal is indicated. White arrows indicate motion artifacts from arteries, the heart and diaphragm motion.

For both MR sequences, the left lung instilled with LPS exhibited significant hyperintense regions, as compared to the control (right) lung, see Figure 5.7. These hyperintense regions were attributed to fluids due to inflammation. They were observed as having a diffuse appearance (see for example Figure 5.7A) similar to that observed by Beckmann at al. (12) after an allergen challenge and they were related to edema formation as described in (8), rather than to mucus (14).

Considering the contrast of images, one can note that UTE images provide improved contrast for detecting inflammatory regions as compared to these of gradient-echo images when the boundary of edema and muscles are of concern (for example see Figure 5.7 A and D).

White arrows in Figure 5.7 indicate the presence of motion artifacts due to the

arterial flow (Fig 5.7D), heart beating (Fig 5.7E) or diaphragm motion (Fig 5.7F). None of these motion artifacts significantly affects the corresponding radial UTE images.

Figure 5.8 shows the mean lesions volume quantified from the gradient-echo and UTE images for individual animals. The volumetric measurements were performed at two different time points. The coefficient of variation was used to estimate intra-rater reliability (61) of the segmentation procedure.

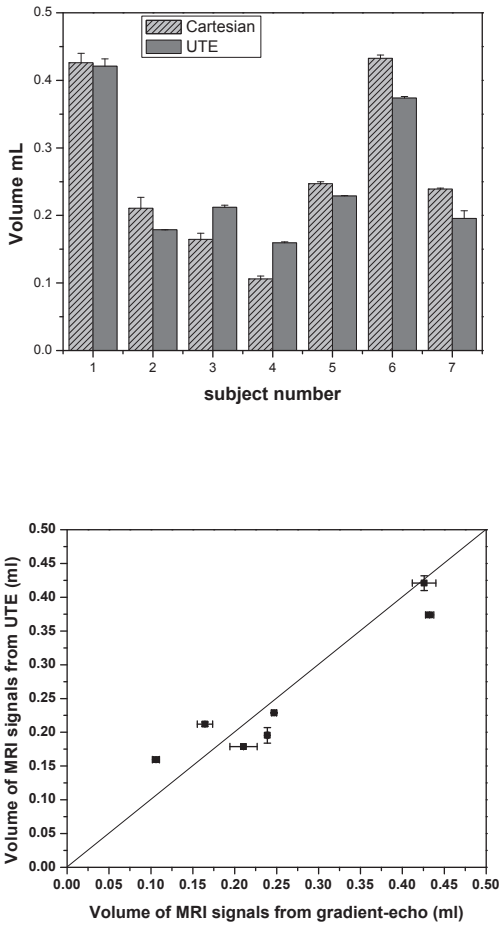

Figure 5.8: Mean lesion volume quantified from the gradient-echo and UTE images for individual animals. The bar error represents standard deviation of the measurements.

The images were manually segmented, by an observer having expertise in lung anatomy, yielding lesion volume for each protocol. The same images were then seg-

mented again by the same observer two days later. Combining the volumetric results obtained over two segmentations gives a mean lesion volume and a standard deviation of the volume calculation (109). These two values yield the coefficient of variation. This procedure was repeated for each of the 12 slices covering the lungs of each individual animal (N=7). The mean coefficient of variation (averaged across 7 animals) for each protocol is shown in Figure 5.9. The CV calculated for the UTE technique was found to be less than half that of the Cartesian technique, showing segmentations performed on data acquired using the UTE technique to have improved intra-rater reliability.

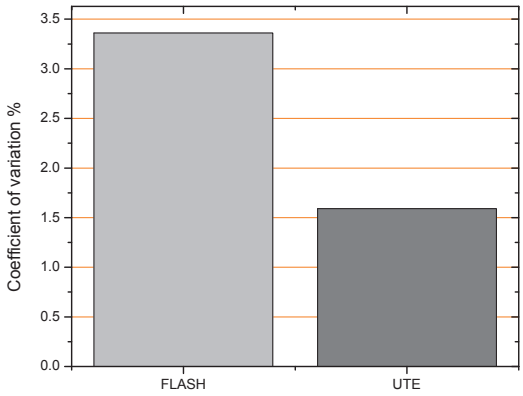

Figure 5.9: Mean coefficient of variation for Cartesian and radial imaging protocol.

Study II

5.7.1 MR Imaging

Six and twenty-four hours after LPS instillation, the inflammatory area with fluid secretion could be detected on the images. This fluid was attributed to edema (98) and it likely correlates to inflammatory cells assessed in the broncho-alveolar lavage fluid, including macrophages, as reported previously in (120).

Figure 5.10 and Figure 5.11 show the result from quantitative measurements. The signal intensity versus TE, as well as T2* values measured with respect to 6 h (Figure 5.10a) and 24 h (Figure 5.10b) following LPS instillation are presented.

The MR signal was measured in ROIs placed in the regions of the lung parenchyma containing edema and normal tissue. Additionally, the signal was measured in regions

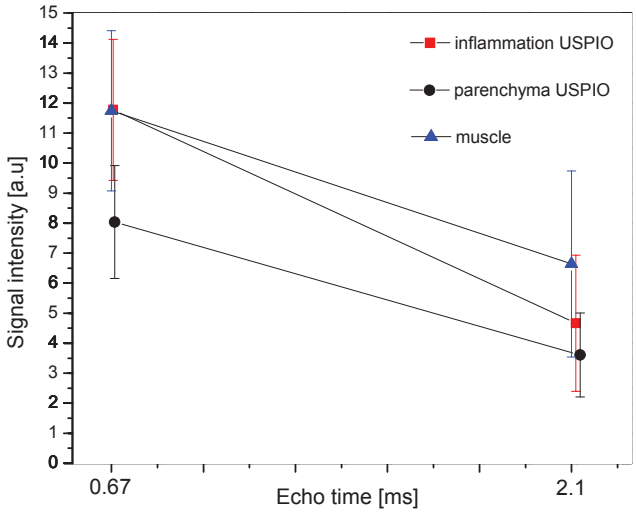

(a)

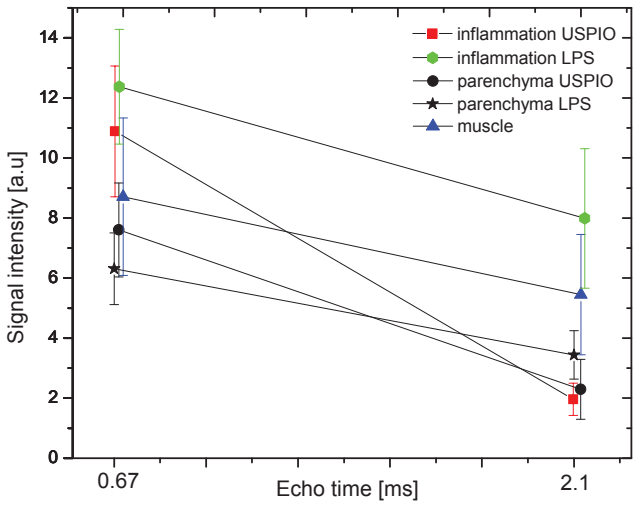

(b)

Figure 5.10: Mean signal intensity measured from images at very short (0.67 ms) and long TE (2.1 ms) at 6 h (a) and 24 h (b) after LPS administration

of muscles. The measurements were performed in a group of animals treated with both, USPIO and LPS (i); and a control group - treated only with LPS (ii).

Considering regions from the normal lung parenchyma, as seen from Figure (Figure 5.10), the signal intensity measured at a short TE were comparable in USPIO/LPS treated and control animals.

A slightly steeper gradient of the signal intensity decrease with a longer echo time was observed for the group of the animals treated with USPIO as compared to the control group (5.10b). Nevertheless, the T2* values measured in the regions with the normal parenchyma between those two groups, did not show a statistical differences.

The signal intensity measured in the edematous regions of the lung parenchyma was comparable for the two groups of animals at the shorter echo time. Hovewer, at the longer echo time a pronounced signal intensity drop was visible in the group of animal treated with USPIO. This observation was consistent with lower T2* values found in the USPIO-treated group (Figure 5.11).

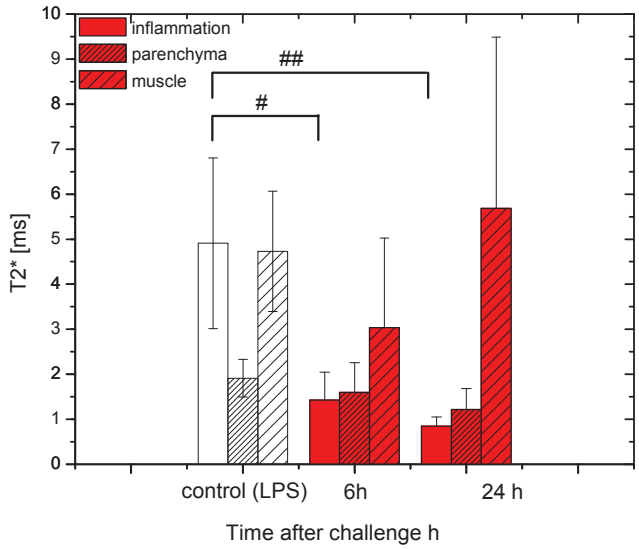

Figure 5.11: T2* kinetics measured in the inflammatory regions, healthy parenchyma, and muscle following LPS administation in the control group and USPIO-treated group of animals. In the group of animals treated with USPIO, the rats were challenged with LPS after USPIO was administred. Significant statistical differences were observed at 6 h and 24 h after LPS challenge (P<0.004). # $P < 0.001$, ## $P < 0.00001$

The T2* value drops were statistically more pronounced (P<0.0004) at 24 h following the LPS instillation (mean: 0.84±0.2), as compared to those at 6 h after challenge (mean: 1.47±0.6). Accordingly, significant drop; 5 ms in LPS group versus 1.9 ms in the USPIO group at 6 h following LSP challenge, and 5 ms in LPS group versus 0.6 ms in the USPIO administrated group, was observed. Statistical significance of the signal drop was P<0.001 at 6 h following LPS administration and P<0.00001 at 24 h after challenge. No statistical differences in T2* values were found in the regions from the muscle between groups at any point in time with regards to LPS challenge.

Figure 5.12 compares a series of radial images with increasing TE value acquired 24 h following LPS administration with USPIO injection (Figure 5.12 top) and without the contrast agent (USPIO) (Figure 5.12 bottom). Considering the images acquired following the USPIO injection, the edematous regions with strong signal intensity decrease at longer TE, could be delineated. These regions were characterized by very short relaxation times, visible on T2* maps (Figure 5.13). Contrarily, long life-time signal, characterized by a long T2*, was observed in the control rats which were exposed to LPS exclusively.

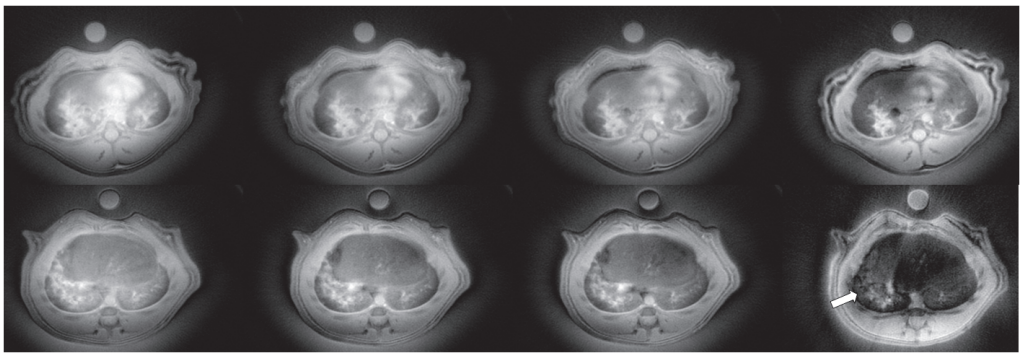

Figure 5.12: Series of images acquired with different echo times (0.67, 0.97, 1.17, 1.67, 2.1) ms at 24 h following LPS administration in control (top) and USPIO administrated (bottom) rat. Note strong signal decay (white arrows), due to susceptibility effect of USPIO administrated 72 h prior to imaging. None of these effects was visible in control images acquired 24 h after LPS challenge without the USPIO contrast agent.

The effect of a signal drop at longer TE values, visible with USPIO-treated animals, was attributed to the susceptibility effect due to the presence of iron-loaded macrophage infiltration into the site of inflammation. The presence of macrophages with intracellular iron accumulation was proved by histological examination (See Figure 5.18(c)).

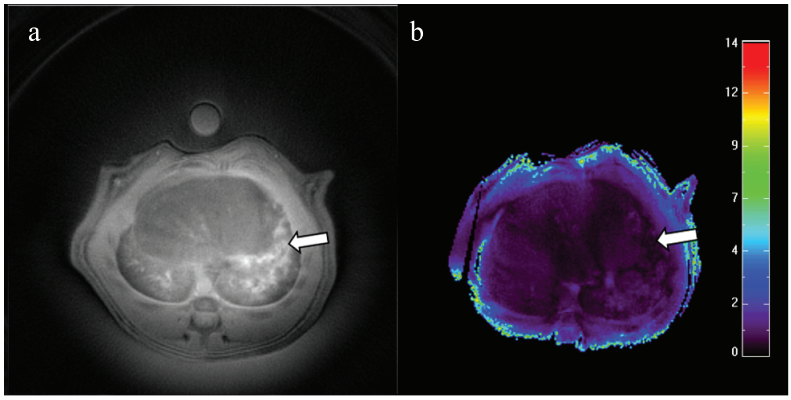

Figure 5.13: An example of T2* map for rat injected with USPIO at 24 h prior to LPS instillation. Arrows indicate strongly attenuated signal in the region of inflammation.

The images acquired at 6 h (Figure 5.14) following the LPS instillation, showed different distribution patterns of inflammatory areas as compared to those of 24 h after the challenge, (Figure 5.14). The lower value of T2* parameter at 24 h following LPS instillation suggests that this is likely due to an accumulation of iron-loaded macrophages from intravascular to the alveolar compartments.

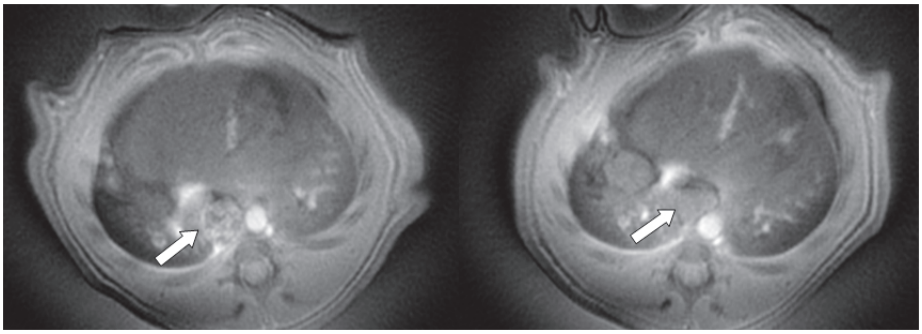

Figure 5.14: Images of rat's thorax acquired from the same animal treated with LPS at 48 h (left) and 72 h (right) following USPIO administration. Note inflammatory pattern changes with time in the inflammatory area.

Figure 5.15 shows an example of an image acquired prior to and 24 h after LPS administration for the group of animals receiving USPIO. The images corresponding to the later time point (24 h) acquired with gradient-echo (Fig 5.15 c) and UTE sequence (Fig. 5.15 b) were compared. Considering the lung tissue, one can note the regions with attenuated sinal intensity visible at UTE images (see Figure 5.15 b,c). These

regions are likely associated with macrophages infiltration causing local susceptibility gradients, even though no edematous signal was visible in the images. Notably, the signal alterations due to the susceptibility effect were pronounced in UTE images and make it possible to delineate the inflammatory region while the same region was hardly distinguishable in the corresponding image acquired with the gradient-echo sequence.

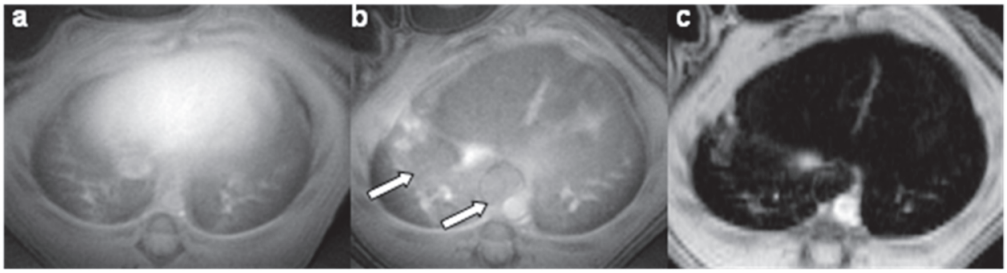

Figure 5.15: Axial images acquired prior (a) and 24 h after LPS challenge (b and c). The rat received USPIO 72 h before MR imaging. The arrows indicate inflammatory regions detected in UTE image (b), which cannot be delineated in the corresponding gradient-echo image (c).

It was of interest to examine whether this signal attenuation is detectable in the lung parenchyma even if no inflammation was induced. Figure 5.16 compares the images from the control rat (without USPIO administration) and image acquired 48 h after USPIO administration. It can be seen that no regions with signal attenuation due to the susceptibility effect were noticeable in the lung parenchyma images.

Notably, MR imaging confirmed that at this point in time, the iron particles were accumulated in the liver (Figure 5.17 a) and lymph's node (Fig 5.17 b). The signal enhancement detected in the vessels suggests that free iron particles can circulate in the vessels at this time point.

5.7.2 Histology

Figure 5.18 presents a histological section of lungs treated with LPS. Hematoxylin-eosin staining showed a mixed cellular infiltration of polymorphonuclear cells and macrophages around vessels (Fig 5.18 a,b). It was observed that iron-staining was co-localized with macrophages in the antigen (CD68) challenged section (Fig 5.18d). Also, iron particles stained with Perls Prusian blue were found in the same areas where iron-containing macrophages (Fig 5.18c). No free iron particles were present in the

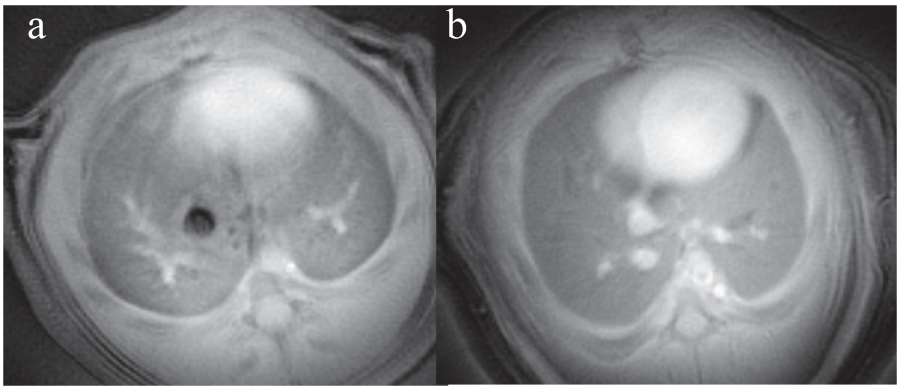

Figure 5.16: Images of the rat's thorax without the contrast agent (a) and USPIO injected 48 h prior to MR imaging (b).

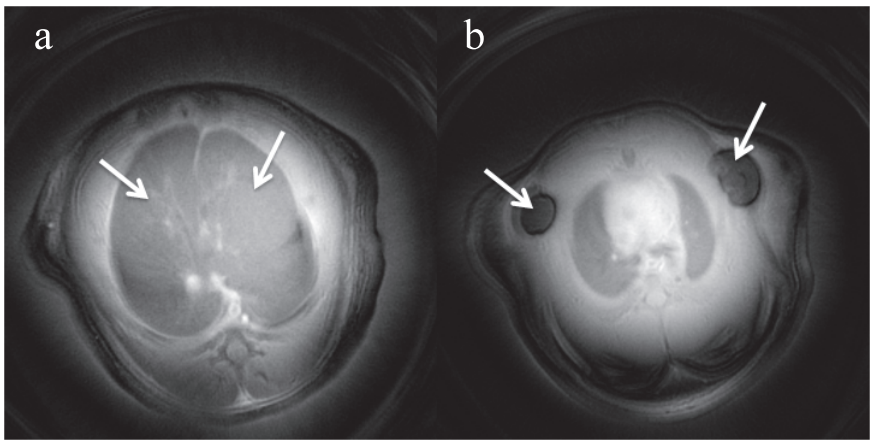

Figure 5.17: Images of the rat's thorax at different thorax level, showing distribution of iron at 48 h after USPIO injection. The animal was not exposed to LPS.

parenchyma tissue. However, 72 h after USPIO administration, a few free iron particles were found is the vessels. No iron particles or iron containing macrophages were found in rats that had not received USPIO prior to the image acquisition.

5.8 Discussion

In these studies, the detection of inflammation markers in rat lungs following LPS administration was demonstrated using the ultra-short echo-time MRI. Considering MRI, traditionally the extent of the inflammatory area is defined by the edema pattern, visible as regions with signal enhancement on T1-weighted MR images. The challenge of

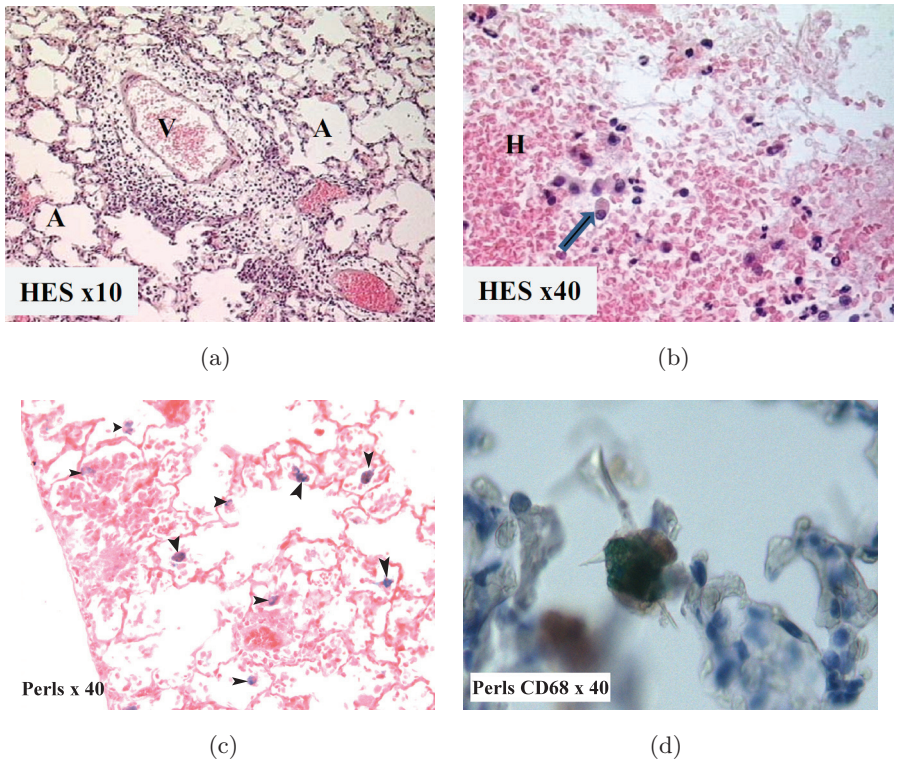

(a) (b)

(c) (d)

Figure 5.18: Histological analysis. H&E stainning of lung tissue from LPS treated rat (a). Note, a significant perivascular cellular infiltration. V indicates a vessel. The cellular infiltration constitutes numerous granulocytes and histiocytes indicated by the arrow in (b). Iron staining shows staining in macrophages indicated by black arrows (c). Immunostainning with the anti-macrophage antibody and iron shows staining in the macrophage (d).

edema volume estimation in the lungs rises from motion in the thoracic cavity which can influence the quantification of the inflammatory areas - frequently leading to overestimation of the lesion volume. Thus, the choice of the acquisition strategy is crucial to assess the extent of inflammatory regions. Conventional gradient-echo MR imaging combined with the signal averaging strategy has been recognized as an efficient tool in assessing the edema volume, considering that a significant contrast is obtained between a dark-appearing lung parenchyma and a hyperintense edema and assuming that the motion artifacts can be suppressed for the images following the sufficient number of averages.

In the study I, we have shown that the detection and quantification of edema was

feasible with the radial UTE technique. Due to the robustness of this technique against motion, neither respiratory, nor ECG triggering was necessary, and rats were freely-breathing during acquisition.

To validate this technique for in vivo edema detection, the images acquired with UTE and traditional gradient-echo sequence were compared. When the motion of organs is of concern, we have shown the advantages of the UTE radial technique compared to Cartesian-based acquisition.

In our experimental set-up, image contrast in UTE images was clearly superior for detecting inflammatory regions when the boundary of edema and muscles is of concern. This high contrast achieved with UTE sequence allowed for a more reliable delineation of the lesion volume compared to the gradient-echo approach.

In our protocol, it was not possible to estimate which acquisition method gives a more accurate estimate of fluid volume because a histomorphometric correlation study was not performed. The correlation study is envisaged to be performed by means of quantitative histology and the micro CT techniques.

In order to compare quantitatively the two techniques, the reliability of the calculated lesion volume was estimated. The reliability of lesion volume estimation for the two protocols were assessed by means of an intra-rater reliability test assuming that the quality of image impacts the results of volumetric measurements (61). The results showed a two-fold improvement in the coefficient of variation for the volumetric estimation using the UTE technique compared with the gradient-echo method. This result demonstrated that more reproducible volume measurements can be obtained using UTE image acquisition. Furthermore, we suggest that this acquisition technique would be preferred when automatic segmentation is performed due to its improved lesion extent delineation as compared with gradient-echo technique.

Another advantage of the radial UTE acquisition technique is its inherently short TE. One can expect that a measured volume with the UTE technique might give higher scope of the lesion extent compared to those detected with the gradient-echo acquisition. It is because of the contribution of the short T2* components in the inflammory fluids that might derive from mucus. These components can be detected with the UTE approach but it is not possible to visualize them with conventional imaging, as they are operating at higher TE.

In our protocol the volume detected with UTE technique was not greater than those calculated for gradient-echo approach. The reason for that is the characteristic of presented fluids in LPS challenged animals. The appearance of these fluids in our protocol was edema-like characterized by long T2* relaxation times. Therefore, MR signal from observed fluids could be detected in the TE regime of both UTE and gradient-echo sequence. The appearance of inflammatory fluids was different from those reported previously by (8) with weakly apparent MR signals from mucus. The reason for acute inflammation with strong edema formation after LPS can be attributed to a two-fold increase in the LPS dose as compared to those used by Beckmann et al. (14), since the product was instilled selectively into one lung. Additionally, a different strain of rat (Wistar versus Brown Norway) was used for the experiment, which could contribute to the observed differences.

In order to understand why signal patterns differed from those observed by Beckmann et al., (8) and establish the origin of the observed signals, a histological analysis should be performed.

Study II

The identification of inflammatory regions via the detection of hyperintense regions in proton MR images relies on an increased proton density due to the edema formation in the lung.

An alternative criterion to define the extent of inflammation would be to determine the area of cellular inflammatory infiltrates. The tracking of inflammatory cells in the lungs following the LPS exposure was the objective of the second study (**study II**).

The early response to endotoxin-induced lung inflammation includes neutrophilic infiltration and mononuclear phagocytes (MPs). These cells invasion, play decisive roles in different inflammatory states and it occurs as an early response to inflammatory stimuli.

Quintana et al., showed that a three-fold increase of the number of macrophages was observed in the BAL fluid 6 h following the LPS challenge (98). Neutrophils constituted 80% of the total cell detected. The presence of these cells was suggested to be a likely reason for the early activation of a pathway following administration of LPS that precedes mucus release observed at the later time intervals (98).

In this study, we demonstrated that iron oxide nanoparticles, such as USPIO can be used to localize the cellular infiltration by means of the contrast modulation due to

their susceptibility effects on UTE MRI in the lungs. Injected intravenously USPIO are phagotyced by monocytes in the blood which under inflammatory stimuli get activated and migrate to the site of inflammation.

The infiltration of the iron-labeled cells into the inflammatory regions was reported in several animal models of disease. However, this approach of inflammation assessment to the lung, remained elusive.

A major challenge when using IONPs is the need to recognize the regions of signal void due to their accumulation which in case of dark-appearing MR in the conventional images of the lungs, is unachievable.

Here, the localization of macrophage infiltrates was possible to delineate due to the contrast modulation with progressively increased TE using the UTE technique.

Accordingly, the use of the UTE technique resulted in the detection of MRI signals from cellular infiltrates at points in time when gradient-echo images provided no evidence of lung damage (Figure 5.15).

The strong signal attenuation due to the susceptibility effect in the edematous regions detected in T2* maps allowed us to make conclusions regarding the presence of the inflammatory cells in the edema extent. This observation was correlated with histological findings showing infiltration of IONPs into the inflammatory regions.

Complex signal behavior was observed with regards to time after LPS exposure. The T2* kinetics measured within the inflammation regions was assessed. (Figure 5.11). Lower signal intensity and shorter T2* values due to a higher susceptibility effect with time were demonstrated at 24 h as compared to those measured at 6 h after LPS administration. This effect could be explained by the progressive accumulation of iron particles accordingly with the increased cellular infiltration at later time points of inflammation.

This increase in T2* susceptibility can also be attributed to the reorientation of IONPs into inflammatory cells since this modify T2* relaxivities. It is because the intracellular compartmentalization restricts particle diffusion and thereby enhances the T2* effect of the USPIO in cells. Therefore, the measurement performed 48 h after intravenous USPIO administration might reflect intra and extracellular iron particle distribution, while at the later time intervals (72 h) most of particles were internalized by macrophages, increasing T2* effect. Considering this scenario however, the specificity and sensitivity of this approach might be of concern.

The lung's mononuclear phagocyte system consists of along the resident alveolar and interstitial macrophages which are always present in the lung parenchyma to protect them against air-born particles, as the lung is an open organ (114).

Hypothetically, USPIO is endocyted in monocytes or macrophages of the bloodstreams in pulmonary capillaries or elsewhere before the loaded-cells enter the infected area. However, the passive transmigration of free iron particles through the interendothelial junctions in pathologic tissue in which a subsequent increase of the vessel permeability occurs cannot be excluded. In these cases the particles might be internalized by resident macrophages. This might explain the gradual increase of the susceptibility effect in time.

This biological riddle can be answered by microscopic analysis. From our histological observation, it was not possible to distinguish between the alveaolar macrophages from the blood borne macrophages. Since no free iron was visible in the parenchyma tissue, this allows us to believe that iron was internalized before entering the parenchyma. However, this observation has to be proved quantitatively or by applying more refined techniques allowing the discrimination between the alveolar and the bloodstream macrophages.

In future studies, in order to increase the sensitivity of detection and inflammation localization one should avoid the contribution of lung resident macrophages in phagocytosis.

This represents one of the major challenges of this work. To rise to this challenge one has to optimize the opportunities available for macrophage labeling by an appropriate dosage of the contrast agent, as well as finding an appropriate time for its administration.

5.9 Summary and Conclusions

In these studies, we have proposed new approaches for inflammation extent delineation. These approaches were based on the ultra-short TE acquisition method. Using the specific properties of the UTE technique, namely robustness with respect to motion and a very-short echo time, we aimed at the development of protocols for accurate detection of inflammation markers. For this purpose, two different experimental protocols were used. In the first one, a severe edema as a marker of inflammation was induced and

the UTE technique was compared with a well establish method based on Cartesian encoding to test the reproducibility of volumetric measurement. In the second one, thanks to the ultra-short TE offered by UTE, the progressive infiltration of cellular inflammation markers was detected.

USPIO-enhanced pulmonary imaging opens new areas to assess functional information on a cellular level, however further investigations are required to validate the USPIO signal enhancement by inspection of their affinity to specific uptake by macrophages.

6

Non-invasive and non-contrast enhanced assessment of emphysema markers using UTE MRI

6.1 Introduction

In this chapter, a new approach based on UTE imaging for emphysema marker detection will be presented. After a brief description of the disease, the current state-of-the-art in the emphysema diagnostic will be presented. Next, the objectives and the principle method for validating of quantitative measurement of emphysema will be presented. Finally, the experimental results will be demonstated and discussed.

6.1.1 Emphysema

Emphysema is characterized by an enlargement of air-spaces distal to the terminal bronchiole (i.e., alveolar ducts and alveoli) caused by destruction of the alveolar wall (116). An illustration of this effect is presented in Figure 6.1. Emphysema can be classified into two groups: panacinary and centroacinary, depending on the location of the enlargements. In panacinar emphysema, the entire respiratory acinus, from the respiratory bronchiole to the alveoli, is expanded. One hypothesis is that the breakdown of collagen and the elastic fiber network causes the enlargement (111). According to the

protease-antiprotease hypothesis, lung tissue releases proteases which are hydrolytic enzymes that attack connective tissue proteins. This destructive mechanism of protease is controlled in healthy tissue by releasing protease inhibitors. In the event of too much protease, or not enough inhibitors, emphysema is the result. In centriacinar (or centrilobular) emphysema, the respiratory bronchiole (the proximal and central part of the acinus) is expanded, however, the distal acinus or alveoli are unchanged. The emphysema subgroups are displayed in Figure 6.2. Destruction of parenchyma leads to a decreased alveolar surface area with increased alveolar gas volume and decreased elastic recoil. This leads to air trapping, hyperventilation and consequently to the gas exchange impairment.

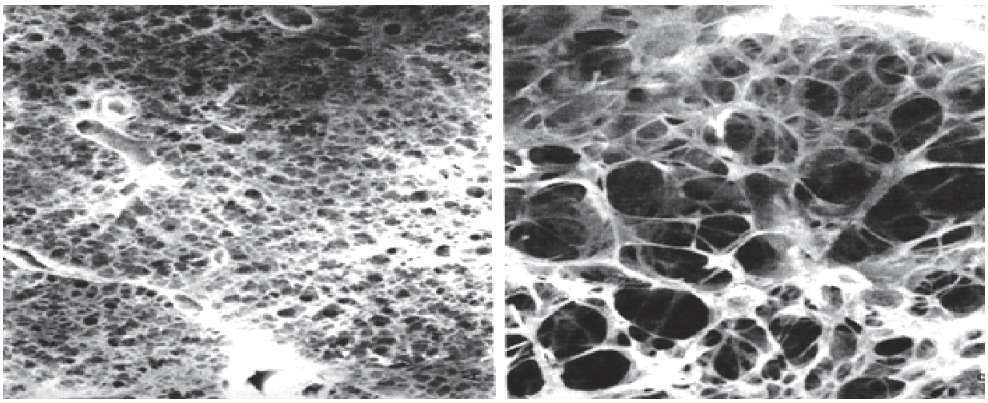

Figure 6.1: An example of the alveolar structure of healthy lungs (left), and emphysemateous lung parenchyma (right). Reprinted from J. West, Pulmonary Physiology and Pathophysiology, Lippincott, 2001 [West2001].

6.2 Problem definition

Several methods to quantify emphysema in humans and animal studies have been proposed. The most accurate method is histomorphometry, however this method is terminal thus cannot be used in follow-up studies. Micro-computed X-ray tomography can be used to estimate emphysema, however its frequent use should be avoided due to the constant exposure to radiation. The hyperpolarized (HP) 3He apparent diffusion coefficient (ADC) tracked by MRI was proposed as a sensitive indicator of emphysema (103), (130), (24). However, escalating cost and scarcity of 3He have inhibited

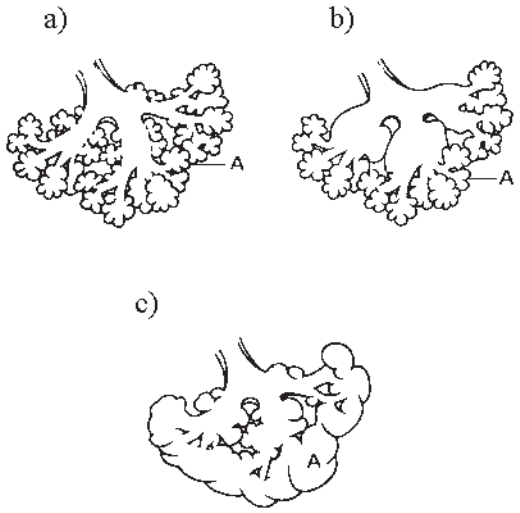

Figure 6.2: Normal (a), centrilobular (b) and panlobular (c) emphysema. A detones alveoli. Scheme modified from Konietzko and Wandel.

its widespread use for medical applications. Thus, there is a need for new sensitive markers of emphysema, suitable with:

- accurate detection and characterization of the disease,
- quantitative assessment of emphysematous damage,
- widespread use for clinical and preclinical diagnostic.

The application of proton MRI to emphysema detection is motivated by its inherent non-invasiveness, its potential to translational research and its complementary diagnostic information as compared to those of CT imaging. However, the low proton density of the lungs combined with the large susceptibility gradients, when conventional imaging sequences are applied result in dark, difficult to view MR images of the lungs.

6.3 Aims of the present study

The main aims of this study were to:

- develop a non-invasive, non-contrast enhanced MR method for follow-up diagnostic purposes in emphysema,

- study the feasibility of marker detection of emphysema,
- study the correlation between MR findings and histological emphysema results,
- evaluate the validity of the method for diagnosis of COPD.

6.4 State-of-the-art

Traditionally, the lung function test is used to monitor the progression of emphysema in COPD patients. Spirometry tests measure the forced expiratory volume in one second (FEV1), which is the greatest volume of air that can be exhaled in the first second of a large breath. Forced vital capacity (FVC) is the greatest volume of air that can be exhaled in a whole large breath [West1999]. Depending on the FEV1/FVC ratio, emphysematous changes can be detected. However this technique is not sensitive to early and mild changes in emphysema (118). Thus, a more sensitive modality is required to assess the early development and progression of disease.

High-resolution computed tomography (HRCT or CT) opens the possibility of emphysema assessment including exact location and estimation of the degree of damaged lung parenchyma tissue. Due to tissue destruction in emphysema, the damaged regions of the lung show lower attenuation, due to tissue density dependent absorption in CT. Differentiation of patients with severe emphysema from those with early stage COPD, using CT, is thus possible. However, inherent exposure to ionizing radiation limits the extensive use of this technique, especially for repeated use in follow-up examinations. Additionally, other emphysema characteristics contributing to airspace enlargement, such as air trapping and perfusion impairment, influence CT attenuation. Therefore, there is a need for new emphysema markers which are capable of sensitive measurements of the disease's progression and which are suitable for longitudinal studies of the disease.

The hyperpolarized (HP) 3He apparent diffusion coefficient (ADC) tracked by MRI is known to be a sensitive indicator of emphysema (31). When hyperpolarized, 3He is inhaled, diffusion of the gas is restricted by the boundaries of the alveoli, and measured ADC reflects the size of peripheral airway spaces (130). The dependence of ADC values on the dimensions of the alveolar space has been thus proposed as a noninvasive approach for probing alveolar structure, and more specifically, the airspace enlargement

characteristic in emphysema. These 3He ADC values have been shown to significantly increase in patients with emphysema, when compared with healthy volunteers (103). Unfortunately, escalating cost and scarcity of 3He have inhibited its widespread use for medical applications. It has been suggested that 129Xenon may also be suitable for diffusion weighted MRI [Mugler et al., Proc ISMRM 2004], (79). It was recently demonstrated that hyperpolaraized ADC measured with Xe are sufficiently sensitive to pulmonary microstructure to differentiate between healthy volunteers and COPD patients with early stage emphysema [Kaushik et al., Proc. ISMRM 2010].

The good solubility of xenon in lung tissue allows one to differentiate between its presence in the alveoli (gas phase) and in tissue (dissolved phase) since xenon dissolved in tissue experiences a large chemical shift (hundreds of ppm) relative to the gas phase.

Xenon polarization transfer contrast (XTC) aims to probe the xenon exchange between alveolar spaces and their surrounding septal walls. This method is based on the selective destruction of xenon polarization in lung parenchyma. Due to the rapid exchange of xenon between the gas and tissue-dissolved phases, the depolarization of xenon dissolved in tissue affects the MR signal from the gaseous phase. The exchange of xenon is measured by monitoring the modulation of the gas phase magnetization due to its exchange with the dissolved phase. It was suggested that this technique might be used to detect global and regional changes in septal wall thickness and tissue-to-alveolar-volume ratio to differentiate between healthy and emphysematous lungs (102).

Emphysema in animal models has been extensively studied using micro-CT, 3He and 129Xenon MRI. With regards to MRI, experimentally-induced emphysema has been investigated in rats (24), (92), mice (33), and rabbits (79) using 3He and 129Xe diffusion MRI, and more recently, a 3D XTC technique [Dregely2010].

Experimental pulmonary emphysema with features of human panacinar emphysema can be induced by porcine pancreatic elastase (PPE) (20), (37), (51) administrated intra-tracheally. Porcine pancreatic elastase has ability to hydrolyze elastin, thus resulting in the alveolar wall damage (16).

Regarding the animal model of elastase induced emphysema, histomorphometry is the most sensitive quantification technique. It is the gold standard for quantifying emphysema (43), (38), (85), using parameters such as: number of alveoli per unit lung volume, mean linear intercept (Lm), and acinar airway radii, (90). It has been reported that micro-CT correlates well with histomorphometry (60).

Recently, proton MR imaging using sequences with reduced echo-time were applied in animal studies of pulmonary disorders. The findings offered by this technique were complementary to those assessed by CT and histology. For example, in a model of cystic fibrosis induced in rats, a short echo-time spin-echo sequence provided results which were well correlated with those obtained with CT (53). More recently, the UTE modalities were applied also to detect experimentally induced emphysema.

Olsson at al., (87) used Single-Point Imaging (SPI) with an echo time of 0.2 ms to detect emphysematous changes in the lungs using a tight skin experimental model. The results he obtained correlated well with histology and CT measurements. However this technique cannot be applied in the large scale for follow up studies of the pharmacological interventions, as SPI requires long acquisition times (87).

Also, a 3T UTE radial technique was proposed to demonstrate the discrimination between healthy and emphysematous lungs in transgenic Klotho mice [Takahashi et al. Proc. ISMRM 2009]. However, these finding were not confirmed by morphometric measurements.

6.5 Proposed solution

The major feature of emphysema is the enlargement of the alveoli. This can lead to reduced local proton density, as well as susceptibility differences of the tissue, as compared to healthy lung parenchyma. Thus, the signal intensity changes and the susceptibility-influenced signal life-time could serve as markers of emphysema, if they were possible to detect.

We propose a radial UTE technique which enables signal from the lung parenchyma to be detected, allowing the investigation of micro structural changes in the parenchyma. We used this technique to probe structural changes of lung parenchyma in an experimental elastase-induced emphysema model in mice. We postulated that measured T2*, together with improved signal detection offered by the UTE technique could provide an additional or alternative quantitative tool to current diagnostic methods. This technique could be easily translated to evaluate regional changes in diagnosing emphysema in human patients. To evaluate the validity of the technique for quantitative emphysema assessment, the MRI findings will be correlated with a linear intercept parameter

determined by histology. Nevertheless, although this study is beyond the scope of this chapter, it will be related in due course in section 6.7.5.

6.6 General study design

The experimental protocol of this study is shown in Figure 6.3. This work was conducted in collaboration with a team at INSERM U955 Paris, France. The experimental model as well as histology was performed by the group from Paris (L. Boyer, P. Caramelle, J. Boczkowski) while MRI and image analysis were performed in Lyon, France (M. Zurek, Y. Crémilliex).

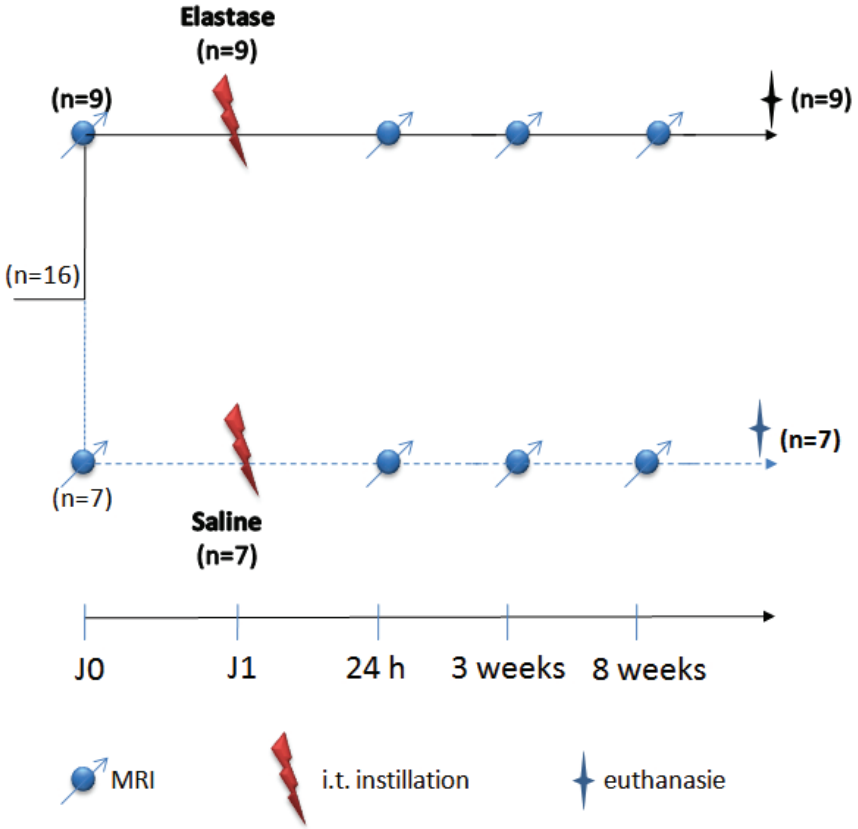

Figure 6.3: Experimental protocol design.

6.7 Materials and methods

6.7.1 Animal care

Experiments were carried out following the INSERM guidelines regarding the fair treatment of animals. The MRI was performed under gaseous anaesthesia with isofluorane (concentration: 1.5%, flow rate: 0.4 L/min) while intramuscular injection of ketamine (1.6 mg: Merial, Lyon, France) and xylazine (300 μg: Bayer, Puteaux, France) was used for elastase challenge and euthanasia procedure.

Male, eight-week-old C57BL/6 mice (N=16) weighing 24-26 g were supplied by Charles River Laboratory (Lyon, France). The experiment was performed after one week of animal accommodation in ambient temperature and 12 h dark-light phase. Elastase was instilled in 9 mice, while the rest of the mice instilled with saline solution served as a control (N=7).

6.7.2 Administration of elastase

Emphysema was induced by intra-tracheal injection of a porcine pancreatic elastase (PPE) into the lungs (see Figure 6.4). All animals were anaesthetized with an intramuscular injection of a ketamine/xylazine mixture, and 5 U in 50 μL of PPE (Elastin Products, Owensville, MO) or saline was administered into the surgically exposed trachea (96).

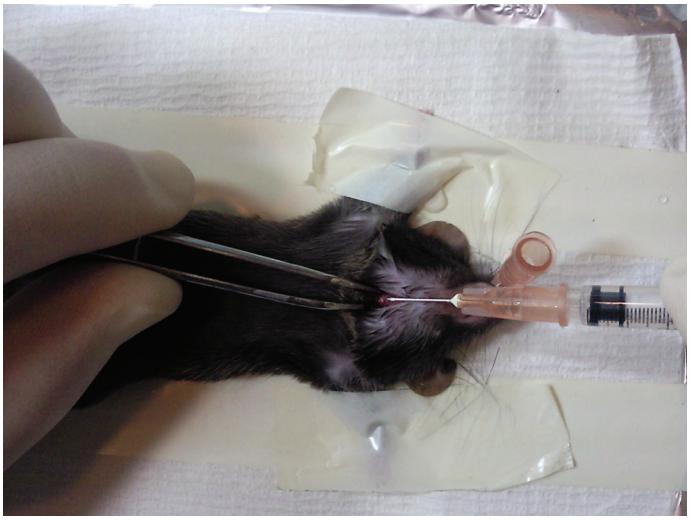

Figure 6.4: Administration of PPE by intratracheal injection in mouse.

All animals survived to the end of the protocol. However, one mouse, 24 h after PPE administration had bristling hairs and appeared be more sedentary compared to the other mice in the cage, demonstrating signs of pain.

6.7.3 MR protocol

A longitudinal study was performed on spontaneously breathing mice before PPE or saline were instilled (baseline) and 24 h as well as 3 and 8 weeks after the challenge. At the end of the protocol, the animals were euthanized for histological analysis.

MR measurements were performed with a 4.7 T Oxford magnet (10-cm wide bore) interfaced to a Bruker MR console (Bruker, Ettlingen, Germany). A radial sequence was used for image acquisition. Four hundred radial views per image with 128 points per view were collected with an angular sampling range of $(0, 2\pi)$ and increment angle of $2\pi/400$ in order to fulfill the Nyquist criterion ($400 \approx 128\pi$) and minimize aliasing image artifacts. The radial projections were evenly spaced in k-space with a successive azimuthal alteration of 180 degrees before each angular increment.

Free induction decay (FID) acquisition was triggered during read gradient ramping, starting immediately after slice excitation and slice refocusing gradient. For each radial view, the k-space origin was acquired with repetition time of 80 ms. The flip angle was set, according to the Ernst angle condition, to 20° . The minimum effective echo time was equal to 550 μs (the effective TE is defined as the interval between the middle of the RF pulse and the first point of the acquisition) and was achieved with a Gaussian-shape pulse excitation of duration of 0.4 ms and slice thickness of 1.7 mm.

Multi-slice scans with 6 axial slices and inter slice distance of 2.5 mm were performed. Signals from 8 sweeps of radial acquisition were accumulated, resulting in 4.2 minutes of acquisition time. For the T2* assessment of the lung parenchyma, a series of axial images with progressively increasing TEs was acquired. Images with 5 different TE value (0.55, 0.97, 1.26, 1.76, 2.46 ms) were acquired, resulting in 21 minutes of acquisition protocol for each animal.

Image reconstruction was performed using an in-house program developed in IDL. Following the gridding algorithm, the images were interpolated to a 512x512 image matrix.

6.7.4 Image analysis

For quantitative analysis, signal intensity and T2* values were measured within the regions of interest (ROI) prior to, as well as 24 h, 3 and 8 weeks after elastase administration. The ROIs were placed in the left and right lungs at identical positions over time, and in the area of the skeletal muscle. The location of ROIs in the lungs were defined in the axial plane, as shown in Figure 6.5, avoiding regions of large pulmonary vessels. The ROI chosen within the muscle served as a reference. The normalized signal intensity, defined as signal intensity measured from ROIs placed in the lungs divided by signal intensity of the muscle, was assessed. The same ROIs location were used to assess regional T2* changes over time, per animal. For T2* assessment, the ROIs were propagated over images acquired with decreasing echo time (TE) and signal intensity from each image were measured.

Using a linear regression function, the natural logarithm of the mean signal of the ROIs were fitted versus TE data and the T2* value was extracted. A similar procedure was applied for T2* map calculation.

The data acquired before and after elastase administration were compared using Student's t-test.

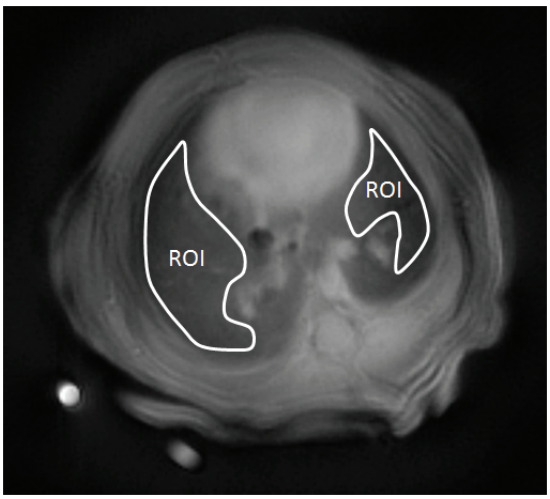

Figure 6.5: Exemplary axial images of thorax with manually delineated ROIs for quantitative image evaluation.

6.7.5 Histology

Immediately after the MRI protocol, animals were anesthetized with injection of ketamine/xylazine mixture and euthanized by exsanguination. A catheter was inserted into the trachea, the lungs were removed from the thorax and were suspended for perfusion. For the tissue fixation, the lungs were perfused via a trachea with a 2.5 % glutaraldehyde solution to a pressure of approximately 25 cm H2O for about 1 hour. Next, the lungs were tied off and immersed in a vial filled with 4% formaldehyde for 24 h. They were then sectioned and embedded with paraffin. To correlate histological and MRI finding, great-axis transversal sections (5 μ m) of the left and right lung were cut in a systematic fashion and were stained with hematoxylin and eosin. The quantification procedure was as discribed previously (96). Ten digital photomicrographs were acquired per lung distributed on the cranial, medial, and caudal regions of each slide at x20 magnification, excluding areas where large bronchi or vessels predominated.

In addition, emphysema will be quantified measuring the mean chord length of alveoli (132) by L.B and P.C, using the public domain NIH Image program at the National Institutes of Health (available at http://rsb.info.nih.gov/nih-image).

6.8 Results

6.8.1 MR Imaging

The effect of elastase was already observed in the lungs 24 h following the administration. In the group of 9 elastase-challenged mice, most of them (7) showed expanded lung volume and attenuated normalized signal intensity, as compared to their baseline images.

In particular, two of the challenged mice showed regions with fluid signals, (see Figure 6.6a) with an appearance comparable to that found by Quintana et al (99) following lung exposition to LPS. According to the experimental model of emphysema induced by elastase, this signal was attributed to inflammation, although histology analysis at this time interval was not performed to confirm this hypothesis.

Together with inflammation, regions with strongly attenuated signal intensity were observed, (see Figure 6.6a). These areas were assigned to a presence of hemorrhage, as described previously (84), (20).

Neither signal elevation due to the inflammation nor evidence of signal decline due to hemorrhage were elusive in MR images at later time intervals (Figure 6.6).

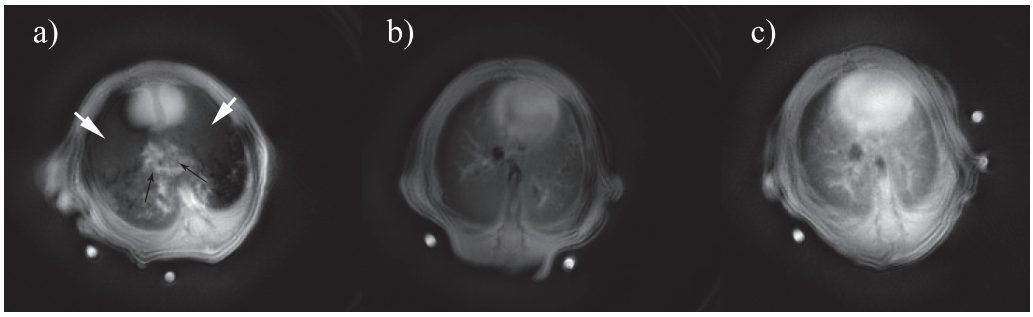

Figure 6.6: Images of mouse thorax from different mice imaged 24 h after administration of elastase (a-c). The black arrows indicate fluid signal related to inflammation, while the white arrows indicate regions with hemorrhage. Part b shows expanded lung volume with lower relative intensity signal, compared to the baseline image. No difference in signal intensity was observed for image c.

Figure 6.7 illustrates the images of the same mouse thorax across the time of the experiment. The example of images acquired 8 weeks after PPE or saline administration are shown for comparison (Figure 6.8). As seen from Figure 6.7, more significant expansion of the lung volume was visible at later time intervals of the protocol (3 and 8 weeks after PEE administration). In many cases, this volume expansion was particularly visible in the left lung as compared to the right one, revealing stronger response with respect to elastase challenge in the left lung. The control mouse, imaged at 8 weeks after saline instillation, did not show expanded lung volume - the feature observed in the case of the mouse instilled with elastase (Figure 6.8).

Together with the lungs enlargement, a reduction in the MR signal intensity was detected in MR images. The normalized signal intensity changes in the lungs measured at TE equal to 0.55 ms was significantly lower in the animals treated with elastase, as compared to their control values.

The result from quantitative measurements are shown in Figure 6.9. The normalized signal decrease measured at the first day after challenge, in the case of the left lung, was 30 %, while the signal decrease measured for the right lung, was 25 %. Subsequently, gradual signal decreasing was observed at later time intervals of the experiment (see Figure 6.9).

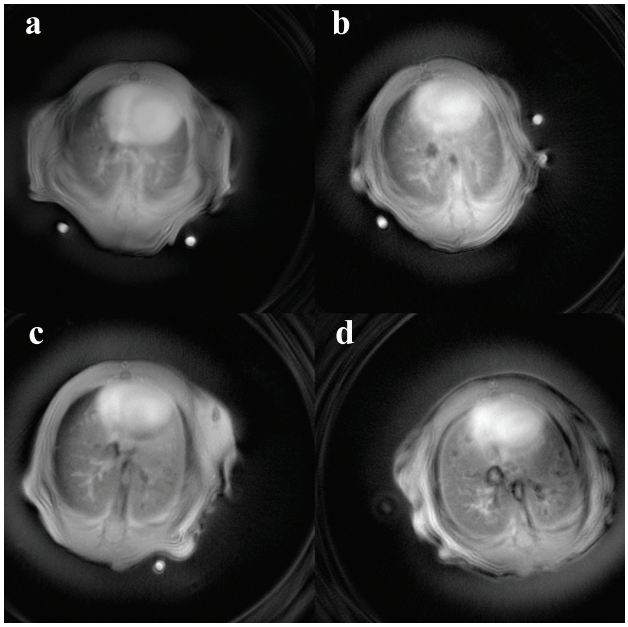

Figure 6.7: Images of mouse thorax from the same animal acquired prior to (a) and 24 h (b) as well as 3 (c) and 8 weeks (d) following the elastase challenge.

The results from quantitative T2* measurements prior to and 24 h as well as 3 and 8 weeks with respect to the PPE administration is shown in Figure 6.10. The T2* shortening in time can be observed in the left lung while in the right lung no specific T2* behaviour was determined. Concerning the left lung, the most prominent T2* changes (30% of T2* decrease) were observed at the later time point (3 and 8 weeks) as compared to the T2* measured prior to PPE administration. Significantly T2* decrease was found between the first day (prior to PPE administration) and 8 weeks following challenge ($p<0.05$).

Similarly to the kinetics of signal intensity, T2* changes between two later time points (3 and 8 weeks) were not significant, showing that emphysema develops quickly after challenge and its progress slows down, afterwards. No specific changes in T2* were detected for the right lung.

6.8.2 Histology

Representative histological images from the left lung are shown in Figure 6.11. Figure 6.11a illustrates the lung parenchyma from the elastase-treated mouse at 8 weeks

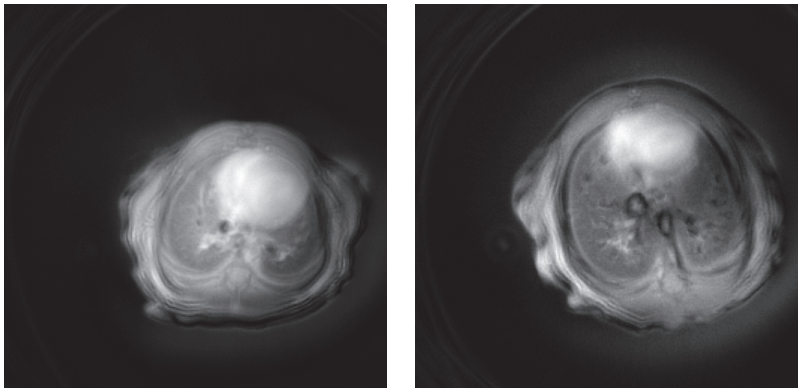

Figure 6.8: Axial images of control (a) and PPE treated mouse (b) at the same age, acquired at 8 weeks after challenge and saline administration. Note that in the expanded lungs (b) the heart is displaced in the direction of the right lung.

after PPE instillation. Note, significant enlargement of the alveolar spaces compared to the control mouse (Figure 6.11b). This enlargement was attributed to the development of emphysema.

Despite the lack of completed

Despite the lack of completed histological analysis for this study, the data from a previous study including the exact experimental protocol were analyzed.

Notably, the previous experiment showed that the airspace enlargement was more pronounced in the left lung compared to the right lung (see Figure 6.12) revealing that the stronger development of emphysema occured in the left lung.

The severity of emphysema was assessed based on the visual observation. For quantitative histological assessement, the score between 0 (without emphysema) and 6 (more than 80 % of emphysema in the lung) was assumed. A higher score (mean: 3.2 ± 1.2 versus 2.1 ± 1.1) assessed for 11 animals was found for the left side of the lung.

6.9 Discussion

In modern research and diagnostics of emphysema, two modalities are currently used to detect its presence, assess its severity and follow its progression. The X-ray attenuation detected by CT is used to assess density of the lungs (74) and HP 3He diffusion-weighted MRI is used to estimate alveolar size (130), (31). Although these techniques correlate

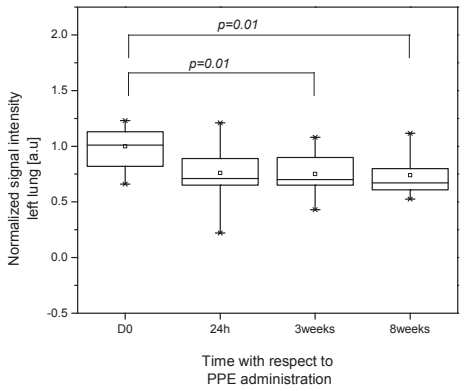

(a)

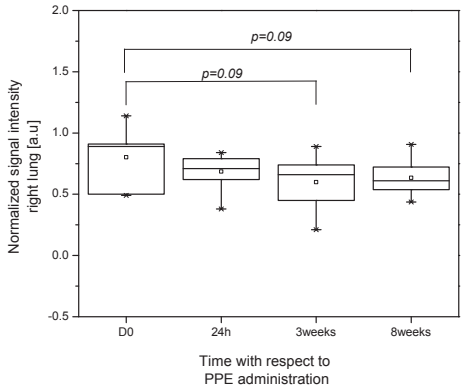

(b)

Figure 6.9: Signal intensities measured from the left (a) and right (b) lung parenchyma with regards to time after administration of PPE. The bottom and top of the box are the lower and upper quartiles, respectively; the band near the middle of the box is the median; the ends of the whiskers represent the minimum and maximum of all the data; the open squares represent the mean.

with morphological analysis by measuring mean linear intercept (Lm), (60), (92), (130), their widespread use both in clinical and pre-clinical research is limited.

A short echo-time offered by UTE MRI technique enables signal detection of the lungs parenchyma. Moreover, by varying the TE of this sequence it is possible to assess the T2*.

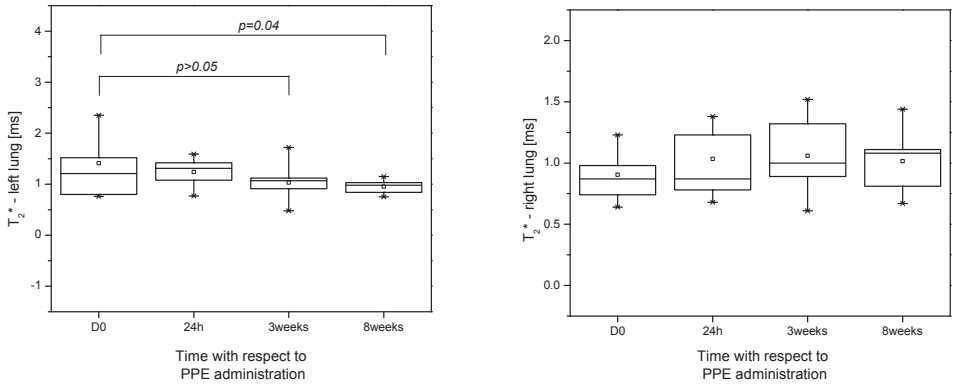

(a) (b)

Figure 6.10: T2* changes measured in the left (a) and right (b) lungs at different time intervals with regards to administration of PPE. The bottom and top of the box are the lower and upper quartiles, respectively; the band near the middle of the box is the median; the ends of the whiskers represent the minimum and maximum of all the data; the open squares represent the mean.

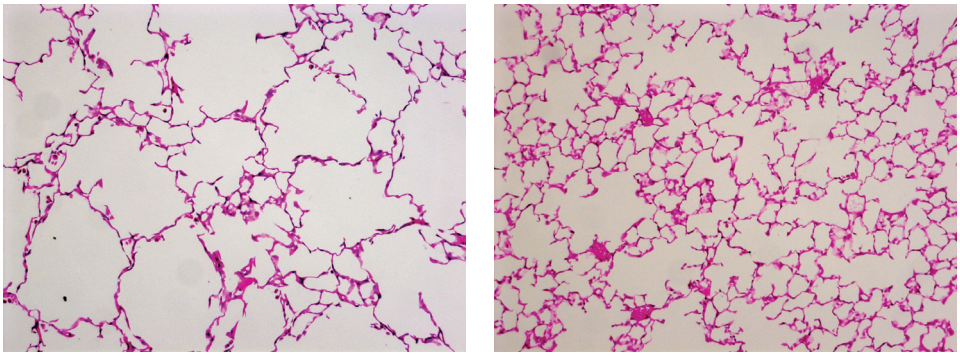

(a) (b)

Figure 6.11: Histological slices of mouse lung from the left lung. The lung tissue 8 weeks after PPE administration (a) and saline administration (b).

Since the signal detected from the parenchyma is weighted by proton tissue density and T2* reflects morphometric changes of the alveolar structure (30), this sequence gives unique opportunities to detect markers of emphysema non-invasively and without the use of any contrast agent. In the present study, the quantification of the kinetics

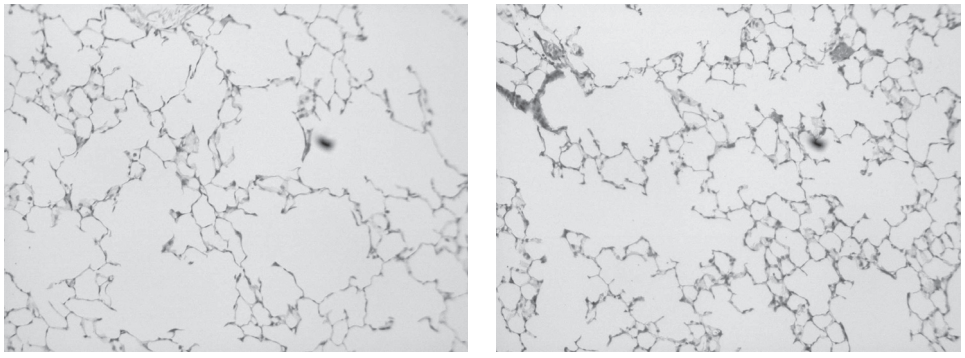

(a) (b)

Figure 6.12: Comparison of histological slices from the left (a) and right (b) lung from mouse treated with PPE.

of murine elastase-induced emphysema model using UTE MR imaging, was performed. The results were compared with histological analysis.

Our study demonstrates that signal intensity and T2* are lower in lungs with emphysema, than those in healthy animals.

The signal decreasing was observed as early as 24 h after elastase administration. At the same time interval, MRI images (see Figure 6.6a) showed presence of fluid signals accompanied by regional significant signal drop. This observation reflects acute inflammatory response caused by elastase administration and it was consistent with previous studies demonstrating that administration of elastase results in formation of inflammation accompanied by hemorrhage (20). Consequently, the results from quantitative measurement concerning the first day after PPE administration were excluded from the statistical significance test to ensure there will be no interference with inflammatory signals.

At 3 weeks, a significant decrease in signal intensity was observed compared with baseline. This result reflects the lower overall pulmonary density and is consistent with previous studies with the use of gradient-echo and SP imaging (99), (87).

During the suffering of emphysema, the alveolar walls are destroyed leading to an increase of gas volume in alveoli, loss of lung elasticity and obliteration of the pulmonary capillary bed. Further consequences are: increased lung volume, air trapping and impairments of gas exchange. The increased pulmonary volume as well as increased air

volume relative to tissue mass, cause local decreasing of tissue density. As a result a reduction of MR signal in the lung parenchyma is observed.

A similar effect showing the dependence of the MR signal and lung density is observed during the physiological conditions of respiration (30),(45). The inhalation phase involves increasing the thoracic volume and airflow into alveoli. This results in lower proton density thus, lower MR signal intensity compared to the exhalation phase, where parenchyma contraction occurs.

With the progression of emphysema across time, no significant signal decrease was observed at 8 weeks compared to those at 3 weeks ($p>0.05$). This showed that more dynamic disease evolution occurs during earlier stages after which a plateau is observed. This observation is consistent with the previous studies involving Lm measurements, which confirms that dynamic disease progression occurs up to 2 weeks after elastase challenge with a peak occurring between 5 and 10 days (72). After that, a slow-down of the disease progression is observed.

Quantitative T2* measurements showed similar characteristics to those observed for signal intensity. The T2* values dropped at 24 h after elastase administration and progressively decreased at later time points of the experiment. This result reflects the fact that emphysematous alveoli are larger, thus resulting in higher internal susceptibility gradients, when compared to healthy animals. A similar effect was found in an excised rat lung inflated to a pressure of 20 cm H2O by Cuttilo (30). Inflated lungs had inhomogeneous line-broadening (equivalent to lower T2* values), that was not found in collapsed lungs.

This observation was confirmed by simulating the susceptibility effect, utilizing the spherical-shell and foam model (28). Simulation including different air ratios showed a higher susceptibility effect with increasing ratios of air (30), (34).

In the physiological conditions the T2* differences between inhalation and exhalation with shorter T2* value observed in inspiration were reported (45).

T2* shortening in the case of inhalation of 100% oxygen were seen in humans (97). In emphysematous lungs, high alveoli inflation and higher level of oxygenation, resulting from air trapping, occurs.

Since lung inflation and higher oxygenation are related one can assume that paramagnetic properties of molecular oxygen and higher susceptibility in inflated lungs would

add and amplify T2* shortening in emphysematous mice compared to the healthy subjects.

The T2* values measured in our experiment ranged between 0.8 - 1.4 ms which are longer than the 4.7-T value in rodents reported, by Olsson and Beckmann (ranging between 0.4 - 0.5 ms). One possible explanation for that includes the use of different imaging sequence parameters. Sequences reported previously had much shorter TR than that used for our study (1.5-5.6 ms versus 80 ms) and thus a stronger T1-weighting. As a result, the relative contribution to MR signal intensity of the different proton comparments (blood, tissue water, etc) associated with given T1 and T2* values is modified. This modification in the contribution of proton components might affect the overall measured T2* values.

Notably, T2* as well as signal intensity reduction was more pronounced in the left lung compared to the right lung. These results were confirmed by histology and they are consistent with previous research, including experimentally induced inflammation (8). A possible explanation of why the left lung shows a stronger response to the elastase challenge relates to the anatomical structure of the tracheobronchial tree. Since the elastase administration was performed by intra-tracheal injection, one could expect that the probability of the solution entering the left and right lung is equal. As the left lung is smaller than the right lung, and only consists of one lobe, there is likely dosage amplification as compared to the right lung (where the solution is distributed into four lobes). The higher probability of affecting the left lung is further strengthened by the fact that its branching starts at a higher level, than the right lung.

6.10 Conclusions

We have shown that the UTE radial technique was successfully applied to detect changes at the alveolar level in elastase-challenged mouse modeling emphysema. Tracking of the disease progression was feasible by a non-enhanced proton MRI using two MR parameters, namely: signal intensity and transverse relaxation time, T2*. The proton signal intensity decrease reflects tissue density reduction and T2* shortening correspond to the increase in the size of the alveoli.

Our imaging protocol was performed without the use of a mechanical ventilator, allowing the mice to breath spontaneously. The motion artifacts were effectively re-

duced thanks to the behavior of radial acquisition in the presence of cardio-respiratory motion (42). As compared to scan-synchronous ventilation approach, used for motion artifacts reduction, this technique is less invasive and enables higher throughput.

The non-invasiveness of the present approach opens the way for its widespread use for routine drug testing in experimental MR lung research as well as its possible transition to clinical studies.

7

Conclusions

In this final section, we discuss the most important issues and contributions of this thesis, as well as ideas for future work.

7.1 Summary of contributions

In this work, ultra-short echo-time (UTE) MR imaging of the lungs is presented as a way of detecting pulmonary MRI signal to develop new imaging tools and to expand MR applications for experimental models of lung diseases in rodents. In particular, this technique was used to detect a large spectrum of pathological indicators associated with pulmonary morphological changes characteristic of Chronic Pulmonary Obstructive Disease (COPD). The morphological characterization of lung tissue was assessed by applying the following steps.

1. Implementation of an image synchronization technique to track cardio-respiratory motions in mice.

   A navigating technique was developed and validated, in order to track respiratory and cardiac motion during the free-breathing respiration of mice, yielding images free from motion artifacts. This was possible to achieve using radial k-space sampling, in which repetitive probing of the k-space center (after each RF excitation) occurs.

   Taking advantage of this interesting feature of UTE radial sampling, we demonstrated the feasibility of tracking the MR signal changes derived from the lung

parenchyma. These signal changes were possible to detect due to a variation of pulmonary density and volume during respiration.

The main asset of the proposed technique is its non-invasiveness. Thus, in view of pharmacological research, the same animal can be used as its own control (measured at the baseline) and it can be monitored repeatedly during the disease's progression without affecting its physiology. This simplifies imaging protocols, increasing throughput, and it enables us to achieve a constant repetition time of the imaging sequence - providing easier control of image contrast and making quantitative image analysis feasible.

2. Application of the UTE MRI technique for reproducible edema detection.

   The intrinsic advantages of radial UTE sampling over Cartesian encoding (with respect to diminished artifacts from cardio-respiratory motion) were used to develop a new approach for investigating inflammation in rat lungs. The identification of inflammatory regions relied on the detection of hyperintense areas in proton MR images caused by edema formation in the lung.

   Considering the fact that the detection of the edema's extent plays an important role in establishing therapeutic responses and the development of new treatment agents, a robust protocol was introduced to improve the reproducible delineation of the edema's extent. The proposed method was shown to increase the reliability of volumetric measurements, compared to currently established methods.

3. Detection of cellular infiltration in the lungs by MRI.

   The extent of the edematous areas frequently leads to the misevaluation of regions of inflammation, thus a new approach used to delineate the extent of inflammation was introduced. In the proposed method, UTE was used to track inflammatory cells in the lungs following the induction of inflammation.

   The detection of inflammatory regions was possible by tracking magnetically labeled macrophages (labeled with IONPs particles) due to susceptibility effects in MR imaging. Since the susceptibility effects were detectable as early as six hours after the induction of inflammation, we have shown that this technique can be useful for the early diagnosis of diseases.

Specifically, we have shown the utility of cellular tracking to define early inflammatory activities in chronic inflammation, modeling COPD in humans. The proposed experimental approach could potentially be transferred to clinical studies.

4. Non-invasive and non-enhanced MRI detection of emphysema in a murine model.

   The UTE technique was demonstrated to detect the markers of emphysema and characterize emphysema progression with respect to time. MRI indicators of emphysematous tissue were established and they correlated well with alveolar expansion, demonstrated by histology.

   The main advantage of the proposed technique over currently established methods (ie. based on histological analysis and CT), is its non-invasiveness. This allows repeated measurements on the same animal to be performed over time, without interfering with the animal's physiology.

In summary, the UTE proton MRI was shown to provide insight into pathological indicators like inflammation and airspace enlargement associated with major lung diseases such as COPD. Relevant structural and functional information concerning the lungs was obtained thanks to the MR signal from lung parenchyma. This technique was shown to be useful when easy protocol implementation (relatively high throughput and low-cost experiments) and longitudinal studies (limited interference with subject's physiopathology) are of concern.

7.2 Future research

Some ideas and issues for possible line of future research are discussed below:

1. Sequence development: To ameliorate image quality, the prospect of implementing the projection order based on "golden ratio" ordering is appealing. The advantages of such k-space ordering are twofold. First, it would diminish residual streaking by reducing inter-projection inconsistencies during motion. Second, as it allows for significant under-sampling of k-space without reducing image quality, it yields a reduced acquisition time and therefore improves protocol efficiency.

2. Improvement of a temporal resolution for self-gating reconstruction: section 4 shows the results of self-gating reconstruction with image synchronization to the

defined phase of the cardio-respiratory cycle. The synchronization should be performed ideally to multiple phases of the cardio-respiratory cycle, yielding a CINE reconstruction of the cardio-respiratory cycle. To achieve this goal, a four-fold or higher reduction in temporal resolution is required. The CINE reconstruction is expected to provide information related to perfusion and ventilation. Subsequently, signal loss can be recovered by averaging across many k-spaces.

3. Appropriate dosing of the contrast agent: section 5 illustrates detection of the infiltration of macrophages into the lung. In order to maximize the labeling of inflammatory macrophages in the lung, it is important to correctly choose the time interval and appropriate dosing of the contrast agent. Subsequently, the distribution of the labeled-macrophages in the body should be assessed quantitatively.

4. General research perspectives: There is great interest in investigating the relationship between anatomical and functional changes in lung disorders. For instance, proton lung MRI combined with ventilation imaging using hyperpolarized gases was explored in order to examine the correlations between the lesion areas detected by proton MRI and the observed ventilations defects (88). To assess regional pulmonary ventilation, oxygen-enhanced MRI is the technique of choice (36), (23). This method offers quantitative estimation of regional ventilation of lung parenchyma (3). Recently, the oxygen-enhanced technique was applied to the diagnostics and evaluation of a variety of pulmonary disorders in humans; including pulmonary emphysema, diffuse lung disease (including pulmonary fibrosis), embolism, and pneumonia (112), (113). More recently, Watt et al. demonstrated the feasibility of oxygen-enhanced imaging in mice (125). In previous studies, inversion recovery spin-echo sequences have been used to quantify ventilation changes. The spatial resolutions of images were, however, limited due to the low signal from the lungs and time constraints. To improve image quality, we propose to use radial UTE acquisition conjugated with golden-ratio projection distribution. This new MR ventilation imaging technique may give an insight into pulmonary physiology, as well as pathopysiology, in many pulmonary diseases including emphysema, fibrosis and pulmonary embolisms.

References

[1] S. M. Albelda, C. W. Smith, and P. A. Ward. Adhesion molecules and inflammatory injury. *FASEB J*, 8(8):504–512, May 1994. 69

[2] J. D. Armstrong, E. H. Gluck, R. O. Crapo, H. A. Jones, and J. M. Hughes. Lung tissue volume estimated by simultaneous radiographic and helium dilution methods. *Thorax*, 37(9):676–679, Sep 1982. 14

[3] Johannes F T Arnold, Markus Kotas, Florian Fidler, Eberhard D Pracht, Michael Flentje, and Peter M Jakob. Quantitative regional oxygen transfer imaging of the human lung. *J Magn Reson Imaging*, 26(3):637–645, Sep 2007. 120

[4] O. S. Atwal, K. J. Minhas, and C. S. Williams. Ultrastructural response of pulmonary intravascular macrophages to exogenous oestrogen in the bovine lung: translocation of the surface-coat and enhanced cell membrane plasticity and angiogenesis. *J Anat*, 198(Pt 5):611–624, May 2001. 12

[5] Robin Azoulay, Paul Olivier, Olivier Baud, Catherine Verney, Robin Santus, Philippe Robert, Pierre Gressens, and Guy Sebag. Uspio (ferumoxtran-10)-enhanced mri to visualize reticuloendothelial system cells in neonatal rats: feasibility and biodistribution study. *J Magn Reson Imaging*, 28(4):1046–1052, Oct 2008. 76

[6] Alexander A Bankier, Carl R O'Donnell, Vu M Mai, Pippa Storey, Viviane De Maertelaer, Robert R Edelman, and Qun Chen. Impact of lung volume on mr signal intensity changes of the lung parenchyma. *J Magn Reson Imaging*, 20(6):961–966, Dec 2004. 15

[7] Grzegorz Bauman, Michael Puderbach, Michael Deimling, Vladimir Jellus, Christophe Chefd'hotel, Julien Dinkel, Christian Hintze, Hans-Ulrich Kauczor, and Lothar R Schad. Non-contrast-enhanced perfusion and ventilation assessment of the human lung by means of fourier decomposition in proton mri. *Magn Reson Med*, 62(3):656–664, Sep 2009. 15

[8] N. Beckmann, B. Tigani, D. Ekatodramis, R. Borer, L. Mazzoni, and J. R. Fozard. Pulmonary edema induced by allergen challenge in the rat: noninvasive assessment by magnetic resonance imaging. *Magn Reson Med*, 45(1):88–95, Jan 2001. 27, 28, 61, 82, 93, 115

[9] N. Beckmann, B. Tigani, L. Mazzoni, and J. R. Fozard. Mri of lung parenchyma in rats and mice using a gradient-echo sequence. *NMR Biomed*, 14(5):297–306, Aug 2001. 15, 42, 61, 71

[10] Nicolau Beckmann, Catherine Cannet, Anna Louise Babin, François-Xavier Blé, Stefan Zurbruegg, Rainer Kneuer, and Vincent Dousset. In vivo visualization of macrophage infiltration and activity in inflammation using magnetic resonance imaging. *Wiley Interdiscip Rev Nanomed Nanobiotechnol*, 1(3):272–298, May 2009. 72

[11] Nicolau Beckmann, Catherine Cannet, Harry Karmouty-Quintana, Bruno Tigani, Stefan Zurbruegg, François-Xavier Blé, Yannick Crémillieux, and Alexandre Trifilieff. Lung mri for experimental drug research. *Eur J Radiol*, 64(3):381–396, Dec 2007. 3, 69, 71

[12] Nicolau Beckmann, Catherine Cannet, Stefan Zurbruegg, Markus Rudin, and Bruno Tigani. Proton mri of lung parenchyma reflects allergen-induced airway remodeling and endotoxin-aroused hyporesponsiveness: a step toward ventilation studies in spontaneously breathing rats. *Magn Reson Med*, 52(2):258–268, Aug 2004. 71, 82

[13] Nicolau Beckmann, Regina Falk, Stefan Zurbrügg, Janet Dawson, and Petra Engelhardt. Macrophage infiltration into the rat knee detected by mri in a model of antigen-induced arthritis. *Magn Reson Med*, 49(6):1047–1055, Jun 2003. 72

[14] Nicolau Beckmann, Bruno Tigani, Rosemary Sugar, Alan D Jackson, Gareth Jones, Lazzaro Mazzoni, and John R Fozard. Noninvasive detection of endotoxin-induced mucus hypersecretion in rat lung by mri. *Am J Physiol Lung Cell Mol Physiol*, 283(1):L22–L30, Jul 2002. 3, 71, 79, 82, 93

[15] C. J. Bergin, D. C. Noll, J. M. Pauly, G. H. Glover, and A. Macovski. Mr imaging of lung parenchyma: a solution to susceptibility. *Radiology*, 183(3):673–676, Jun 1992. 22

[16] J. Bieth, B. Spiess, and C. G. Wermuth. The synthesis and analytical use of a highly sensitive and convenient substrate of elastase. *Biochem Med*, 11(4):350–357, Dec 1974. 101

[17] J. D. Brain, R. M. Molina, M. M. DeCamp, and A. E. Warner. Pulmonary intravascular macrophages: their contribution to the mononuclear phagocyte system in 13 species. *Am J Physiol*, 276(1 Pt 1):L146–L154, Jan 1999. 12

[18] Anja C S Brau, Laurence W Hedlund, and G. Allan Johnson. Cine magnetic resonance microscopy of the rat heart using cardiorespiratory-synchronous projection reconstruction. *J Magn Reson Imaging*, 20(1):31–38, Jul 2004. 3, 16, 42

[19] J-C. Brisset, V. Desestret, S. Marcellino, E. Devillard, F. Chauveau, F. Lagarde, S. Nataf, N. Nighoghossian, Y. Berthezene, and M. Wiart. Quantitative effects of cell internalization of two types of ultrasmall superparamagnetic iron oxide nanoparticles at 4.7 t and 7 t. *Eur Radiol*, 20(2):275–285, Feb 2010. 77

[20] R. H. Busch, K. E. Lauhala, S. M. Loscutoff, and K. E. McDonald. Experimental pulmonary emphysema induced in the rat by intratracheally administered elastase: morphogenesis. *Environ Res*, 33(2):497–513, Apr 1984. 101, 107, 113

REFERENCES

[21] Brendan J Canning. Modeling asthma and copd in animals: a pointless exercise? *Curr Opin Pharmacol*, 3(3):244–250, Jun 2003. 68

[22] Ben T Chen, Alexander T Yordanov, and G. Allan Johnson. Ventilation-synchronous magnetic resonance microscopy of pulmonary structure and ventilation in mice. *Magn Reson Med*, 53(1):69–75, Jan 2005. 42

[23] Q. Chen, P. M. Jakob, M. A. Griswold, D. L. Levin, H. Hatabu, and R. R. Edelman. Oxygen enhanced mr ventilation imaging of the lung. *MAGMA*, 7(3):153–161, Dec 1998. 120

[24] X. J. Chen, L. W. Hedlund, H. E. Möller, M. S. Chawla, R. R. Maronpot, and G. A. Johnson. Detection of emphysema in rat lungs by using magnetic resonance measurements of 3he diffusion. *Proc Natl Acad Sci U S A*, 97(21):11478–11481, Oct 2000. 98, 101

[25] C. G. Chitko-McKown and F. Blecha. Pulmonary intravascular macrophages: a review of immune properties and functions. *Ann Rech Vet*, 23(3):201–214, 1992. 12

[26] Claire Corot, Philippe Robert, Jean-Marc Idée, and Marc Port. Recent advances in iron oxide nanocrystal technology for medical imaging. *Adv Drug Deliv Rev*, 58(14):1471–1504, Dec 2006. 72, 75, 77

[27] Y. Crémillieux, A. Briguet, and A. Deguin. Projection-reconstruction methods: fast imaging sequences and data processing. *Magn Reson Med*, 32(1):23–32, Jul 1994. 38

[28] A. G. Cutillo and D. C. Ailion. Modeling the nuclear magnetic resonance behavior of lung: from electrical engineering to critical care medicine. *Bioelectromagnetics*, Suppl 4:110–119, 1999. 114

[29] A. G. Cutillo, P. H. Chan, D. C. Ailion, S. Watanabe, K. H. Albertine, C. H. Durney, C. B. Hansen, G. Laicher, R. F. Scheel, and A. H. Morris. Effects of endotoxin lung injury on nmr t2 relaxation. *Magn Reson Med*, 39(2):190–197, Feb 1998. 70

[30] A. G. Cutillo, K. Ganesan, D. C. Ailion, A. H. Morris, C. H. Durney, S. C. Symko, and R. A. Christman. Alveolar air-tissue interface and nuclear magnetic resonance behavior of lung. *J Appl Physiol*, 70(5):2145–2154, May 1991. 15, 112, 114

[31] Sandra Diaz, Ingrid Casselbrant, Eeva Piitulainen, Peter Magnusson, Barry Peterson, Per Wollmer, Peter Leander, Olle Ekberg, and Per Akeson. Validity of apparent diffusion coefficient hyperpolarized 3he-mri using msct and pulmonary function tests as references. *Eur J Radiol*, 71(2):257–263, Aug 2009. 100, 110

[32] Jiang Du, Atsushi M Takahashi, Won C Bae, Christine B Chung, and Graeme M Bydder. Dual inversion recovery, ultrashort echo time (dir ute) imaging: creating high contrast for short-t(2) species. *Magn Reson Med*, 63(2):447–455, Feb 2010. 24

[33] Joseph P Dugas, Joel R Garbow, Dale K Kobayashi, and Mark S Conradi. Hyperpolarized (3)he mri of mouse lung. *Magn Reson Med*, 52(6):1310–1317, Dec 2004. 101

[34] C. H. Durney, A. G. Cutillo, and D. C. Ailion. Magnetic resonance behavior of normal and diseased lungs: spherical shell model simulations. *J Appl Physiol*, 88(4):1155–1166, Apr 2000. 15, 114

[35] Bernd Ebner, Patrick Behm, Christoph Jacoby, Sandra Burghoff, Brent A French, Jürgen Schrader, and Ulrich Flögel. Early assessment of pulmonary inflammation by 19f mri in vivo. *Circ Cardiovasc Imaging*, 3(2):202–210, Mar 2010. 71

[36] R. R. Edelman, H. Hatabu, E. Tadamura, W. Li, and P. V. Prasad. Noninvasive assessment of regional ventilation in the human lung using oxygen-enhanced magnetic resonance imaging. *Nat Med*, 2(11):1236–1239, Nov 1996. 120

[37] D. H. Eidelman, S. Bellofiore, D. Chiche, M. G. Cosio, and J. G. Martin. Behavior of morphometric indices in pancreatic elastase-induced emphysema in rats. *Lung*, 168(3):159–169, 1990. 101

[38] Heinz Fehrenbach. Commentaries on viewpoint: use of mean airspace chord length to assess emphysema. what does lm tell us about lung pathology? *J Appl Physiol*, 105(6):1984–5; author reply 1986–7, Dec 2008. 101

[39] S. L. Gewalt, G. H. Glover, L. W. Hedlund, G. P. Cofer, J. R. MacFall, and G. A. Johnson. Mr microscopy of the rat lung using projection reconstruction. *Magn Reson Med*, 29(1):99–106, Jan 1993. 22, 42, 61

[40] Sukhjit S Gill, Sarabjeet S Suri, Kyathanahalli S Janardhan, Sarah Caldwell, Tanya Duke, and Baljit Singh. Role of pulmonary intravascular macrophages in endotoxin-induced lung inflammation and mortality in a rat model. *Respir Res*, 9:69, 2008. 12

[41] O. M. Girard, J. Du, L. Agemy, K. N. Sugahara, V. R. Kotamraju, E. Ruoslahti, G. M. Bydder, and R. F. Mattrey. Optimization of iron oxide nanoparticle detection using ultrashort echo time pulse sequences: comparison of t1, t2*, and synergistic t1- t2* contrast mechanisms. *Magn Reson Med*, 65(6):1649–1660, Jun 2011. 77

[42] G. H. Glover and J. M. Pauly. Projection reconstruction techniques for reduction of motion effects in mri. *Magn Reson Med*, 28(2):275–289, Dec 1992. 27, 42, 116

[43] Ian A Greaves. Commentaries on viewpoint: use of mean airspace chord length to assess emphysema. mean airspace chord length is useful in assessing emphysema. *J Appl Physiol*, 105(6):1982; author reply 1986–1982; author reply 1987, Dec 2008. 101

[44] J. R. Harkema and J. A. Hotchkiss. In vivo effects of endotoxin on intraepithelial mucosubstances in rat pulmonary airways. quantitative histochemistry. *Am J Pathol*, 141(2):307–317, Aug 1992. 69

[45] H. Hatabu, D. C. Alsop, J. Listerud, M. Bonnet, and W. B. Gefter. T2* and proton density measurement of normal human lung parenchyma using submillisecond echo time gradient echo magnetic resonance imaging. *Eur J Radiol*, 29(3):245–252, Mar 1999. 14, 114

[46] H. Hatabu, Q. Chen, K. W. Stock, W. B. Gefter, and H. Itoh. Fast magnetic resonance imaging of the lung. *Eur J Radiol*, 29(2):114–132, Feb 1999. 16

[47] L. W. Hedlund, G. P. Cofer, S. J. Owen, and G. Allan Johnson. Mr-compatible ventilator for small animals: computer-controlled ventilation for proton and noble gas imaging. *Magn Reson Imaging*, 18(6):753–759, Jul 2000. 3, 17, 42

[48] Bassem Hiba, Nathalie Richard, Marc Janier, and Pierre Croisille. Cardiac and respiratory double self-gated cine mri in the mouse at 7 t. *Magn Reson Med*, 55(3):506–513, Mar 2006. 43, 62, 64

[49] Bassem Hiba, Nathalie Richard, Hélène Thibault, and Marc Janier. Cardiac and respiratory self-gated cine mri in the mouse: comparison between radial and rectilinear techniques at 7t. *Magn Reson Med*, 58(4):745–753, Oct 2007. 43

[50] S. Hurd. The impact of copd on lung health worldwide: epidemiology and incidence. *Chest*, 117(2 Suppl):1S–4S, Feb 2000. 1

[51] Satoru Ito, Edward P Ingenito, Stephen P Arold, Harikrishnan Parameswaran, Nora T Tgavalekos, Kenneth R Lutchen, and Béla Suki. Tissue heterogeneity in the mouse lung: effects of elastase treatment. *J Appl Physiol*, 97(1):204–212, Jul 2004. 101

[52] J. I. Jackson, C. H. Meyer, D. G. Nishimura, and A. Macovski. Selection of a convolution function for fourier inversion using gridding [computerised tomography application]. *IEEE Trans Med Imaging*, 10(3):473–478, 1991. 26, 27, 48

[53] Richard E Jacob, Brett G Amidan, Jolen Soelberg, and Kevin R Minard. In vivo mri of altered proton signal intensity and t2 relaxation in a bleomycin model of pulmonary inflammation and fibrosis. *J Magn Reson Imaging*, 31(5):1091–1099, May 2010. 102

[54] G. A. Johnson, G. P. Cofer, L. W. Hedlund, R. R. Maronpot, and S. A. Suddarth. Registered (1)h and (3)he magnetic resonance microscopy of the lung. *Magn Reson Med*, 45(3):365–370, Mar 2001. 42, 61

[55] Achim H Kaim, Thorsten Wischer, Terence O'Reilly, Gernot Jundt, Johannes Fröhlich, Gustav K von Schulthess, and Peter R Allegrini. Mr imaging with ultrasmall superparamagnetic iron oxide particles in experimental soft-tissue infections in rats. *Radiology*, 225(3):808–814, Dec 2002. 72

[56] H. Karmouty-Quintana, F-X. Blé, C. Cannet, S. Zurbruegg, J. R. Fozard, C. P. Page, and N. Beckmann. In vivo pharmacological evaluation of compound 48/80-induced airways oedema by mri. *Br J Pharmacol*, 154(5):1063–1072, Jul 2008. 61

[57] H. Karmouty-Quintana, C. Cannet, R. Sugar, J. R. Fozard, C. P. Page, and N. Beckmann. Capsaicin-induced mucus secretion in rat airways assessed in vivo and non-invasively by magnetic resonance imaging. *Br J Pharmacol*, 150(8):1022–1030, Apr 2007. 61

[58] Harry Karmouty-Quintana, Catherine Cannet, Stefan Zurbruegg, François-Xavier Blé, John R Fozard, Clive P Page, and Nicolau Beckmann. Bleomycin-induced lung injury assessed noninvasively and in spontaneously breathing rats by proton mri. *J Magn Reson Imaging*, 26(4):941–949, Oct 2007. 3

[59] Waheedullah Karzai, Xizhong Cui, Norbert Heinicke, Christian Niemann, Eric P Gerstenberger, Rosaly Correa, Steven Banks, Bjoern Mehlhorn, Frank Bloos, Konrad Reinhart, and Peter Q Eichacker. Neutrophil stimulation with granulocyte colony-stimulating factor worsens ventilator-induced lung injury and mortality in rats. *Anesthesiology*, 103(5):996–1005, Nov 2005. 3, 18

[60] Masaki Kawakami, Yukiko Matsuo, Kenta Yoshiura, Takahide Nagase, and Naomi Yamashita. Sequential and quantitative analysis of a murine model of elastase-induced emphysema. *Biol Pharm Bull*, 31(7):1434–1438, Jul 2008. 101, 111

[61] R. Kikinis, M. E. Shenton, G. Gerig, J. Martin, M. Anderson, D. Metcalf, C. R. Guttmann, R. W. McCarley, W. Lorensen, and H. Cline. Routine quantitative analysis of brain and cerebrospinal fluid spaces with mr imaging. *J Magn Reson Imaging*, 2(6):619–629, 1992. 83, 92

[62] Birgit Kittel, Christine Ruehl-Fehlert, Gerd Morawietz, Jan Klapwijk, Michael R Elwell, Barbara Lenz, M. Gerard O'Sullivan, Daniel R Roth, Peter F Wadsworth, R. I. T. A. Group, and N. A. C. A. D. Group. Revised guides for organ sampling and trimming in rats and mice–part 2. a joint publication of the rita and nacad groups. *Exp Toxicol Pathol*, 55(6):413–431, Jul 2004. 7

[63] Dean O Kuethe, Natalie L Adolphi, and Eiichi Fukushima. Short data-acquisition times improve projection images of lung tissue. *Magn Reson Med*, 57(6):1058–1064, Jun 2007. 61

[64] N. R. Labiris, C. Nahmias, A. P. Freitag, M. L. Thompson, and M. B. Dolovich. Uptake of 18fluorodeoxyglucose in the cystic fibrosis lung: a measure of lung inflammation? *Eur Respir J*, 21(5):848–854, May 2003. 70

[65] C. M. Lai and P. C. Lauterbur. True three-dimensional image reconstruction by nuclear magnetic resonance zeugmatography. *Phys Med Biol*, 26(5):851–856, Sep 1981. 27

[66] Andrew C Larson, Peter Kellman, Andrew Arai, Glenn A Hirsch, Elliot McVeigh, Debiao Li, and Orlando P Simonetti. Preliminary investigation of respiratory self-gating for free-breathing segmented cine mri. *Magn Reson Med*, 53(1):159–168, Jan 2005. 43, 51

[67] Andrew C Larson, Richard D White, Gerhard Laub, Elliot R McVeigh, Debiao Li, and Orlando P Simonetti. Self-gated cardiac cine mri. *Magn Reson Med*, 51(1):93–102, Jan 2004. 43, 44, 62

[68] P. C. Lauterbur. Image formation by induced local interactions. examples employing nuclear magnetic resonance. 1973. *Clin Orthop Relat Res*, (244):3–6, Jul 1989. 21

[69] Ji-Hyun Lee, Dong-Soon Lee, Eun-Kyung Kim, Kang-Hyeon Choe, Yeon-Mock Oh, Tae-Sun Shim, Sang-Eun Kim, Yun-Song Lee, and Sang-Do Lee. Simvastatin inhibits cigarette smoking-induced emphysema and pulmonary hypertension in rat lungs. *Am J Respir Crit Care Med*, 172(8):987–993, Oct 2005. 68

[70] Wei Lin and Hee Kwon Song. Improved signal spoiling in fast radial gradient-echo imaging: Applied to accurate t(1) mapping and flip angle correction. *Magn Reson Med*, 62(5):1185–1194, Nov 2009. 38

REFERENCES

[71] K. E. Longworth. The comparative biology of pulmonary intravascular macrophages. *Front Biosci*, 2:d232–d241, 1997. 12

[72] Edgar C Lucey, Joseph Keane, Ping-Ping Kuang, Gordon L Snider, and Ronald H Goldstein. Severity of elastase-induced emphysema is decreased in tumor necrosis factor-alpha and interleukin-1beta receptor-deficient mice. *Lab Invest*, 82(1):79–85, Jan 2002. 114

[73] A. E. Lujan, E. W. Larsen, J. M. Balter, and R. K. Ten Haken. A method for incorporating organ motion due to breathing into 3d dose calculations. *Med Phys*, 26(5):715–720, May 1999. 10

[74] A. Madani, C. Keyzer, and P. A. Gevenois. Quantitative computed tomography assessment of lung structure and function in pulmonary emphysema. *Eur Respir J*, 18(4):720–730, Oct 2001. 110

[75] A. Maeda, K. Sano, and T. Yokoyama. Reconstruction by weighted correlation for mri with time-varying gradients. *IEEE Trans Med Imaging*, 7(1):26–31, 1988. 25

[76] Toshitaka Maeno, A. McGarry Houghton, Pablo A Quintero, Sandra Grumelli, Caroline A Owen, and Steven D Shapiro. Cd8+ t cells are required for inflammation and destruction in cigarette smoke-induced emphysema in mice. *J Immunol*, 178(12):8090–8096, Jun 2007. 68

[77] James G Martin and Meiyo Tamaoka. Rat models of asthma and chronic obstructive lung disease. *Pulm Pharmacol Ther*, 19(6):377–385, 2006. 68

[78] Pasquina Marzola, Anna Lanzoni, Elena Nicolato, Vincenza Di Modugno, Patrizia Cristofori, Francesco Osculati, and Andrea Sbarbati. (1)h mri of pneumococcal pneumonia in a murine model. *J Magn Reson Imaging*, 22(1):170–174, Jul 2005. 3

[79] Jaime F Mata, Talissa A Altes, Jing Cai, Kai Ruppert, Wayne Mitzner, Klaus D Hagspiel, Bina Patel, Michael Salerno, James R Brookeman, Eduard E de Lange, William A Tobias, Hsuan-Tsung J Wang, Gordon D Cates, and John P Mugler. Evaluation of emphysema severity and progression in a rabbit model: comparison of hyperpolarized 3he and 129xe diffusion mri with lung morphometry. *J Appl Physiol*, 102(3):1273–1280, Mar 2007. 101

[80] C. H. Meyer, B. S. Hu, D. G. Nishimura, and A. Macovski. Fast spiral coronary artery imaging. *Magn Reson Med*, 28(2):202–213, Dec 1992. 26

[81] Nobuaki Mizutani, Jun ichi Fuchikami, Maki Takahashi, Takeshi Nabe, Shin Yoshino, and Shigekatsu Kohno. Pulmonary emphysema induced by cigarette smoke solution and lipopolysaccharide in guinea pigs. *Biol Pharm Bull*, 32(9):1559–1564, Sep 2009. 68

[82] H. T. Nielsen, G. E. Gold, E. W. Olcott, J. M. Pauly, and D. G. Nishimura. Ultra-short echo-time 2d time-of-flight mr angiography using a half-pulse excitation. *Magn Reson Med*, 41(3):591–599, Mar 1999. 24

[83] D. G. Nishimura, A. Macovski, J. I. Jackson, R. S. Hu, C. A. Stevick, and L. Axel. Magnetic resonance angiography by selective inversion recovery using a compact gradient echo sequence. *Magn Reson Med*, 8(1):96–103, Sep 1988. 24

[84] P. M. O'byrne and D. S. Postma. The many faces of airway inflammation. asthma and chronic obstructive pulmonary disease. asthma research group. *Am J Respir Crit Care Med*, 159(5 Pt 2):S41–S63, May 1999. 107

[85] Matthias Ochs. A brief update on lung stereology. *J Microsc*, 222(Pt 3):188–200, Jun 2006. 101

[86] Markus Oechsner, Eberhard D Pracht, Daniel Staeb, Johannes F T Arnold, Herbert Köstler, Dietbert Hahn, Meinrad Beer, and Peter M Jakob. Lung imaging under free-breathing conditions. *Magn Reson Med*, 61(3):723–727, Mar 2009. 62

[87] Lars E Olsson, Maria Lindahl, Per-Ola Onnervik, Lars B Johansson, Malin Palmér, Martina Kvist Reimer, Leif Hultin, and Paul D Hockings. Measurement of mr signal and t2* in lung to characterize a tight skin mouse model of emphysema using single-point imaging. *J Magn Reson Imaging*, 25(3):488–494, Mar 2007. 102, 113

[88] Lars E Olsson, Amir Smailagic, Per-Ola Onnervik, Anders Lindén, and Paul D Hockings. 1h and hyperpolarized 3he magnetic resonance imaging clearly detect the preventative effect of a glucocorticoid on endotoxin-induced pulmonary inflammation in vivo. *Innate Immun*, Feb 2010. 79, 120

[89] J. D. O'Sullivan. A fast sinc function gridding algorithm for fourier inversion in computer tomography. *IEEE Trans Med Imaging*, 4(4):200–207, 1985. 27

[90] Harikrishnan Parameswaran, Arnab Majumdar, Satoru Ito, Adriano M Alencar, and Béla Suki. Quantitative characterization of airspace enlargement in emphysema. *J Appl Physiol*, 100(1):186–193, Jan 2006. 101

[91] James C Parker and Mary I Townsley. Evaluation of lung injury in rats and mice. *Am J Physiol Lung Cell Mol Physiol*, 286(2):L231–L246, Feb 2004. 2, 69

[92] G. Peces-Barba, J. Ruiz-Cabello, Y. Cremillieux, I. Rodríguez, D. Dupuich, V. Callot, M. Ortega, M. L. Rubio Arbo, M. Cortijo, and N. Gonzalez-Mangado. Helium-3 mri diffusion coefficient: correlation to morphometry in a model of mild emphysema. *Eur Respir J*, 22(1):14–19, Jul 2003. 101, 111

[93] Dana C Peters, J. Andrew Derbyshire, and Elliot R McVeigh. Centering the projection reconstruction trajectory: reducing gradient delay errors. *Magn Reson Med*, 50(1):1–6, Jul 2003. 64

[94] Klaus G Petry, Claudine Boiziau, Vincent Dousset, and Bruno Brochet. Magnetic resonance imaging of human brain macrophage infiltration. *Neurotherapeutics*, 4(3):434–442, Jul 2007. 72

[95] J. G. Pipe. Motion correction with propeller mri: application to head motion and free-breathing cardiac imaging. *Magn Reson Med*, 42(5):963–969, Nov 1999. 17

[96] Laurent Plantier, Sylvain Marchand-Adam, Joëlle Marchal-Sommé, Guy Lesèche, Michel Fournier, Monique Dehoux, Michel Aubier, and Bruno Crestani. Defect of hepatocyte growth factor production by fibroblasts in human pulmonary emphysema. *Am J Physiol Lung Cell Mol Physiol*, 288(4):L641–L647, Apr 2005. 104, 107

[97] Eberhard D Pracht, Johannes F T Arnold, Tungte Wang, and Peter M Jakob. Oxygen-enhanced proton imaging of the human lung using t2. *Magn Reson Med*, 53(5):1193–1196, May 2005. 114

[98] Harry Karmouty Quintana, Catherine Cannet, Elisabeth Schaeublin, Stefan Zurbruegg, Rosemary Sugar, Lazzaro Mazzoni, Clive P Page, John R Fozard, and Nicolau Beckmann. Identification with mri of the pleura as a major site of the acute inflammatory effects induced by ovalbumin and endotoxin challenge in the airways of the rat. *Am J Physiol Lung Cell Mol Physiol*, 291(4):L651–L657, Oct 2006. 71, 79, 84, 93

[99] Harry Karmouty Quintana, Catherine Cannet, Stefan Zurbruegg, François-Xavier Blé, John R Fozard, Clive P Page, and Nicolau Beckmann. Proton mri as a noninvasive tool to assess elastase-induced lung damage in spontaneously breathing rats. *Magn Reson Med*, 56(6):1242–1250, Dec 2006. 3, 107, 113

[100] V. Rasche, R. Proksa, R. Sinkus, P. Börnert, and H. Eggers. Resampling of data between arbitrary grids using convolution interpolation. *IEEE Trans Med Imaging*, 18(5):385–392, May 1999. 26

[101] M. Rudin, N. Beckmann, R. Porszasz, T. Reese, D. Bochelen, and A. Sauter. In vivo magnetic resonance methods in pharmaceutical research: current status and perspectives. *NMR Biomed*, 12(2):69–97, Apr 1999. 2

[102] K. Ruppert, J. R. Brookeman, K. D. Hagspiel, and J. P. Mugler. Probing lung physiology with xenon polarization transfer contrast (xtc). *Magn Reson Med*, 44(3):349–357, Sep 2000. 101

[103] B. T. Saam, D. A. Yablonskiy, V. D. Kodibagkar, J. C. Leawoods, D. S. Gierada, J. D. Cooper, S. S. Lefrak, and M. S. Conradi. Mr imaging of diffusion of (3)he gas in healthy and diseased lungs. *Magn Reson Med*, 44(2):174–179, Aug 2000. 98, 101

[104] S. A. Schmitz. [iron-oxide-enhanced mr imaging of inflammatory atherosclerotic lesions: overview of experimental and initial clinical results]. *Rofo*, 175(4):469–476, Apr 2003. 72

[105] William P Segars, Benjamin M W Tsui, Eric C Frey, G. Allan Johnson, and Stuart S Berr. Development of a 4-d digital mouse phantom for molecular imaging research. *Mol Imaging Biol*, 6(3):149–159, 2004. 10, 12

[106] S. D. Shapiro. Animal models for copd. *Chest*, 117(5 Suppl 1):223S–227S, May 2000. 68

[107] M. D. Shattuck, S. L. Gewalt, G. H. Glover, L. W. Hedlund, and G. A. Johnson. Mr microimaging of the lung using volume projection encoding. *Magn Reson Med*, 38(6):938–942, Dec 1997. 37

[108] S. M. Shea, R. M. Kroeker, V. Deshpande, G. Laub, J. Zheng, J. P. Finn, and D. Li. Coronary artery imaging: 3d segmented k-space data acquisition with multiple breath-holds and real-time slab following. *J Magn Reson Imaging*, 13(2):301–307, Feb 2001. 51

[109] Y. I. Sheline, P. W. Wang, M. H. Gado, J. G. Csernansky, and M. W. Vannier. Hippocampal atrophy in recurrent major depression. *Proc Natl Acad Sci U S A*, 93(9):3908–3913, Apr 1996. 84

[110] S. Shioya, R. Christman, D. C. Ailion, A. G. Cutillo, and K. C. Goodrich. Nuclear magnetic resonance hahn spin-echo decay (t2) in live rats with endotoxin lung injury. *Magn Reson Med*, 29(4):441–445, Apr 1993. 70

[111] G. L. Snider, E. C. Lucey, and P. J. Stone. Animal models of emphysema. *Am Rev Respir Dis*, 133(1):149–169, Jan 1986. 97

[112] A. Stadler, L. Stiebellehner, P. M. Jakob, J. F T Arnold, and A. A. Bankier. [t1 maps and o2-enhanced mrt of the diseased lung. emphysema, fibrosis, mucoviscidosis]. *Radiologe*, 46(4):282, 284–282, 289, Apr 2006. 120

[113] Alfred Stadler, Leopold Stiebellehner, Peter M Jakob, Johannes F T Arnold, Edith Eisenhuber, Isabella von Katzler, and Alexander A Bankier. Quantitative and o(2) enhanced mri of the pathologic lung: findings in emphysema, fibrosis, and cystic fibrosis. *Int J Biomed Imaging*, 2007:23624, 2007. 120

[114] N. C. Staub. Pulmonary intravascular macrophages. *Annu Rev Physiol*, 56:47–67, 1994. 12, 95

[115] Vasile Stupar, Emmanuelle Canet-Soulas, Sophie Gaillard, Hasan Alsaid, Nicolau Beckmann, and Yannick Crémillieux. Retrospective cine 3he ventilation imaging under spontaneous breathing conditions: a noninvasive protocol for small-animal lung function imaging. *NMR Biomed*, 20(2):104–112, Apr 2007. 43

[116] J. E. Takasugi, D. E. Wood, J. D. Godwin, M. L. Richardson, J. O. Benditt, and R. K. Albert. Lung-volume reduction surgery for diffuse emphysema: radiologic assessment of changes in thoracic dimensions. *J Thorac Imaging*, 13(1):36–41, Jan 1998. 97

[117] Y. Tesfaigzi, M. J. Fischer, A. J. Martin, and J. Seagrave. Bcl-2 in lps- and allergen-induced hyperplastic mucous cells in airway epithelia of brown norway rats. *Am J Physiol Lung Cell Mol Physiol*, 279(6):L1210–L1217, Dec 2000. 68, 69

[118] W. M. Thurlbeck. Overview of the pathology of pulmonary emphysema in the human. *Clin Chest Med*, 4(3):337–350, Sep 1983. 100

[119] Bruno Tigani, Catherine Cannet, Harry Karmouty-Quintana, François-Xavier Blé, Stefan Zurbruegg, Elisabeth Schaeublin, John R Fozard, and Nicolau Beckmann. Lung inflammation and vascular remodeling after repeated allergen challenge detected noninvasively by mri. *Am J Physiol Lung Cell Mol Physiol*, 292(3):L644–L653, Mar 2007. 3

[120] Bruno Tigani, Elisabeth Schaeublin, Rosemary Sugar, Alan D Jackson, John R Fozard, and Nicolau Beckmann. Pulmonary inflammation monitored noninvasively by mri in freely breathing rats. *Biochem Biophys Res Commun*, 292(1):216–221, Mar 2002. 84

[121] Damian J Tyler, Matthew D Robson, R. Mark Henkelman, Ian R Young, and Graeme M Bydder. Magnetic resonance imaging with ultrashort te (ute) pulse sequences: technical considerations. *J Magn Reson Imaging*, 25(2):279–289, Feb 2007. 25

[122] Edwin J R van Beek and Eric A Hoffman. Functional imaging: Ct and mri. *Clin Chest Med*, 29(1):195–216, vii, Mar 2008. 1

[123] B. R. Wallau, A. Schmitz, and S. F. Perry. Lung morphology in rodents (mammalia, rodentia) and its implications for systematics. *J Morphol*, 246(3):228–248, Dec 2000. 8

[124] R. W. Watson, H. P. Redmond, and D. Bouchier-Hayes. Role of endotoxin in mononuclear phagocyte-mediated inflammatory responses. *J Leukoc Biol*, 56(1):95–103, Jul 1994. 68, 69

[125] K. N. Watt, J. Bishop, B. J. Nieman, R. M. Henkelman, and X. J. Chen. Oxygen-enhanced mr imaging of mice lungs. *Magn Reson Med*, 59(6):1412–1421, Jun 2008. 38, 120

[126] Marlène Wiart, Nathalie Davoust, Jean-Baptiste Pialat, Yves Berthezène, and Norbert Nighoghossian. Magnetic resonance imaging (mri) of inflammation in stroke. *Conf Proc IEEE Eng Med Biol Soc*, 2007:4316–4319, 2007. 72

[127] G. C. Winkler. Pulmonary intravascular macrophages in domestic animal species: review of structural and functional properties. *Am J Anat*, 181(3):217–234, Mar 1988. 12

[128] G. C. Winkler and N. F. Cheville. Monocytic origin and postnatal mitosis of intravascular macrophages in the porcine lung. *J Leukoc Biol*, 38(4):471–480, Oct 1985. 12

[129] Joanne L Wright and Andrew Churg. A model of tobacco smoke-induced airflow obstruction in the guinea pig. *Chest*, 121(5 Suppl):188S–191S, May 2002. 68

[130] Dmitriy A Yablonskiy, Alexander L Sukstanskii, Jason C Leawoods, David S Gierada, G. Larry Bretthorst, Stephen S Lefrak, Joel D Cooper, and Mark S Conradi. Quantitative in vivo assessment of lung microstructure at the alveolar level with hyperpolarized 3he diffusion mri. *Proc Natl Acad Sci U S A*, 99(5):3111–3116, Mar 2002. 98, 100, 110, 111

[131] R. B. Yang, M. R. Mark, A. Gray, A. Huang, M. H. Xie, M. Zhang, A. Goddard, W. I. Wood, A. L. Gurney, and P. J. Godowski. Toll-like receptor-2 mediates lipopolysaccharide-induced cellular signalling. *Nature*, 395(6699):284–288, Sep 1998. 69

[132] T. Zheng, Z. Zhu, Z. Wang, R. J. Homer, B. Ma, R. J. Riese, H. A. Chapman, S. D. Shapiro, and J. A. Elias. Inducible targeting of il-13 to the adult lung causes matrix metalloproteinase- and cathepsin-dependent emphysema. *J Clin Invest*, 106(9):1081–1093, Nov 2000. 107

List of publications and presentations:

I **Zurek M**., Bessaad A., Cieslar K., Crémillieux Y., Validation of Simple and Robust Protocols for High-Resolution Lung Proton MRI in Mice. *Magn Reson Med* 64: 401–407 (2010).

II **Zurek M**., Crémillieux Y. MRI of the lung: non-invasive protocols and applications to small animal models of lung disease. In. *In vivo NMR Imaging: Methods and Protocols*, Humana Press, USA, in press.

III **Zurek M.,** et al., Longitudunal and noninvasive assessment of emphysema evolution in a murine model using proton MRI. *Magn Reson Med*, in preparation.

IV **Zurek M**., et al., UTE imaging for detection of LPS- induced inflammation in rat lung: improving specificity and localization of early stage markers of COPD. *NMR in Biomed*, in preparation.

V **Zurek M**., Carrero-Gonzalez L., Bucher S., Kaulisch T., Stiller D., Crémillieux Y. Inflammation assessment in the lungs of LPS-challenged rodents: Comparison between radial ultra short echo time (UTE) and Cartesian MR Imaging. In ISMRM-ESMRMB Joint Annual Meeting, Stockholm, Sweden, pages 2504, 1-7 May 2010. (poster)

VI **Zurek M**., Cieslar K., Sigovan M., Bessaad A., Canet-Soulas E., Cremillieux Y. Pulmonary Perfusion-Weighted Regional Measurements in Mouse – Primarily Results. In ISMRM, Hawaii, USA, pages 2005, 18-24 April 2009. (poster)

VII **Zurek M**., Bessaad A., Cieslar K., Crémillieux Y. "Constant Repetition Time" Imaging Protocols for High Resolution Lung Proton MR Imaging in Mice. In ISMRM, Hawaii, USA, pages 2696, 18-24 April 2009. (poster)

VIII **Zurek M**., Ultra-short echo time (UTE) MR imaging of the lung in small animals. Phelinet Workshop on lung imaging: latest developments and medical applications, Cracow, Poland, 24-27 May 2010. (oral presentation)

Magnetic Resonance in Medicine 64:401–407 (2010)

Validation of Simple and Robust Protocols for High-Resolution Lung Proton MRI in Mice

Magdalena Zurek, Amine Bessaad, Katarzyna Cieslar, and Yannick Crémillieux*

One fundamental limitation of spatial resolution for in vivo MR lung imaging is related to motion in the thoracic cavity. To overcome this limitation, several methods have been proposed, including scan-synchronous ventilation and the cardiac gating approach. However, with cardiac and ventilation triggered techniques, the use of a predetermined and constant sequence repetition time is not possible, resulting in variable image contrast. In this study, the potential of two "constant repetition time" approaches based on retrospective self-gating and signal averaging were investigated for lung imaging. Image acquisitions were performed at a very short echo time for visualization of the lung structures and the parenchyma. Highly spatially resolved images acquired using retrospective self-gating, signal averaging technique and conventional cardiorespiratory gating are presented and compared. Magn Reson Med 64:401–407, 2010. © 2010 Wiley-Liss, Inc.

Key words: self-gating; free-breathing; gated acquisition; short echo time imaging; lung MRI; UTE; mouse imaging

Recent applications of MRI techniques in lung disease evaluation have raised growing interest in lung proton MRI of small animals (1,2). As demonstrated in recent studies (3–7), proton-based MRI can be envisioned as a powerful and versatile tool in pharmacological investigations of pulmonary disorders. It can be used for noninvasive pathology characterization and the evaluation of new treatments' effects in vivo.

However, lung imaging using proton MR remains a challenge. Low proton density in the lung parenchyma, combined with local magnetic inhomogeneities around air-filled alveoli, results in low image signal to noise ratio (SNR) and rapid signal loss due to the T_2* decay. For instance, at 4.7 T, a magnetic field commonly used in small animal scanners, T_2* in the lung parenchyma is about 500 μs (8). Thus, lung parenchyma usually appears dark in MR images acquired with a conventional echo time (~milliseconds) imaging sequences. Therefore, submillisecond echo time sequences are required for visualization of the lung parenchyma.

Additionally, the motion of the structures within the thoracic cavity during the breathing cycle and the cardiac motion cause image artifacts, degrading the spatial resolution. To address this issue, one can acquire high-resolution images using scan-synchronous ventilation, cardiac gating, or combined approaches (9–11). Although synchronizing the image acquisition to the breathing cycle and gating to the cardiac cycle allows one to obtain high spatial resolution in images of rodents' lungs (10,12), it increases the complexity of the MR protocol. This yields a reduced imaging protocol efficiency, a key parameter in investigation of animal models or in pharmacological studies of diseases, where large throughput and simple imaging protocol are usually sought. Moreover, cardiac and ventilation triggered techniques do not allow the use of sequence constant repetition time, resulting in a possibly varying image contrast. This can lead to difficulties in the interpretation of image readouts when quantification of changes in signal amplitude or in a tissue relaxation time is required. Alternatively, motion artifacts in lungs can be efficiently reduced using signal averaging (8). In this approach, the animals are allowed to breathe spontaneously and images are acquired without the use of either cardiac or respiratory triggering. This technique has been applied in numerous investigations of lung diseases in rats and mice (1,2,4–8).

Another efficient way to reduce motion artifacts is the use of radial *k*-space trajectory (13–15). Radial *k*-space acquisition has proven to be appropriate for lung imaging applications (16–19). Besides the advantage of artifact reduction generated by moving structures (13–15), this type of *k*-space sampling enables a significant shortening of the echo time and thus increases the signal from the lung parenchyma. Another interesting feature of radial imaging is the repetitive sampling of the *k*-space center, giving access to total NMR signal amplitude after each radiofrequency excitation. This property can be used to retrospectively monitor physiologic functions such as cardiac or respiratory cycles. It has recently been applied for the acquisition of time-resolved ^{3}He ventilation images in spontaneously breathing animals (20). Similarly, in proton MRI this approach has been demonstrated for the reconstruction of time-resolved cardiac images synchronized with cardiac and respiratory cycles (21). In both cases, the technique relies on the retrospective use of the MR signal intensity variations induced by cardiac and respiratory events.

In this study, we investigated and compared the performance of a short echo time radial sequence for lung MRI in mice in three different experimental setups, namely, standard cardiorespiratory (CR) gating acquisition, signal averaging (SA) acquisition, and cardiorespiratory retrospective self-gated (RSG) acquisition.

MATERIALS AND METHODS

Animal Preparation

Experiments were performed on 4.7 T 10-cm-bore magnet (Oxford, UK) interfaced to a MR consol (Bruker,

Université de Lyon, Lyon, France.

*Correspondence to: Yannick Crémillieux, PhD., ESCPE, La Doua, 43 Boulevard du 11 Novembre 1918, 69622 Villeurbanne Cedex, France. E-mail: yannick.cremillieux@univ-lyon1.fr

Received 10 July 2009; revised 19 November 2009; accepted 17 December 2009.

DOI 10.1002/mrm.22360

Published online in Wiley InterScience (www.interscience.wiley.com).

Ettlingen, Germany). Female C57BL/6 mice (average weight of 25 g) were anesthetized with isoflurane (concentration 1.5%; flow rate 0.4 L/min) administered via a face mask. For cardiac monitoring, electrocardiographic (ECG) electrodes were placed on the mice paws. The breathing cycle was controlled by a pressure sensor placed in the abdominal area. The animals were positioned supine in a home-built Alderman-Grant coil and body temperature was maintained by a regulated water flow. Experimental protocol was approved by the local ethics committee.

MR Acquisition

For visualization of the lung structures (blood vessels, bronchial tree) and the parenchyma, all MR acquisitions were performed with a short-echo-time radial imaging sequence. Four hundred radial views per image were collected, with an angular sampling range of 2π. The radial projections were evenly spaced in *k*-space, with a successive azimuthal increment of 181.1° to reduce motion artifacts. Free induction decay acquisition was triggered during read gradient ramping, starting immediately after slice excitation and slice refocusing gradient. For each radial view, the *k*-space origin was acquired with an effective echo time of 450 μs (the effective echo time is defined as the interval between the middle of the radiofrequency pulse and the first point of the acquisition). A radiofrequency excitation pulse of 0.2 ms was applied to excite a slice of 1.2 mm thickness.

Data acquisition was carried out using two different approaches: (1) "constant repetition time" imaging, and (2) cardiorespiratory-gated acquisition. The constant repetition time protocol was based either on RSG or on signal averaging approach.

For RSG and signal averaging acquisition schemes, the pulse repetition time and flip angle were set to 80 ms and 30°, respectively. In the case of RSG acquisition, 20 *k*-space sweeps were performed, resulting in an acquisition time of 10 min. The signal averaging acquisition consisted in averaging data from 20 consecutive scans before image reconstruction (total acquisition time of 10 min).

The typical repetition time for cardiorespiratory gating acquisition was equal to 400 ms, resulting in a 3-min total acquisition time. The flip angle was set to 20°.

For all three protocols, the images were acquired consecutively in the axial and the coronal planes.

To assess the accuracy of the investigated methods, the image synchronization algorithms were also tested on a phantom simulating breathing motion. The phantom consisted of a 2-cm-diameter syringe filled with a water solution doped with gadolinium-diethylenetriamine penta acetic acid (Gd-DTPA) to reduce T_1 and T_2 relaxation times. For the reproducibility tests, the phantom movements were performed along the longitudinal axis of the syringe, with two different oscillation rates of 30 and 60 cycles/min. The amplitude of oscillations was chosen to mimic the changes of the diaphragm position during respiration in mice and rats, with amplitudes of 1.5 and 3 mm, respectively (22). The phantom experiments were performed using the radial sequence with the same sequence parameters as for the in vivo studies.

Retrospective Lung Gating Procedure

A gridding algorithm (23) implemented in IDL (RSI, Boulder, CO) was used for the image reconstruction. Reconstructed images were interpolated into a 512×512 array with a Kaiser-Bessel interpolation kernel (23).

For RSG image reconstruction, the first sampled data point of each radial acquisition was extracted and plotted versus time. The typical pattern of the signal amplitude variations with two periodic signal modulations generated by both respiratory and cardiac cycle was observed (Fig. 1). The radial views within the user-defined range corresponding to the specific period in the breathing and the cardiac cycle were then selected based on these plots and used to fill in a given *k*-space matrix. Images were retrospectively synchronized to a given phase of the breathing and the cardiac cycle simultaneously.

Quantitative Analysis

In order to estimate and compare image quality, two parameters were evaluated: the sharpness and the noise level of the images. The noise level was defined as the standard deviation of signal intensity measured in a region of interest located in the image background. The sharpness was assessed using the standard procedure applied to vessel sharpness scoring of coronary arteries and septum from clinical MR images (24,25). The local maximum and minimum intensity value were determined along an intensity profile, and the distance d between the points at 80% and 20% of profile intensity was measured. The sharpness value was defined as $1/d$. The sharpness measurement was performed using a program developed using Matlab (The Mathworks, Inc., Natick, MA) with the following steps: (i) a set of points lying on the boundary of lung structure (vessels, diaphragm, ...) was selected, (ii) the selected points were fitted with a polynomial function ($n = 2$), (iii) tangents to the polynomial curve were plotted for each point of the curve, and (iv) intensity profiles perpendicular to the tangents were plotted and averaged. This procedure is illustrated in Fig. 2. Typically, 30 to 40 profiles were averaged along the considered structure to assess border sharpness.

RESULTS

Phantom Experiments

Figure 3 shows moving phantom images reconstructed from the averaged and gated-acquisitions (Fig. 3a-f). The image triggering was performed at the maximal phantom displacement. The motion was followed using a pressure transducer. For self-gating image synchronization, a signal from the *k*-space center was used and specific amplitudes of phantom oscillation were chosen in the reconstruction process (see "Retrospective Lung Gating Procedure"). The acquisition and processing algorithm used for the phantom studies was identical to that used for in vivo studies.

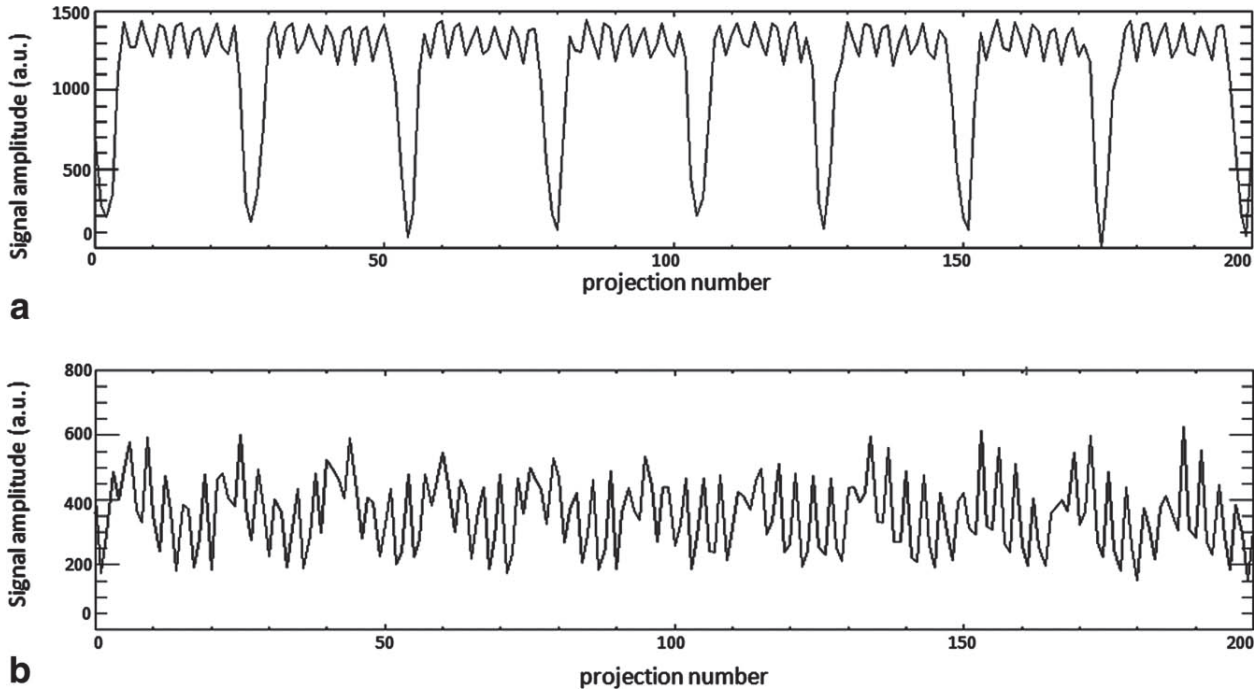

FIG. 1. NMR signal amplitude from the center of *k*-space acquired in coronal **(a)** and axial plane **(b)**. Low-frequency (0.5 Hz) and high-frequency (5 Hz) signal modulations correspond to the respiratory and cardiac cycles, respectively, as clearly seen in the top plot.

To show the relative impact of averaged and gated acquisitions on motion artifacts, the image quality was compared by using two image parameters, the sharpness and the noise level. Figure 4 compares the profiles measured at the boundary of the oscillating phantom for images acquired with oscillation rates of 30 cycles/min and 60 cycles/min and amplitudes of 1.5 mm and 3 mm, respectively. For both cases, the averaging shows a gentler slope of the profile, while the slopes of the two gating methods are comparable. The quantitative measurements of sharpness are presented in Table 1. Comparable sharpness values were obtained for standard synchronization and the self-gating technique. In contrast, the sharpness of the averaging approach was shown to be approximately two times lower with oscillations of 1.5 mm and four times lower with oscillations of 3 mm.

Table 2 shows the mean standard deviation scoring. The results indicate that the gating techniques permit the reduction of the noise level as compared to the averaging approach. No significant differences were found between the two synchronization techniques for any experimental setup.

In Vivo Experiments

Figure 1 shows the time course of the signal amplitude at the center of *k*-space for a set of consecutive radial views. The signal evolution for both coronal (Fig. 1a) and axial (Fig. 1b) slice orientation is depicted. Signal variation with two signal modulations can be observed: high-frequency variations due to the cardiac motion and low-frequency variations due to the respiratory cycle. Retrospective gating to the cardiac and respiratory cycle was based on the amplitude changes between the inspiration and exhalation phase in the breathing cycle and on the systole and diastole amplitude changes in the cardiac pulsation.

RSG and averaged and CR-gated images acquired in axial and coronal planes were compared. Examples of coronal lung images obtained with RSG, signal averaging, and cardiorespiratory gating approaches are shown

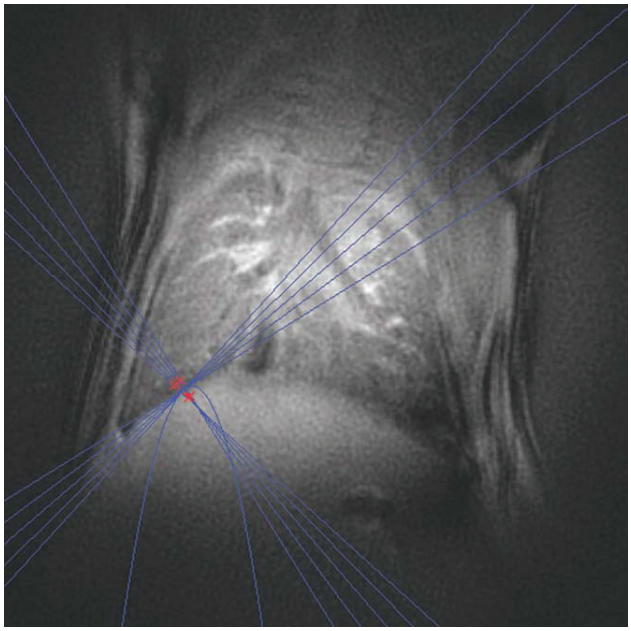

FIG. 2. Example of the intensity profiles generated and used for the calculation of the image sharpness at the diaphragm position. For clarity, only five intensity profiles are shown.

in Fig. 5. From visual inspection, one can note similar features, comparable image quality, and the absence of major motion artifacts related to respiratory or cardiac motion regardless of the imaging approach.

In order to estimate the degree of blurring suppression for each method, intensity profiles crossing either the diaphragm-liver boundary or going through a right pulmonary vein were generated for quantification and scoring of image sharpness. Typical averaged intensity profiles from coronal images are depicted in the Fig. 2.

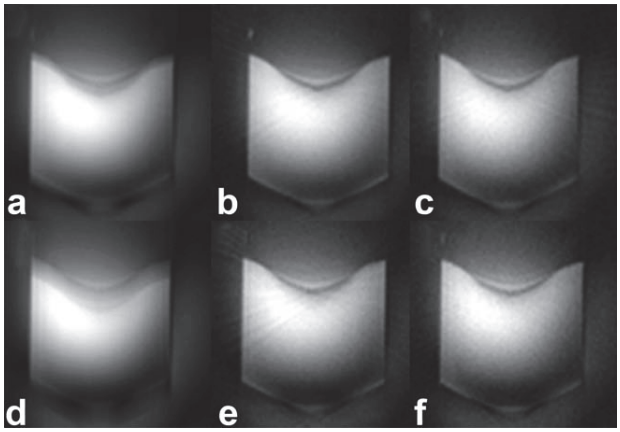

FIG. 3. From left to right: Averaged, synchronized, and self-gating image of a moving phantom with an oscillation rate of 30 cycles/min and an amplitude of 1.5 mm **(a-c)** and an oscillation rate of 60 cycles/min and an amplitude of 3 mm **(d-f)**. Motion was performed along the longitudinal axis of the phantom.

Comparable slopes of the intensity profiles were measured both at the diaphragm-liver interface and through a pulmonary vein. Table 1 summarizes the sharpness value for each acquisition approach measured in the region of the diaphragm. Comparable values were obtained for all approaches, confirming the qualitative similarity between images and intensity profiles.

Table 2 summarizes the noise level assessed for each of the acquisition methods. In the case of the signal averaging approach, the noise level was scaled with the square root of the number of averages.

Equivalent noise level was measured in self- and CR-gated images, while the noise level observed in the signal averaging acquisition was twice as big as that of the gated acquisitions.

The impact of averaging on the suppression of motion artifacts and image quality was investigated. Images acquired consecutively with an increasing number of averages were compared. Figure 6 shows coronal images acquired with one, five, and twenty averages. Typically, 20 averages were sufficient to suppress most of the streaking motion artifacts and the blurring located in the region of diaphragm and lung vasculature. Sharpness was assessed, as described above, for different numbers of image averages. To evaluate the sharpness measurement accuracy, the standard deviations of measured mean distance d were estimated and compared. Calculated standard deviations, 12% in the case of one and five averages and 4% variation for 20 averages, show that using 20 averages is sufficient for precise estimation of the image sharpness.

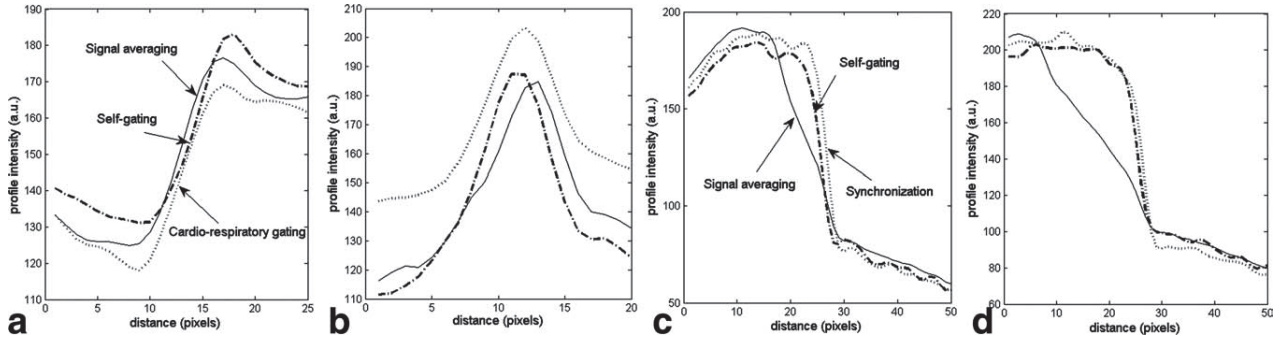

FIG. 4. Averaged line profiles obtained in vivo at the boundary of the diaphragm **(a)** the right pulmonary vein **(b)** and in the boundary of the moving phantom, with an oscillation rate of 30 cycles/min and an amplitude of 1.5 mm **(c)** and an oscillation rate of 60 cycles/min and an amplitude of 3 mm **(d)**.

Table 1
Sharpness Scores From Averaged, Synchronized, and Self-gated Images*

	Averaged image	Synchronized image	Self-gated image
Sharpness in vivo (pixels^{-1})	0.15 ± 0.01	0.18 ± 0.04	0.16 ± 0.02
Sharpness phantom, case 1 (pixels^{-1})	0.111 ± 0.003	0.23 ± 0.02	0.23 ± 0.03
Sharpness phantom, case 2 (pixels^{-1})	0.061 ± 0.004	0.25 ± 0.04	0.24 ± 0.02

*Values were obtained in coronal images from averaged intensity profiles crossing the diaphragm/liver boundary and the oscillating phantom, with the rate and amplitude of oscillation of 30 cycles/min and 1.5 mm (case 1) and 60 cycles/min and 3 mm (case 2). The standard deviation values were obtained from repeated measurements.

Table 2
Mean Noise Level Values Measured in Averaged, Synchronized, and Self-gated Images In Vivo and the Oscillating Phantom, With Rate and Amplitude of Oscillation equal to 30 Cycles/Min and 1.5 mm (Case 1) and 60 Cycles/Min and 3 mm (Case 2)*

Normalized noise level in image background	Averaged image	Synchronized image	Self-gated image
In vivo	8.64 ± 1.73	4.81 ± 0.26	3.85 ± 0.23
Phantom case 1	3.33 ± 0.22	1.53 ± 0.05	1.59 ± 0.06
Phantom case 2	3.54 ± 0.24	1.55 ± 0.08	1.71 ± 0.13

*The standard deviation values were obtained from repeated measurements.

DISCUSSION AND CONCLUSIONS

The efficacy of the signal averaging approach for motion artifact suppression in lung proton MRI images was previously demonstrated by Beckmann et al. (8) in rats and mice, using Cartesian *k*-space scanning. Since then, the signal averaging technique has been successfully applied to numerous animal models of lung disease for the detection and quantification of inflammation, mucous plugging, or lung fibrosis (4–7). For all the above-mentioned applications, this approach has been recognized as robust, easy to implement, and well adapted to scanning of large cohorts of animals.

The short-echo time radial *k*-space sampling represents the acquisition technique of choice when increased SNR from lung parenchyma and improved image resolution are sought. Combined with cardiorespiratory triggering and ventilation-synchronous scan, the approach has been shown to be very efficient for depicting fine anatomic details of a rodent's lungs (12,19,26). The main objective of this study was to determine whether short-echo-time non-triggered approaches can provide similar results, and thus two image parameters were measured, namely, the sharpness and the noise level. The image sharpness was used to assess the image resolution, while the noise level was measured for evaluating the impact of motion artifacts on the image quality.

The retrospectively cardiorespiratory-gated approaches using Cartesian and radial sampled signals have been previously reported in proton imaging for time-resolved imaging in humans (25,27) and small animals (21). The findings of the present study indicate that the self-gating approach is also applicable for lung imaging in small animals. Modulations of MR signal intensity induced by breathing and cardiac pulsations were noticeable in both coronal and axial imaging slices. Modulations caused by the animals' respiratory cycle were more pronounced in coronal then in axial images. This results from larger lung volume changes in the craniocaudal direction as compared to the left-right and anteroposterior orientation. Interestingly, the detection of signal variations due to the cardiac cycle was not restricted to slices encompassing parts of the cardiac muscle. Indeed, signal changes due to pulsing blood flow within pulmonary vasculature were detected in all imaged slices. These signal changes were used for reconstructing images synchronized with the cardiac cycle.

The results from sharpness measurements indicate that spatial resolutions equivalent to those of cardiorespiratory gating acquisitions can be obtained using self-gated or averaging approaches. In the case of averaging acquisition, this counterintuitive observation can be attributed to the peculiar behavior of radial acquisition in the presence of a moving structure. Indeed, in radial images motion artifacts are usually distributed as radial streaks in the periphery of the image. Furthermore, the acquisition of free induction decay signals at a very short echo time prevents the phase accumulation of moving spins in the presence of imaging gradients.

Similar diaphragm positions for all three imaging techniques were observed in coronal images (Fig. 5). Cardiorespiratory and self-gated lung images were acquired at the expiratory phase, with the animal breathing spontaneously at tidal volume. As seen from the MR signal intensity time curve in Fig. 1a, the fraction of time spent in expiration phase represents about two thirds of the total breathing cycle of the animal. As a result, in the signal averaging image, the diaphragm is seen in a position corresponding to the expiratory phase.

The noise level was measured in the image periphery, where the motion artifacts are presumably mainly located. A 2-fold higher noise level was observed in the

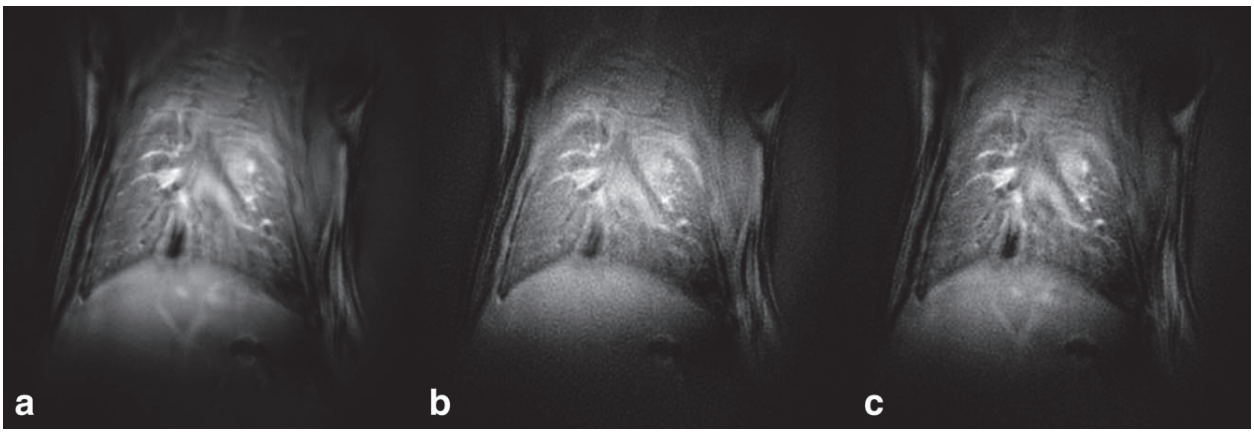

FIG. 5. Typical images of mice thorax acquired using the signal averaging approach (20 averages) **(a)**, the cardiorespiratory-gated approach **(b)**, and the RSG procedure **(c)**.

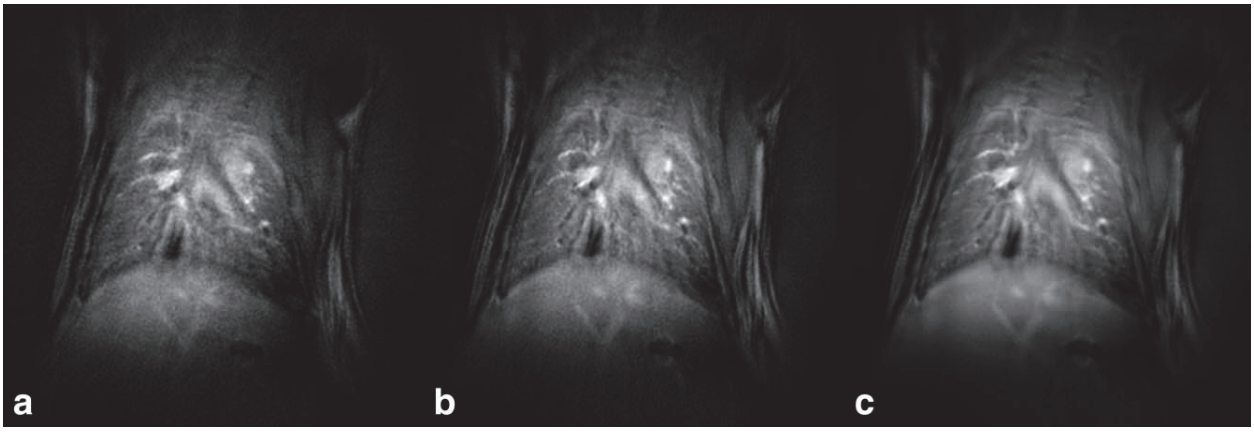

FIG. 6. Comparison of image quality for different number of averages (NA). NA was one **(a)**, five **(b)**, twenty **(c)**.

signal averaging acquisition. This higher noise level is an indication of increased fluctuating signal intensity related to motion, as can be suspected from non-gated acquisition. However, this increase in noise level did not affect the sharpness measurement within the lung, nor did it degrade the overall image quality.

If image SNR is of concern, the SNR per unit time provided by the different approaches has to be considered. When using appropriate radiofrequency excitation at Ernst angle, it can be demonstrated that signal averaging and CR-gated techniques can yield very similar SNR per unit time. On the contrary, the self-gated technique has a reduced SNR per unit time due to discarded radial views during the image reconstruction.

Despite its degraded SNR per unit time, self-gated acquisition offers the possibility of reconstructing lung images at different cardiac or respiratory cycles. Figure 7 shows a typical axial image of mouse thorax obtained using the retrospective-gated technique at two different cardiac cycle phases. In this case, the projections corresponding to systolic and diastolic phases of the cardiac cycle were chosen and the images corresponding to each phase were reconstructed. Depending on a cardiac phase, one can observe signal intensity variations in the parenchyma which are attributed to changes in lung perfusion. Furthermore, if needed the acquired *k*-spaces can be averaged later to generate higher SNR images.

The results obtained in the phantom study validate the accuracy of the self-gating method for motion artifacts suppression; the sharpness and noise level were found similar to those obtained with the standard gating technique. However, in contrast to in vivo experiments, a degradation of the sharpness value was observed for signal averaging acquisition. Although the frequencies and amplitudes of phantom displacement correspond to the breathing rate and diaphragm displacement in mice and rats, the pattern of the phantom's motion was

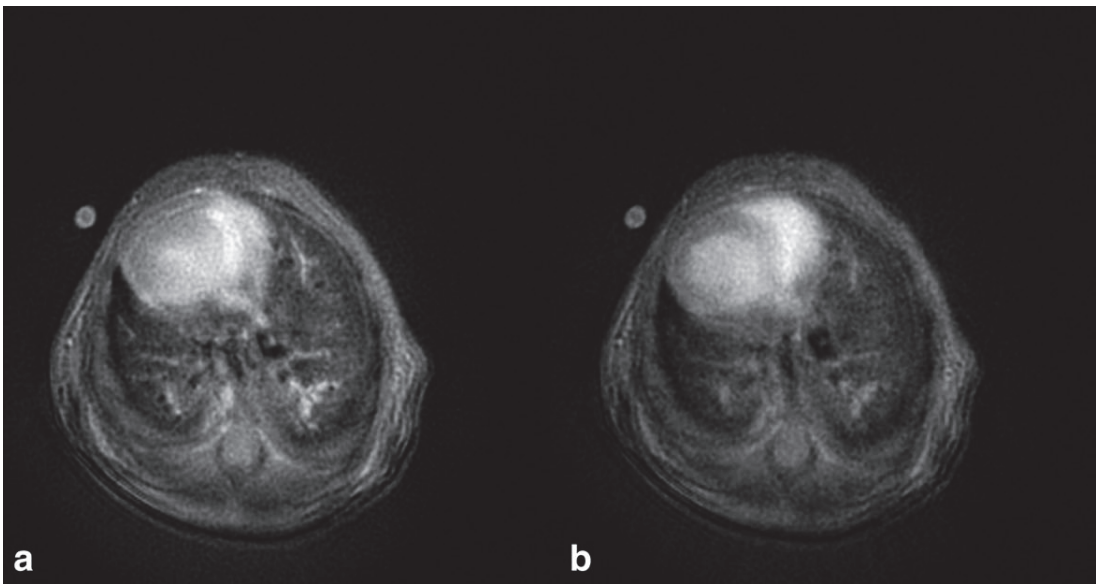

FIG. 7. Comparison of self-gated transverse pulmonary images corresponded to the systolic **(a)** and diastolic **(b)** phases of the cardiac cycle.

different to that observed in vivo (as mentioned above, the fraction of time spent in the expiration phase represents about two thirds of the total breathing cycle of the animal).

In conclusion, in this study different short echo time radial imaging protocols were applied for proton lung imaging in small animals during spontaneous breathing. Constant repetition time methods and the cardiorespiratory-gated approach were compared. Within the limit of the nominal image resolution of this study (pixel size of 54 μm $\times$ 54 μm), parenchyma and vascular structures in mouse lung were visualized, with equivalent spatial resolution for all the applied techniques. The use of non-cardiorespiratory-gated techniques offers several advantages. First of all, they simplify the imaging protocol for lung MRI of rodents. Second, the images are acquired with an operator-defined repetition time, allowing the control of the image contrast. Finally, the retrospectively gated approach offers the possibility of lung imaging at multiple phases of the cardiac or respiratory cycles.

In the future, these non-gated short-echo time radial approaches might be profitably used for the large-scale and high-throughput investigation of lung structural or functional changes in mice or rats models of lung diseases.

ACKNOWLEDGMENTS

M.Z. and K.C. acknowledge a fellowship from the European Network PHELINET (MRTN-CT-2006-36002).

REFERENCES

1. Beckmann N, Cannet C, Karmouty-Quintana H, Tigani B, Zurbruegg S, Blé FX, Crémillieux Y, Trifilieff A. Lung MRI for experimental drug research. Eur J Radiol 2007;64:381–396.
2. Beckmann N, Crémillieux Y, Tigani B, Karmouty Quintana H, Blé FX, Fozard JR, Lung MRI in small rodents as a tool for the evaluation of drugs in models of airways diseases. In: Beckmann N, editor. In vivo MR techniques in drug discovery and development. New York: Taylor & Francis Group; 2006. p 351–372.
3. Olsson LE, Lindahl M, Onnervik PO, Johansson LB, Palmér M, Reimer MK, Hultin L, Hockings PD. Measurement of MR signal and T2* in lung to characterize a tight skin mouse model of emphysema using single-point imaging. J Magn Reson Imaging 2007;25:488–494.
4. Beckmann N, Tigani B, Ekatodramis D, Borer R, Mazzoni L, Fozard JR. Pulmonary edema induced by allergen challenge in the rat: non-invasive assessment by magnetic resonance imaging. Magn Reson Med 2001;45:88–95.
5. Karmouty-Quintana H, Blé F-X, Cannet C, Zurbruegg S, Fozard JR, Page CP, Beckmann N. In vivo pharmacological evaluation of compound 48/80-induced airways oedema by MRI. Br J Pharmacol 2008; 154:1063–1072.
6. Karmouty-Quintana H, Cannet C, Sugar R, Fozard JR, Page CP & Beckmann N. Capsaicin-induced mucus secretion in rat airways assessed in vivo and non-invasively by magnetic resonance imaging. Br J Pharmacol 2007;150:1022–1030.
7. Karmouty-Quintana H, Cannet C, Zurbruegg S, Blé FX, Fozard JR, Page CP, Beckmann N. Proton MRI as a noninvasive tool to assess elastase-induced lung damage in spontaneously breathing rats. Magn Reson Med 2006;56:1242–1250.
8. Beckmann N, Tigani B, Mazzoni L, Fozard JR. MRI of lung parenchyma in rats and mice using a gradient-echo sequence. NMR Biomed 2001;14:297–306.
9. Hedlund LW, Cofer GP, Owen SJ, Allan Johnson G. MR-compatible ventilator for small animals: computer-controlled ventilation for proton and noble gas imaging. Magn Reson Imaging 2000;18:753–759.
10. Cassidy PJ, Schneider JE, Grieve SM, Lygate C, Neubauer S, Clarke K. Assessment of motion gating strategies for mouse magnetic resonance at high magnetic fields. J Magn Reson Imaging 2004;19: 229–237.
11. Maï W, Badea CT, Wheeler CT, Hedlund LW, Johnson GA. Effects of breathing and cardiac motion on spatial resolution in the microscopic imaging of rodents. Magn Reson Med 2005;53:858–865.
12. Johnson GA, Cofer GP, Hedlund LW, Maronpot RR, Suddarth SA. Registered ^{1}H and ^{3}He magnetic resonance microscopy of the lung. Magn Reson Med 2001;45:365–370.
13. Glover GH, Pauly JM. Projection reconstruction techniques for reduction of motion effects in MRI. Magn Reson Med 1992;28:275–289.
14. Brau AC, Hedlund LW, Johnson GA. Cine magnetic resonance microscopy of the rat heart using cardiorespiratory-synchronous projection reconstruction. J Magn Reson Imaging 2004;20:31–38.
15. Schäffter T, Rasche V, Carlsen IC. Motion compensated projection reconstruction. Magn Reson Med 1999;41:954–963.
16. Bergin CJ, Pauly JM, Macovski A. Lung parenchyma: projection, reconstruction MR imaging. Radiology 1991;179:777–781.
19. Gewalt SL, Glover GH, Hedlund LW, Cofer GP, MacFall JR, Johnson GA. MR microscopy of the rat lung using projection reconstruction. Magn Reson Med 1993;29:99–106.
18. Shattuck MD, Gewalt SL, Glover GH, Hedlund LW, Johnson GA. MR microimaging of the lung using volume projection encoding. Magn Reson Med 1997;38:938–942.
19. Bergin CJ, Glover GM, Pauly J. Magnetic resonance imaging of lung parenchyma. J Thorac Imaging 1993;8:12–17.
20. Stupar V, Canet-Soulas E, Gaillard S, Alsaid H, Beckmann N, Crémillieux Y. Retrospective cine ^{3}He ventilation imaging under spontaneous breathing conditions: a non-invasive protocol for small-animal lung function imaging. NMR Biomed 2007;20:104–112.
21. Hiba B, Richard N, Janier M, Croisille P. Cardiac and respiratory double self-gated cine MRI in the mouse at 7 T. Magn Reson Med 2006;55:506–513.
22. Segars WP, Tsui BMW, Frey EC, Johnson GA, Berr SS. Development of a 4D digital mouse phantom for molecular imaging research. Mol Imaging Biol 2004;6:149–159.
23. Jackson JI, Meyer CH, Nishimura DG, Macovski A. Selection of a convolution function for Fourier inversion using gridding. IEEE Trans Med Imaging 1991;10:473–478.
24. Shea S, Kroeker R, Deshpande V, Laub G, Zheng J, Finn J, Li D. Coronary artery imaging: 3D segmented k-space data acquisition with multiple breath-holds and real-time slab following. J Magn Reson Imaging 2001;13:301–307.
25. Larson AC, Kellman P, Arai A, Hirsch GA, McVeigh E, Li D, Simonetti OP. Preliminary investigation of respiratory self-gating for free-breathing segmented cine MRI. Magn Reson Med 2005;53: 159–168.
26. Kuethe DO, Adolphi NL, Fukushima E. Short data-acquisition times improve projection images of lung tissue. Magn Reson Med 2007;57: 1058–1064.
27. Oechsner M, Pracht ED, Staeb D, Arnold YFT, Köstler H, Hahn D, Beer M, Jakob PM. Lung imaging under free-breathing conditions. Magn Reson Med 2009;61:723–727.

Chapter 24

MRI of the Lung: Non-invasive Protocols and Applications to Small Animal Models of Lung Disease

Magdalena Zurek and Yannick Crémillieux

Abstract

Magnetic resonance imaging (MRI) can be used in pre-clinical studies as a non-invasive imaging tool for assessing the morphological and functional impact of lung diseases and for evaluating the efficacy of potential treatments for airways diseases. Hyperpolarized gases (^{3}He or ^{129}Xe) MRI provides insight into the lung ventilation function. Lung proton MRI provides information on lung diseases associated with inflammatory activity or with changes in lung tissue density. These imaging techniques can be implemented with non-invasive protocols appropriate for longitudinal investigations in small animal models of lung diseases. This chapter will detail two ^{3}He and proton lung MR imaging protocols applied on two models of lung pathology in rodents.

Key words: Magnetic resonance imaging, MRI, lung, mouse, rat, rodent, hyperpolarized gases, Helium-3, Xenon-129, lung ventilation imaging, bronchoconstriction, methacholine, asthma model, LPS, lung inflammation, spontaneous breathing lung imaging.

1. Introduction

The low proton density of the lungs (approximately 20–30%) combined with susceptibility gradients induced by the air–tissue interfaces and motions within thoracic cavity produces an inherently weak MR signal from the lung parenchyma and makes the lungs the most challenging organ to be imaged by means of MRI.

Despite difficulties associated with lung MRI, there is growing interest in the potential of MR techniques applied to lung diagnostics in patients or to the investigation of lung diseases in animal models. This increase in MR applications for lungs

L. Schröder, C. Faber (eds.), *In Vivo NMR Imaging*, Methods in Molecular Biology 771,
DOI 10.1007/978-1-61779-219-9_24,

is related to technological breakthrough (use of hyperpolarized gases such as ^{3}He or ^{129}Xe), hardware improvement (MR gradient performance), and methodological progress (for instance short echo time imaging or oxygen-enhanced lung MRI). The application of MRI to lungs is further motivated by its inherent non-invasiveness (of high interest in the case of chronic diseases), its potential for translational research and its complementary readouts as compared to those of CT imaging.

The large NMR signal offered by hyperpolarized (HP) gases allows imaging their distribution in the pulmonary tree and the alveolar spaces. The first NMR biomedical application of HP ^{129}Xe was reported in 1994 with intrapulmonary space imaging of excised mouse lungs (1) (*see* also **Chapter 10**). The first in vivo lung ventilation images obtained in rodents using HP ^{3}He were reported 1 year later (2) followed by the first human lung images (3, 4). The spatial resolution of lung ventilation images obtained by means of ^{3}He exceeds by an order of magnitude the spatial resolution that is routinely obtained with scintigraphy techniques using radioactive gases. In human studies, typical spatial resolutions in the millimeter range are reported while in rodent studies sub-millimetric resolutions are usually reached (5, 6).

Apparent diffusion coefficient (ADC) values of HP gases in airspaces depend on the restriction of gas atoms diffusion by the broncho-alveolar walls. The diffusion length of helium atoms during typical diffusion-sensitizing times (a few milliseconds) exceeds the diameter of alveolar sacks (a few hundreds of micrometers). Hence, in the timescale of MR diffusion acquisition, ^{3}He diffusion in alveolar space takes place in a restricted regime. The dependence of HP gases ADC values upon the dimensions of the alveolar space has been proposed as a non-invasive approach for probing the lung architecture at a sub-pixel level. Indeed, ^{3}He ADC values have been shown to significantly increase in patients with emphysema compared to healthy volunteers (7). These ^{3}He ADC changes in emphysematous lungs are attributed to the morphological changes in alveolar structure and more specifically to the airspace enlargements that characterize emphysema (8–10). Emphysema disease in animal models has been extensively studied using ^{3}He and ^{129}Xe MRI. Elastase-induced emphysema has been investigated in rat (8, 10), mouse (11), and rabbit (12) using ^{3}He or ^{129}Xe diffusion MRI. When measurements were carried out at total lung capacity, ^{3}He ADC values increased from 0.15 cm^2/s in normal rats to 0.18 cm^2/s in elastase-challenged animals; moreover, a significant correlation was found between the ^{3}He ADC values and the alveolar internal area assessed by histology in lungs fixed with formalin at an airway pressure corresponding to the total lung capacity (10). Similarly, ^{3}He ADC values averaged over the entire lungs were found to

be approximately 25% higher in emphysema mice than in healthy animals (11).

The relaxation rate R_1 of ^{3}He varies linearly with the partial pressure of oxygen through dipolar interactions of the ^{3}He nucleus with paramagnetic molecular oxygen (13). By measuring the time variation of the relaxation time of HP ^{3}He in the lungs, it is then possible to compute locally the intrapulmonary oxygen concentration and the oxygen consumption rate of oxygen in vivo (14–18). As the intrapulmonary pO_2 distribution is governed by local ventilation, perfusion, and O_2 uptake, pO_2 assessment can be used to evaluate lung function. The rate at which oxygen reaches the alveolus is determined by its ventilation and the inspired pO_2. The rate at which oxygen leaves the alveolus is determined by its perfusion. Consequently, the determination of alveolar pO_2 is an indirect measure of the ventilation/perfusion ratio. The potential of ^{3}He imaging for detecting perfusion abnormalities due to their effect on alveolar pO_2 was demonstrated in an experimental pig model (19). After isolated pulmonary arterial occlusion using a balloon catheter, a focal T_1 reduction corresponding to an abnormally high pO_2 (because of the absence of perfusion) was observed, which normalized upon deflation of the balloon. More recently, pO_2 imaging and oxygen depletion rate imaging were extended to small animal investigation in rat and mouse studies (20, 21).

Chemical shift imaging has been demonstrated using HP ^{129}Xe. The high solubility in blood and tissues and the large chemical shift (several hundreds of ppm) of xenon allow one to differentiate between xenon in alveoli and xenon dissolved in tissue. The so-called xenon polarization transfer contrast (XTC) technique aims to probe the xenon exchange between alveolar space and blood/tissue compartments (22). The method is based on the selective destruction of the xenon polarization in the lung parenchyma. Due to the rapid exchange of xenon between the gas and tissue-dissolved phases, the depolarization of xenon dissolved in tissue affects the xenon signal from the gaseous phase. Using an appropriate pixel-based signal analysis of this effect, the XTC lung images with a contrast related to the tissue and alveolar xenon exchange can be obtained.

The potential of ^{3}He MRI for assessing airways constriction has been investigated in the methacholine-induced bronchoconstriction rat model. Using a Cine MRI approach in which image acquisition was synchronized with the inhalation of the gas mixture (^{3}He with oxygen and nitrogen), a heterogeneously distributed airways constriction resulting in a partition of the lung between ventilated and non-ventilated regions was observed (23). The diameter of the main airways decreased by approximately 11% following methacholine

challenge (30 μg). In a methacholine-induced bronchoconstriction rat model (24), dynamic ventilation image series obtained from a single breath were used to generate parametric pixel-by-pixel maps of gas arrival time, filling time constant, inflation rate, and gas volume. Quantitative and regional analysis of gas flow, volume, and arrival times demonstrated statistically significant differences between the baseline and methacholine-constricted states.

In animals, hyperpolarized ^{3}He can be inhaled using either tracheal intubation or invasive tracheotomy. The gas delivery to the animal lungs can be performed using a variety of protocols and apparatus. Small animal respirators compatible with polarized ^{3}He have been developed by several groups (25–27). These respirators allow a fine control of the delivered gas volume and of the lung ventilation timing. Triggering and synchronization of the imaging sequence with the gas delivery can be used for performing lung ventilation. However, acquisition of ^{3}He lung images in spontaneously breathing mice and rats has also been reported recently (28, 29). In this case, gas was administered through a mask.

Apart from the HP gases imaging techniques, many efforts have been made to employ proton lung MRI. The insignificant cost, easy protocol implementation, and versatility of proton lung MR imaging make it an adequate tool in research of lung diseases in animal model studies. Consequently, the development of methodologies and experimental protocols for proton MR pharmacological studies became of interest (30–32). For instance, it was recently demonstrated that conventional gradient echo MR imaging can be efficiently applied to show inflammation hallmark in various models of lung diseases. Considering that a significant contrast is obtained between a dark-appearing lung parenchyma and hyperintense fluids being associated with diverse lung diseases, the gradient echo imaging has been successfully applied to numerous animal models for the detection and quantification of fluid secretion in asthma, chronic obstructive pulmonary diseases (COPD), emphysema, or lung fibrosis (33–36). Furthermore, potential motion artifacts from breathing and cardiac cycles can be reduced by image averaging. For all the above-mentioned applications, the averaging approach based on Cartesian encoding has been recognized as robust, easy to implement, and well adapted to scanning of large cohorts of animals. In order to detect signal from the lung parenchyma, characterized by a very short transverse relaxation time, non-standard imaging techniques are required. For instance a radial ultra-short echo time (UTE) sequence which reduces considerably the echo time (TE) was proposed for this application (37, 38). With the use of a UTE sequence, a TE of the order of 450 μs (with a standard excitation pulse) can be achieved allowing for visualization

of lung tissue with a high signal-to-noise ratio (SNR) (39). The improved parenchyma visualization may enable the detection of emphysema and/or fibrosis-like microstructural changes of the lung (40–42) or alternations in ventilation/perfusion ratio (43–45) reflecting different pathophysiological effects in lung injury models. UTE radial imaging has recently also been applied to detect edema and mucus plugging in an acute lipopolysaccharide (LPS)-induced inflammation rat model (46). The radial encoding is less sensitive to motion and blurring artifacts occurring in the thoracic cavity during respiration (47, 48), and thus can provide more accurate results as compared to Cartesian imaging techniques.

There is a great interest in investigating the relationship between anatomical and functional changes in lung disorders. Therefore, proton lung MRI combined with ventilation imaging using HP gases was explored in order to examine the correlation between lesion area detected by proton MRI and the observed ventilation defects (49). To assess the regional pulmonary ventilation, oxygen-enhanced MRI is a technique of choice (50). Molecular oxygen is weakly paramagnetic and shortens the spin–lattice relaxation time (T_1) of the lung parenchyma. The effect of ventilation is thus visualized by signal intensity increase in the T_1-weighted images of the lung acquired with subjects breathing 100% oxygen as compared to room air. Oxygen-enhanced ventilation imaging was applied in human studies to show the ventilation defects in fibrotic, emphysematous, and pneumonic lungs (51, 52). Recently, the investigation of lung ventilation in mouse using oxygen as a contrast agent was reported (43).

Another challenge of proton lung MRI arises from the cardiac and respiratory movements, which can degrade the image quality and make the correct image readout impossible. To address this issue, several acquisition methods have been proposed, including scan-synchronous ventilation combined with electrocardiographic (ECG) synchronization (53, 54), the averaging method (55), and self-gating approaches (56–58). In contrast to conventional synchronization, the averaging and self-gating methods permit to avoid delays associated with the setup of ECG equipment, thus reducing the overall imaging time and the cost of the studies involving a large number of animals. The self-gating methods combined with a radial UTE acquisition allow obtaining highly resolved images of lung parenchyma, which can be synchronized to a specific phase of the cardio-respiratory cycle (39). Alternatively, the combination of UTE acquisition with cardio-respiratory gating can be used to assess and quantify the regional signal changes in the lung parenchyma due to blood perfusion in the lungs (44).

This chapter focuses on two selected lung imaging techniques applied to small animal, namely hyperpolarized (HP) ^{3}He MRI

and ultra-short echo time (UTE) proton MRI. The potential of these techniques is illustrated and detailed on two models of lung pathologies in rodents. Both presented approaches are suitable for longitudinal investigations in animal models of lung diseases.

2. Materials

2.1. Breathing of Hyperpolarized ^{3}He

1. 40 mL hyperpolarized ^{3}He.
2. 60-mL syringe.
3. Two- and three-way Luer-lock valves.
4. Rat or mouse.
5. Animal mask (*see* **Note 1**).
6. Latex balloon.
7. Warming pad.
8. Anesthesia (e.g., ketamine/xylazine) (*see* **Note 2**).

2.2. Bronchoconstriction Induction by Injection of Methacholine

1. Methacholine (85 μg in 1 mL of saline).
2. Saline.
3. Heparin.
4. Infusion syringe pump.
5. 2-mL syringe.
6. 22–25 gauge needle (rat) or 27–30 gauge needle (mouse) attached to a 1-mL syringe.
7. Rat or mouse.
8. Anesthesia (e.g., ketamine/xylazine) (*see* **Note 2**).

2.3. Inflammation Induction by the Instillation of Endotoxin Lipopolysaccharide (LPS)

1. LPS (1 mg/kg in 0.2 mL of saline).
2. Balance.
3. 1-mL tube.
4. Vortexer.
5. Rat (e.g., Brown Norway, Wistar).
6. Blunt forceps, light source, 1-mL syringe, 26-G catheter, ventilator.
7. Anesthesia (e.g., ketamine/xylazine) (*see* **Note 2**).
8. Warming pad.
9. A mask, gloves, lab coat, and eye protection.

3. Methods

3.1. Ventilation Imaging of Bronchoconstriction Model Under Spontaneous Breathing Conditions

3.1.1. Animal Preparation

1. Anesthetize the animal (e.g., with intraperitoneal injection of ketamine/xylazine).
2. Insert a 22–25 gauge needle (rat) or 27–30 gauge needle (mouse) into a vein of the tail. Flush the line with saline solution and connect a 2-mL syringe filled with methacholine solution to the catheter.
3. Place the head of the animal within the mask (**Fig. 1**). The homemade mask can be screwed, at one end, to the balloon containing the polarized ^{3}He. On the other end of the mask, a latex sleeve surrounds the neck of the animal. Tighten the latex sleeve around the neck of the animal in order to limit air leakage.
4. Center the chest of the animal in the NMR rf coil. Position the NMR coil within the magnet isocenter for MRI acquisitions.

3.1.2. Free Breathing and Acquisition of Ventilation Images

1. Extract HP ^{3}He from the storage cell to a 60-mL syringe. Transfer the ^{3}He gas from the syringe to the latex balloon. Attach the balloon to the mask positioned on the head of the animal. Allow the animal to breathe spontaneously the gas from the balloon (**Fig. 1**).
2. Launch the MRI sequence. Following MR acquisition (typically 20 s time), disconnect the balloon from the head mask and allow the animal to recover.
3. This protocol can be repeated to investigate bronchoconstrictive effects of methacholine. Trigger intravenous injection of methacholine solution (10 μg/mL) using infusion syringe pump (6 mL/h for rat).
4. Repeat Steps 1 and 2 as many times as required by the follow-up imaging protocol.

3.1.3. Imaging Parameters

MRI field strength is equal to 2 T (optimal magnetic field strength for HP gases ventilation imaging in small animals). To acquire ^{3}He signal at very short echo, a radial-sampling imaging sequence is used.

Repetition time (TR) = 5 ms; TE = 40 μs; field of view (FOV) = 80 mm; number of radial directions (NA) = 200; number of sampled points (NS) = 128; number of experiments (NEX) = 20; no slice thickness; flip angle = 12°; total acquisition time = 20 s.

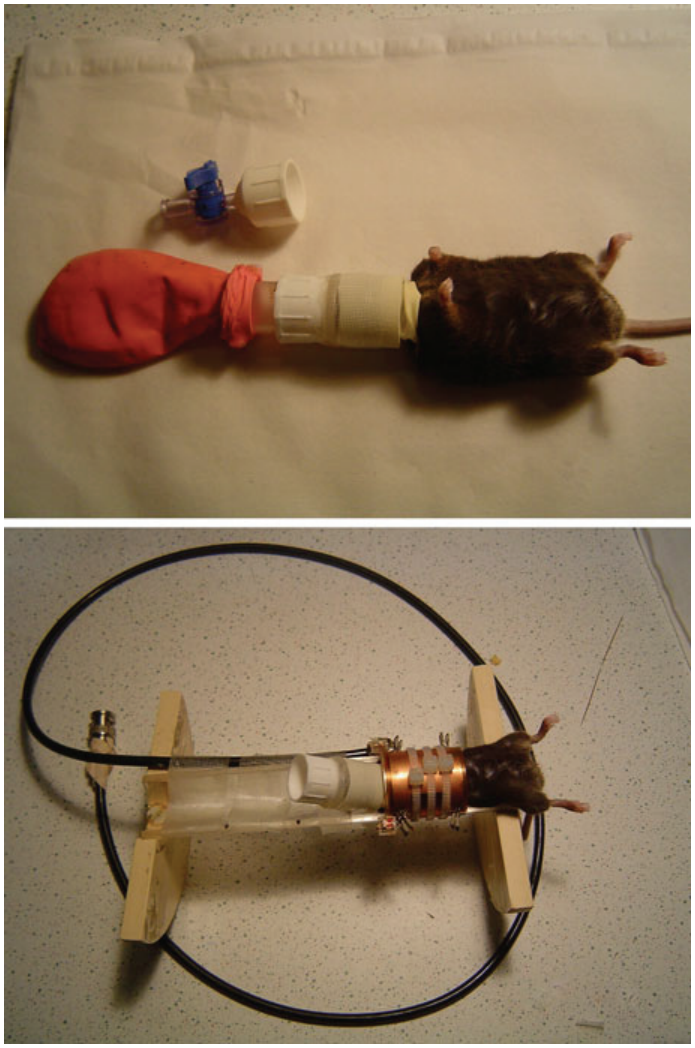

Fig. 1. Illustration of the experimental setup for the lung MR imaging studies using hyperpolarized gas with free breathing. The *top picture* shows the homemade mask positioned on the head of the animal (C57BL/6 mouse). The head mask is connected to a balloon filled with gas. The *bottom picture* represents the animal, with the mask, positioned in the NMR rf coil. The balloon is connected to the mask once the animal is positioned within the magnet.

3.1.4. Reconstruction Parameters

Image reconstruction is performed using a gridding algorithm (regridding of radially acquired samples onto a Cartesian grid). Reconstruction oversampling factor = 2; sampling density compensation using the Jacobian of the transformation; Kaiser–Bessel kernel parameters: shape factor $\alpha = 2.8$, window width $L = 3.0$; final reconstruction matrix 256 × 256 (*see* **Note 3**).

Images of ventilation synchronized with the breathing cycle of the animal are obtained using the retrospective Cine reconstruction techniques (29). These time-resolved images of ventilation can be processed to generate parametric maps of gas arrival time in the broncho-alveolar space (29).

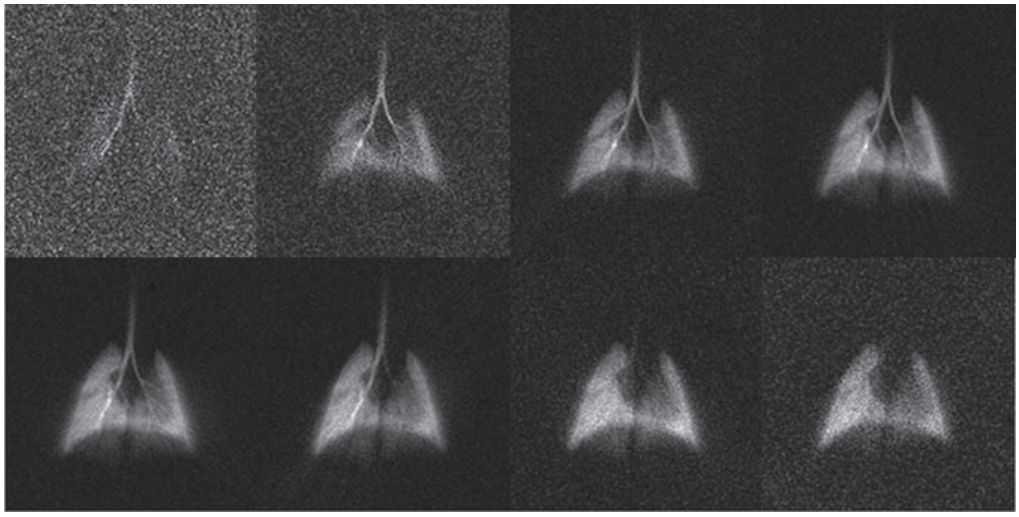

Fig. 2. Examples of lung ventilation images obtained under free-breathing conditions. The images represent the intrapulmonary distribution of polarized ^{3}He for different time windows of the breathing cycle of the animal. In this example, images correspond to consecutive 100-ms time windows. Images are reconstructed using a retrospective Cine algorithm. The total acquisition time is 20 s.

3.1.5. Expected Results

The expected results for ventilation imaging under spontaneous breathing conditions are the visualization of ventilated airspaces at tidal volumes. The Cine reconstruction algorithm generates images of ventilation at different phases of the breathing cycle (**Fig. 2**). Images of ventilation and gas arrival maps can be monitored during slow intravenous injection of methacholine. With increasing injected dose of methacholine, ventilation defects and delayed gas arrival time in the airspaces can be observed (**Fig. 3**).

3.2. Lung Proton MR Imaging in LPS Model of Lung Inflammation

3.2.1. Administration of LPS

1. Dissolve 1 mg/kg of LPS in 0.2 mL of saline.
2. Anesthetize the rat (injection of ketamine/xylazine) (*see* **Note 2**).
3. Wait until the animal loses its toe pinch reflex and position it supine on the board with the head tilted up (*see* **Note 4**).
4. Intubate the animal with a 26-gauge flexible polyethylene catheter attached to the 1-mL syringe (*see* **Note 5**) into a trachea (it is recommended to verify the length of the catheter first) and instill 0.2 mL of the solution (**Fig. 4**).
5. In order to have a homogeneous distribution of the suspension in the lungs, provoke hyperventilation by using a ventilator (*see* **Note 6**).
6. Allow the animal to recover maintaining its temperature on a heating pad.

3.2.2. Imaging Parameters

Two different approaches can be used: the first one uses a gradient echo imaging sequence which permits to obtain a high

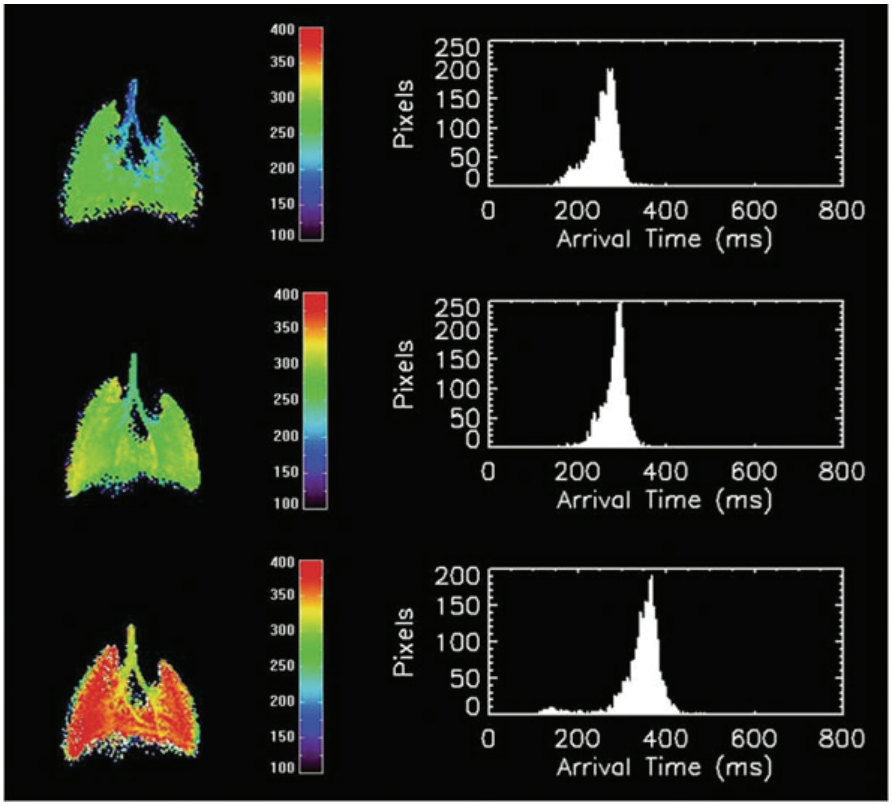

Fig. 3. Examples of parametric ventilation maps obtained in a rat using the ^{3}He free-breathing protocol. Parametric maps represent the local arrival time values in milliseconds. The arrival time is defined as the time delay between the arrival of gas into the trachea and the arrival of gas in a given pixel. The corresponding histogram for arrival time value is shown on the *right*. From *top* to *bottom*, the images correspond to the data acquisition before intravenous injection of methacholine, 11 and 21 min after the start of the injection of methacholine (10 μg/mL, 6 mL/h injection rate), respectively.

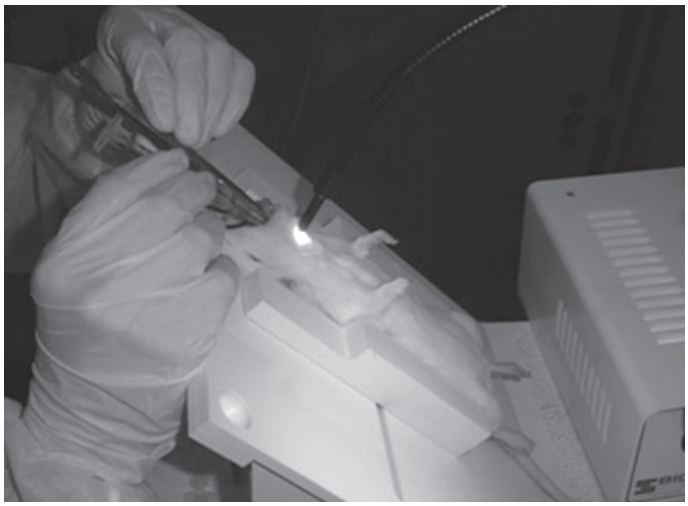

Fig. 4. Example of instillation setup. For instillation of agents, position a rat supine with the head tilted up. Intubate rats perorally with a 26-gauge flexible polyethylene catheter into the trachea. Inject 0.2 mL of solution.

contrast between dark-appearing lung parenchyma and the expected inflammation hallmark; the second, based on a radial ultra-short echo time sequence, is less sensitive to motion and blurring artifacts occurring in the thoracic cavity during respiration, and thus can provide more accurate assessment of image borders. The optimal sequence parameters at 4.7 T are as follows:

- Gradient echo imaging: TR = 5.6 ms, TE = 2.7 ms; bandwidth = 100 kHz, flip angle = 15°, FOV = 6 × 6 cm^2, matrix size = 256 × 128, and slice thickness = 1.5 mm. A single slice with 60 averages is acquired, resulting in an acquisition time of 75 s (55). To cover the entire lung volume, use 12–28 consecutive axial slices.
- Radial ultra-short echo time imaging: TR = 80 ms, TE = 450 μs; bandwidth = 64 kHz, flip angle = 20°, FOV 6 × 6 cm^2, 400 radials/image, 128 samples/view, slice thickness = 1.5 mm. A multi-slice acquisition with four averages is applied. Neither cardiac nor respiratory gating is used. The total acquisition time is equal to 4 min with an acquisition covering 12 contiguous axial slices.

3.2.3. Optimal Imaging Times

To observe an inflammation hallmark, the optimal imaging time is 48 h after LPS exposure (34, 49). However, the inflammation can be detected at its earlier stage (6 h after the challenge) as well as at later time points (up to 72–144 h after the challenge), reflecting pleura and mucus hypersecretion, respectively (34, 59). The protocol scheme is presented in **Fig. 5**.

3.2.4. Expected Results

The expected result is a hyperintense signal visualized on the T_1-weighted images. The observed signal is usually characterized by two components: one, of higher intensity, is attributed to the

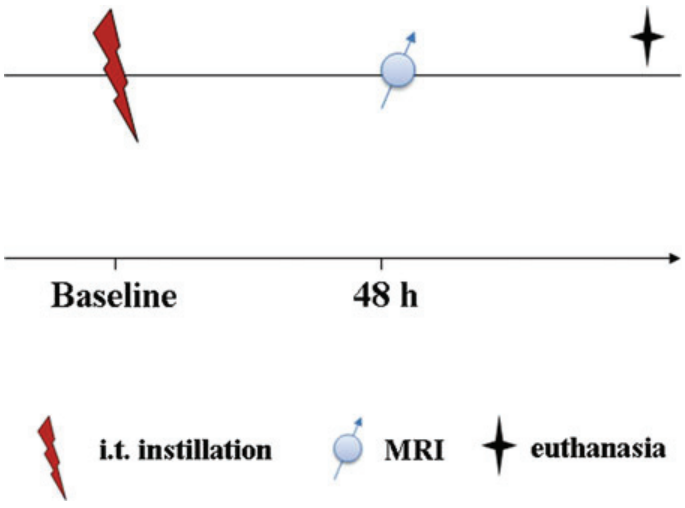

Fig. 5. Scheme of the experimental protocol.

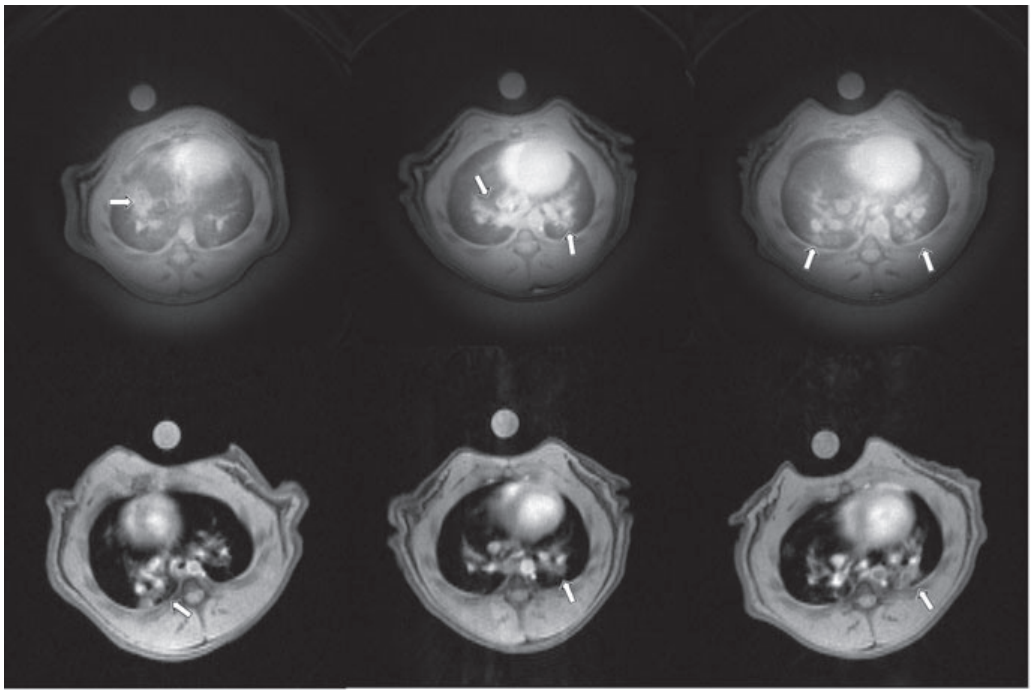

Fig. 6. Exemplary images of thorax in the axial plane 48 h after LPS instillation acquired using the radial UTE (*top*) and the gradient echo imaging sequence (*bottom*). The *arrows* indicate signal from inflammation.

edema; the second patchy-like appearance, with a less intense signal, represents an evidence of mucus secretion (**Fig. 6**).

3.2.5. Application in Pharmacology

The exposure to the endotoxin LPS is a well-established model of acute inflammation in rodents and similar to that observed in human COPD. The proposed protocols have the potential to provide easy implementation and accurate and non-invasive means of monitoring the effect of anti-inflammatory drugs in the experimental research of lung inflammation (31).

4. Notes

1. The homemade mask was realized as follows. The barrel of a standard plastic syringe was cut to the appropriate length to cover the head of the animal. The tip of the syringe barrel was sectioned to fit the nose of the animal. A hole was drilled in the screw cap of a plastic vial. This screw cap was then glued to the tip of the barrel of the syringe. This mask was positioned on the head of the animal. The body of the plastic vial was sectioned. The balloon (later on filled with polarized helium) was tied on the body of the plastic vial. Before launching the ^{3}He MR acquisition, the plastic vial attached to the helium-filled balloon is screwed on the animal mask.

2. Ketamine–xylazine cocktail is a preferred anesthesia over pentobarbital in ventilation studies because it induces less cardio-respiratory depression. Standard dose for intraperitoneal injection in rat and mouse is 3–9 mL/kg body weight of a mixture of 1 mL ketamine (100 mg/mL), 1 mL xylazine (20 mg/mL), and 5 mL saline.

   Alternatively, isoflurane inhalation can be used to anesthetize animals during MR acquisitions (proton studies).
3. Reconstruction of MR images acquired with radial *k*-space sampling requires dedicated reconstruction algorithms (regridding, i.e., interpolation of radially sampled data onto a Cartesian grid or filtered back-projection). MR manufacturers might provide such software in their reconstruction package. However, it is likely that off-line dedicated reconstruction software will be needed. In our studies, we use a set of homemade programs developed under IDL software (Research Systems Inc., Boulder, CO).
4. Hold the rat's head tight on to the board by a loop string or rubber which passes under the upper incisors.
5. or intubation, put out the rat's tongue and open the rat's mouth 2 cm wide using smooth blunt forceps. While inserting the catheter, lighten the larynx from the exterior using a light source.
6. Ventilate the rat at a frequency of 60 breaths per minute for approximately 1 min.

Acknowledgments

Magdalena Zurek acknowledges a fellowship from the European Network PHELINET (MRTN-CT-2006-36002).

References

1. Albert, M. S., Cates, G. D., Driehuys, B., Happer, W., Saam, B., Springer, C. S. Jr., and Wishnia, A. (1994) Biological magnetic resonance imaging using laser-polarized ^{129}Xe. *Nature* **370**, 199–201.
2. Middleton, H., Black, R. D., Saam, B., Cates, G. D., Cofer, G. P., Guenther, R., Happer, W., Hedlund, L. W., Johnson, G. A., and Juvan, K. (1995) MR imaging with hyperpolarized ^{3}He gas. *Magn. Reson. Med.* **33**, 271–275.
3. Ebert, M., Grossmann, T., Heil, W., Otten, W. E., Surkau, R., Leduc, M., Bachert, P., Knopp, M. V., Schad, L. R., and Thelen, M. (1996) Nuclear magnetic resonance in humans using hyperpolarized helium-3. *Lancet* **347**, 1297–1299.
4. MacFall, J. R., Charles, H. C., Black, R. D., Middleton, H., Swartz, J. C., Saam, B., Driehuys, B., Erickson, C., Happer, W., Cates, G. D., Johnson, G. A., and Ravin, C. E. (1996) Human lung air spaces: potential

for MR imaging with hyperpolarized He-3. *Radiology* **200**, 553–558.
5. Viallon, M., Cofer, G. P., Suddarth, S. A., Möller, H. E., Chen, X. J., Chawla, M. S., Hedlund, L. W., Crémillieux, Y., and Johnson, G. A. (1999) Functional MR microscopy of the lung with hyperpolarized ^{3}He. *Magn. Reson. Med.* **41**, 787–792.
6. Chen, B. T., Yordanov, A. T., and Johnson, G. A. (2005) Ventilation-synchronous magnetic resonance microscopy of pulmonary structure and ventilation in mice. *Magn. Reson. Med.* **53**, 69–75.
7. Saam, B. T., Yablonskiy, D. A., Kodibagkar, V. D., Leawoods, J. C., Gierada, D. S., Cooper, J. D., Lefrak, S. S., and Conradi, M. S. (2000) MR imaging of diffusion of (3)He gas in healthy and diseased lungs. *Magn. Reson. Med.* **44**, 174–179.
8. Chen, X. J., Hedlund, L. W., Möller, H. E., Chawla, M. S., Maronpot, R. R., and Johnson, G.A. (2000) Detection of emphysema in rat lungs by using magnetic resonance measurements of ^{3}He diffusion. *Proc. Natl. Acad. Sci. U.S.A.* **10**, 11478–11481.
9. Yablonskiy, D. A., Sukstanskii, A. L., Leawoods, J. C., Gierada, D. S., Bretthorst, G. L., Lefrak, S. S., Cooper, J. D., and Conradi, M. S. (2002) Quantitative in vivo assessment of lung microstructure at the alveolar level with hyperpolarized ^{3}He diffusion MRI. *Proc. Natl. Acad. Sci. U.S.A.* **99**, 3111–3116.
10. Peces-Barba, G., Ruiz-Cabello, J., Crémillieux, Y., Rodríguez, I., Dupuich, D., Callot, V., Ortega, M., Rubio Arbo, M. L., Cortijo, M., and Gonzalez-Mangado, N. (2003) Helium-3 MRI diffusion coefficient: correlation to morphometry in a model of mild emphysema. *Eur. Respir. J.* **22**, 14–19.
11. Dugas, J. P., Garbow, J. R., Kobayashi, D. K., and Conradi, M. S. (2004) Hyperpolarized (3)He MRI of mouse lung. *Magn. Reson. Med.* **52**, 1310–1317.
12. Mata, J. F., Altes, T. A., Cai, J., Ruppert, K., Mitzner, W., Hagspiel, K. D., Patel, B., Salerno, M., Brookeman, J. R., de Lange, E. E., Tobias, W. A., Wang, H. T., Cates, G. D., and Mugler, J. P. 3rd. (2006) Evaluation of emphysema severity and progression in a rabbit model: a comparison of hyperpolarized He-3 and ^{129}Xe diffusion MRI with lung morphometry. *J. Appl. Physio.* **102**, 1273–1280.
13. Saam, B., Happer, W., and Middleton, H. (1995) Nuclear relaxation of ^{3}He in the presence of O_2. *Phys. Rev. A* **52**, 862–865.
14. Eberle, B., Weiler, N., Markstaller, K., Kauczor, H., Deninger, A., Ebert, M., Grossmann, T., Heil, W., Lauer, L. O., Roberts, T. P., Schreiber, W. G., Surkau, R., Dick, W. F., Otten, E. W., and Thelen, M. (1999) Analysis of intrapulmonary O(2) concentration by MR imaging of inhaled hyperpolarized helium-3. *J. Appl. Physiol.* **87**, 2043–2052.
15. Deninger, A. J., Eberle, B., Ebert, M., Grossmann, T., Heil, W., Kauczor, H., Lauer, L., Markstaller, K., Otten, E., Schmiedeskamp, J., Schreiber, W., Surkau, R., Thelen, M., and Weiler, N. (1999) Quantification of regional intrapulmonary oxygen partial pressure evolution during apnea by ^{3}He MRI. *J Mag. Reson.* **141**, 207–216.
16. Deninger, A. J., Eberle, B., Ebert, M., Grossmann, T., Hanisch, G., Heil, W., Kauczor, H.U., Markstaller, K., Otten, E., Schreiber, W., Surkau, R., and Weiler, N. (2000) ^{3}He-MRI-based measurements of intrapulmonary pO2 and its time course during apnea in healthy volunteers: first results, reproducibility, and technical limitations. *NMR Biomed.* **13**, 194–201.
17. Deninger, A. J., Eberle, B., Bermuth, J., Escat, B., Markstaller, K., Schmiedeskamp, J., Schreiber, W. G., Surkau, R., Otten, E., and Kauczor, H-U. (2002) Assessment of a single-acquisition imaging sequence for oxygen-sensitive ^{3}He. *Magn. Reson. Med.* **47**, 105–114.
18. Wild, J. M., Fichele, S., Woodhouse, N., Paley, M. N., Kasuboski, L., and van Beek, E. J. (2005) 3D volume-localized pO2 measurement in the human lung with ^{3}He. MRI *Magn. Reson. Med.* **53**, 1055–1064.
19. Jalali, A., Ishii, M., Edvinsson, J. M., Guan, L., Itkin, M., Lipson, D. A., Baumgardner, J. E., and Rizi, R. R. (2004) Detection of simulated pulmonary embolism in a porcine model using hyperpolarized ^{3}He MRI. *Magn. Reson. Med.* **51**, 291–298.
20. Cieślar, K., Stupar, V., Canet-Soulas, E., Gaillard, S., and Crémillieux, Y. (2007) Alveolar oxygen partial pressure and oxygen depletion rate mapping in rats using (3)He ventilation imaging. *Magn. Reson. Med.* **57**, 423–430.
21. Cieślar, K., Alsaid, H., Stupar, V., Gaillard, S., Canet-Soulas, E., Fissoune, R., and Crémillieux, Y. (2007) Measurement of nonlinear pO2 decay in mice lungs using 3He-MRI. *NMR Biomed.* **20**, 383–391.
22. Ruppert, K., Brookeman, J. R., Hagspiel, K. D., and Mugler, J. P. 3rd. (2000) Probing lung physiology with xenon polarization transfer contrast (XTC). *Magn. Reson. Med.* **44**, 349–357.
23. Chen, B. T. and Johnson, G. A. (2004) Dynamic lung morphology of

methacholine-induced heterogeneous bronchoconstriction. *Magn. Reson. Med.* **52**, 1080–1086.
24. Mosbah, K., Crémillieux, Y., Adeleine, P., Dupuich, D., Stupar, V., Nemoz, C., Canet, E., and Berthezène, Y. (2006) Quantitative measurements of regional lung ventilation using helium-3 MRI in a methacholine-induced bronchoconstriction model. *J. Magn. Reson. Imaging* **24**, 611–616.
25. Hedlund, L. W., Moller, H. E, Chen, X. J., Chawla, M. S., Cofer, G. P., and Johnson, G. A. (2000) Mixing oxygen with hyperpolarized (3)He for small-animal lung studies. *NMR Biomed.* **13**, 202–206.
26. Ramirez, M. P., Sigaloff, K. C., Kubatina, L. V., Donahue, M. A., Venkatesh, A. K., and Albert, M. S. (2000) Physiological response of rats to delivery of helium and xenon: implications for hyperpolarized noble gas imaging. *NMR Biomed.* **13**, 253–264.
27. Chen, B. T., Yordanov, A. T., and Johnson, G. A. (2005) Ventilation-synchronous magnetic resonance microscopy of pulmonary structure and ventilation in mice. *Magn. Reson. Med.* **53**, 69–75.
28. Imai, H., Narazaki, M., Inoshita, H., Kimura, A., and Fujiwara, H. (2006) MR imaging of mouse lung using hyperpolarized ^{3}He: image acquisition and T_1 estimation under spontaneous respiration. *Magn. Reson. Med. Sci.* **5**, 57–64.
29. Stupar, V., Canet-Soulas, E., Gaillard, S., Alsaid, H., Beckmann, N., and Crémillieux, Y. (2007) Retrospective Cine (3)He ventilation imaging under spontaneous breathing conditions: a non-invasive protocol for small-animal lung function imaging. *NMR Biomed.* **20**, 104–112.
30. Beckmann, N., Cannet, C., Karmouty-Quintana, H., Tigani, B., Zurbruegg, S., Blé, F. X., Crémillieux, Y., and Trifilieff, A. (2007) Lung MRI for experimental drug research. *Eur. J. Radiol.* **64,** 381–396.
31. Beckmann, N., Crémillieux, Y., Tigani, B., Karmouty Quintana, H., Blé, F. X., and Fozard, J. R. (2006) Lung MRI in small rodents as a tool for the evaluation of drugs in models of airways diseases. In: Beckmann, N. (ed.), *In Vivo MR Techniques in Drug Discovery and Development.* Taylor & Francis Group, New York, pp. 351–372.
32. Nieman, B. J., Bishop, J., Dazai, J., Bock, N. A., Lerch, J. P., Feintuch, A., Chen, X. J., Sled, J. G., and Henkelman, R. M. (2007) MR technology for biological studies in mice. *NMR Biomed.* **20**, 291–303.
33. Beckmann, N., Tigani, B., Ekatodramis, D., Borer, R., Mazzoni, L., and Fozard, J. R. (2001) Pulmonary edema induced by allergen challenge in the rat: non-invasive assessment by magnetic resonance imaging. *Magn. Reson. Med.* **45**, 88–95.
34. Beckmann, N., Tigani, B., Sugar, R., Jackson, A. D., Jones, G., Mazzoni, L., and Fozard, J. R. (2002) Noninvasive detection of endotoxin-induced mucus hypersecretion in rat lung by MRI. *Am. J. Physiol. Lung Cell Mol. Physiol.* **283**, 22–30.
35. Karmouty-Quintana, H., Cannet, C., Zurbruegg, S., Blé, F. X., Fozard, J. R., Page, C. P., and Beckmann, N. (2006) Proton MRI as a noninvasive tool to assess elastase-induced lung damage in spontaneously breathing rats. *Magn. Reson. Med.* **56**, 1242–1250.
36. Karmouty-Quintana, H., Cannet, C., Zurbruegg, S., Blé, F. X., Fozard, J. R., Page, C. P., and Beckmann, N. (2007) Bleomycin-induced lung injury assessed noninvasively and in spontaneously breathing rats by proton MRI. *J. Magn. Reson. Imaging* **26**, 941–949.
37. Bergin, C. J., Pauly, J. M., and Macovski, A. (1991) Lung parenchyma: projection, reconstruction MR imaging. *Radiology* **179**, 777–781.
38. Gewalt, S. L., Glover, G. H., Hedlund, L. W., Cofer, G. P., MacFall, J. R., and Johnson, G. A. (1993) MR microscopy of the rat lung using projection reconstruction. *Magn. Reson. Med.* **29**, 99–106.
39. Zurek, M., Bessaad, A., Cieslar, K., and Crémillieux, Y. (2010) Validation of simple and robust protocols for high resolution lung proton MR imaging in mice. *Magn. Reson. Med.* **64**, 401–407.
40. Olsson, L. E., Lindahl, M., Onnervik, P. O., Johansson, L. B., Palmér, M., Reimer, M. K., Hultin, L., and Hockings, P. D. (2007) Measurement of MR signal and T2* in lung to characterize a tight skin mouse model of emphysema using single-point imaging. *J. Magn. Reson. Imaging* **25**, 488–494.
41. Takahashi, M., Togao, O., Obara, M., Cauteren, M., Ohno, Y., Malloy, C., and Dimitrov, I. (2009) Ultra-short echo time (UTE) MR imaging of the lung: comparison between normal and emphysematous mice. *Proceedings of the 17th Annual Meeting of ISMRM*, Honolulu, Hawaii, USA, p. 11.
42. Suga, K., Yuan, Y., Ogasawara, N., Tsukuda, T., and Matsunaga, N. (2003) Altered clearance of gadolinium diethylenetriaminepentaacetic acid aerosol from bleomycin-injured dog lungs: initial observations. *Am. J. Respir. Crit. Care Med.* **167**, 1704–1710.